Evolution of Entanglement Structure in Open Quantum Systems

James Gordon Morley–Wilkinson

A THESIS SUBMITTED FOR THE DEGREE OF

Doctor of Philosophy

UCL

September 2019

Acknowledgements

This thesis wouldn't have been possible without the generous support of colleagues, friends, and family. I would like to thank my supervisor Andrew Green for his guidance and advice. Thanks also to Viv Kendon for her encouragement and support throughout my research career. For their unwavering comradeship during my time at UCL I would like to thank my peers in cohort 2 of the Quantum Technologies CDT: Paul, Nathanaël, Padraic, Danial, Gavin, Alex, Sofia, Simon, Mike, and David.

Special thanks to Heather, Thomas, Helen, and Jack for their quiet support and for reminding me of life outside the PhD bubble.

Finally, I would like to thank my fantastic wife Lorna, to whom this thesis is dedicated.

I, James Morley-Wilkinson confirm that the work presented in this thesis is my own. Where information has been derived from other sources, I confirm that this has been indicated in the thesis.

Parts of this thesis have been published, as follows:

Chapter 3	A. Hallam, *J. G. Morley*, and A. G. Green. The Lyapunov spectra of quantum thermalization. Nature Communications, 10(2708), 2019.
Chapter 6	*J. G. Morley*, N. Chancellor, S. Bose, and V. Kendon. Quantum search with hybrid adiabatic quantum-walk algorithms and realistic noise. Physical Review A, 99(022339), 2019.

Abstract

The thesis presents research related to the dynamics of quantum systems, both isolated and in the presence of interactions with their environment. Generally, I employ matrix product state (MPS) techniques to explore quantum dynamics in open and closed systems.

In the first part I present a study of quantum chaos and how mapping to a MPS variational manifold allow the use of techniques developed in the study of classical many-body systems. Using code developed for this project the Lyapunov spectrum is extracted to give an alternative perspective on eigenstate thermalization, pre-thermalization and integrability.

In the second part, I present a novel combination of MPS methods with a Langevin description of the open system. I use this to show how coupling to the environment restricts the growth of entanglement. The consequences of this are relevant for simulations of open quantum systems and their use in in quantum technologies.

Finally I discuss applications of these ideas to quantum search. I consider adiabatic and quantum walk algorithms for optimal scaling quantum search algorithms, and hybridisations between the two. The robustness of the different underlying physical mechanisms is investigated in a simple infinite-temperature model, and in a low-temperature limit using the MPS Langevin equation.

Impact statement

The dynamics of strongly coupled many-body quantum systems is both a frontier of physics research and a burgeoning area of technological development. Quantum computers, capable of performing calculations impossible on classical hardware, can be built from such systems.

The research presented in this thesis makes three key innovations in this area:

(1) The study of thermalization in many-body quantum systems is furthered *via* a new method of projecting the dynamics onto a manifold of matrix product states. The resulting trajectories are chaotic, proving a link to techniques based on dynamical chaos in classical systems to describe the quantum problem.

(2) A Langevin open systems model is developed for efficient matrix product parameterizations of many body quantum systems. This models a thermal coupling to the system environment *via* noise and dissipation, combining this with the ability of matrix product states to describe large systems with local entanglement.

(3) An in-depth study of a simple continuous-time quantum computing protocol is given. Two quantum protocols for quantum searching *via* different physical processes are compared, and a family of algorithms that hybridize the effects are derived. It is shown that the whole family of algorithms produce the optimal quantum speedup. The relative merits of different degrees of hybridization are investigated in-depth, including a study of open systems effects with the matrix product state Langevin equation.

Works relating to (1) and (3) are published in peer-reviewed journals. The scratch-built code library developed for (2) is publicly available, and the research is in preparation for publication.

Contents

1 Introduction 15

2 Technical Introduction 29

1 Introduction 30

1.1 Entanglement in many-body quantum systems 30

1.1.1 Quantum entanglement 30

1.1.2 Defining entanglement 32

1.1.3 Entanglement in many-body quantum systems 33

1.2 Origins of entanglement-based parameterizations 34

1.3 Chapter summary 35

2 Matrix product states 36

2.1 Definitions and notation 36

2.1.1 Defining the matrix product state parameterization . 37

2.1.2 Calculating expectation values 38

2.1.3 Open, periodic, and infinite matrix product states . . 40

2.2 Gauge choices 41

2.2.1 Gauge freedoms in matrix product states 41

2.2.2 Canonical gauge choices 41

2.3 Properties of matrix product states 44

3 Time-dependent variational principle 45

3.1 The time-dependent variational principle (TDVP) 45

3.2 Applying TDVP to matrix product states 46

3.2.1 Parameterizing the tangent space 46

3.2.2 Infinite matrix product states 47

3.2.3 Finite matrix product states 47

3.3 Code validation 49

3 Quantum chaos - tracking Lyapunov coefficients 53

1 Thermalization 54

1.1 Dynamical chaos in many-body classical systems 54

1.2 Eigenstate thermalization in many-body quantum systems . . . 55

2 Tracking chaos with TDVP 57

2.1 Projecting quantum dynamics 57

2.2 Extracting the Lyapunov spectrum 57

2.3 Accurate numerical integration 60

2.4 The thermofield double 63

3 Results 66

3.1 Wavefunction matrix product state 66

3.2 Thermofield matrix product state 71

4 Discussion 73

4 A Langevin equation for matrix product states 75

1 Langevin methods for open quantum systems 76

1.1 Classical Langevin equations 76

1.2 The open quantum systems toolkit 78

1.2.1 General survey 79

1.2.2 Caldeira-Leggett model 81

1.3 Trajectories for open many-body quantum systems 81

2 A quantum Langevin equation for MPS 83

2.1 Heuristic derivation 83

2.2 Derivation from Keldysh field theory 86

2.2.1 Forming a Keldysh path integral from the propagator 86

2.2.2 Derivation 87

3 Numerical Implementation 92

3.1 Noise term 92

3.1.1 Numerical methods for stochastic differential eqns . . 92

3.1.2 Ito and Stratonovich differentials 93

3.1.3 Strong convergence in the MPS Langevin equation . . 94

3.2 Friction term 94

3.2.1 Explicit expression for friction 96

3.2.2 Algorithm for finding friction update to MPS 98

3.2.3 Imposing locality 100

4 Discussion 102

5 Applications of Langevin equation for MPS 103

1 Real-time frictional cooling to the ground state 104

1.1 Ground state finding for quantum spin chains 104

1.2 Langevin cooling to ground state with MPS 105
1.2.1 Imposing locality 107
2 Sampling of the thermal distribution 108
2.1 Techniques for sampling thermal distributions 108
2.2 Results 108
3 Restriction of entanglement by noise 111
3.1 Environmental degradation of entanglement generation 111
3.1.1 Choosing a Hamiltonian 111
3.1.2 Approach 112
3.2 Results 112
3.2.1 Closed system dynamics 112
3.2.2 Open system dynamics 113
4 Discussion 117

6 Hybrid approaches to quantum searching 119

1 Quantum speedup in unstructured searching 120
1.1 Encoding search into quantum states 120
1.2 Quantum searching by quantum walk 121
1.3 Quantum searching by adiabatic dynamics 123
1.4 Optimizing adiabatic search schedules 125
2 Hybrid adiabatic and quantum walk searching 130
2.1 Hybrid searching 130
2.2 Demonstrating quadratic speedup with single runs 133
2.2.1 Reduction to single avoided crossing model 133
2.2.2 Analyzing the single avoided crossing model 135
2.3 Performance in multiple search protocols 136
3 Noisy searching 138
3.1 Infinite temperature bath 138
3.1.1 Model 138
3.1.2 Single search 139
3.1.3 Multiple searches 141
3.2 Finite temperature bath 143
3.2.1 Model and approach 143
3.2.2 Frictional searching 143
4 Discussion 146

7 Discussion 149

8 Bibliography **153**

Appendices **169**

A Extracting the classical Lyapunov spectrum **171**

B Testing frictional matrix product state update **173**

C Calculation of optimal schedule for hypercube search **179**

1 Analytical derivation of hypercube schedule 179

2 Numerical derivation of hypercube schedule 183

D Numerical methods for Chapter 6 **187**

E Single avoided crossing model for quantum search **189**

Chapter 1

Introduction

This chapter aims to connect the rest of the thesis with ideas of broader interest. The key themes of the research – quantum entanglement, and its importance for quantum technologies – are introduced at a general level. Several of the foundational ideas are described and illustrated.

The last few years have seen a significant increase in funding for the development of quantum technologies. In June 2019 the UK's National Quantum Technology Program announced funding set to push the total investment in the programme in excess £1 billion [1], and the EU have committed more than €1 billion for the initial phase of the Quantum Technologies Flagship [2]. This is replicated worldwide, with the US and China also investing heavily. A 2015 estimate of quantum technologies funding put the figure at around $1.5 billion per year [3].

The goal in quantum technologies is to use the phenomenology of quantum mechanics to gain a fundamental edge over their non-quantum, 'classical', counterparts. Possibilities for this include ultra high precision sensors [4], improved standards in secure communications [5], and quantum computers capable of exponential speedup [6], with applications in industries ranging from aerospace [7] to finance [8] to mathematics [9, 10] to scientific research [11].

There are a small number of quantum technologies that are already well-established. Atomic clocks that use the natural quantum energy levels of atoms have provided best in class precision since the 1950s, with errors of less than 1 part per billion [12]. Semiconductor transistors, built on an understanding of the quantum mechanics of electrons in metals, allowed miniaturization of computer circuits onto integrated chips that underpin most modern electronics. New quantum technologies aim to use more exotic quantum effects, that are correspondingly harder to realize experimentally.

Perhaps unsurprisingly, those familiar with quantum mechanics have suggested technological applications long before those ideas were experimentally viable. The idea of using quantum mechanics for computational purposes can be traced as far back as 1959 [13], and was considerably fleshed out in the late '80s, '90s and '00s [14, 15, 16, 17]. However, the ability to implement these schemes 'coherently' - that is, without errors disrupting the important quantum effects - is only recently emerging. An example is given by gate-based quantum computers, where operations ('gates') are applied to a quantum system to process information. Real quantum computers of this type are now able to apply gates with errors occurring less than 1% of the time [18, 19, 20]. Combined with developments in error-correcting schemes, this approach is now considered a plausible path to quantum computers that outperform what is possible classically. There have been similar developments in other techniques for controlling quantum effects: the 2012 Nobel prize in physics recognized developments in manipulating single atoms in laser cavities, citing "groundbreaking experimental methods that enable measuring and manipulation of individual quantum systems". Experimental breakthroughs mean that more quantum effects than ever are accessible for study, and for technological development.

A key difficulty in manipulating quantum systems is their sensitivity to any disturbances. Simply measuring a quantum system can induce a catastrophic ‘collapse’ of the system state: a one-way process that radically alters the state of the system and results in a loss of information. While this may be a worst-case scenario, a quantum system is always in contact with its surroundings in one way or another. Interactions with a system’s environment can look like a type of measurement, and usually lead to an unwanted loss of coherence in the system. Understanding and guarding against decoherence effects is a key experimental challenge.

There are also significant theoretical obstacles to studying collections of quantum systems. The amount of information required to describe them can increase exponentially with the number of systems. This scaling is severe - in practice it is impossible to simulate a quantum computer of more than around 50 quantum digits [21]. Coping with this is a significant challenge, which can be addressed by finding mathematical shortcuts and approximations.

There are many physical questions about the behaviour of collections of quantum systems that remain unanswered. Quantum mechanics was developed to explain phenomena on a very small scale, and generally applies only on that scale. A single atom needs to be described quantum mechanically, however a tennis ball of atoms is accounted for by the quite different rulebook of classical mechanics. Yet the tennis ball is made up of quantum mechanical atoms. Understanding how the quantum and classical rulebooks morph into one another is a fascinating question.

The goal of the remainder of this introduction is to develop these ideas further and explain how the research presented in this thesis fits in. First I will discuss what quantum mechanics is, where it came from, and some of the distinct properties of quantum dynamics. Then I will explain in more depth how quantum effects may be repurposed for technological gain, using the semiconductor transistor as a case study, and considering which quantum phenomena are promising candidates for new technologies. Following this I introduce quantum entanglement, discussing how entangled states can be used for quantum computing and the challenges of using entangled states. I then discuss the difficulties of describing collections of quantum systems, and how the exponential space requirement may be beaten. Next I explain how interactions with the environment are important, and how they may be accounted for. Finally I summarize the goals and strategy of the thesis, and outline its remaining contents.

Quantum mechanics

Our everyday experiences are largely described by classical mechanics: it is consistent with our intuition for how objects behave when we interact with them. If we kick a ball we have a clear idea of where that ball will go, and classical mechanics will predict that trajectory with supreme accuracy. The planets follow classical trajectories around the sun, and aircraft will fly if classical mechanics says they will. Classical mechanics was first codified by Newton in the 17th century, and has been enourmosly successful. Newton's laws underpin much of the science and technology of the modern world, from feats of civil engineering to the internal combustion engine.

However, there are phenomena that can't be explained by classical mechanics. One such case is the spectrum of light emitted by the sun. Fig 1.1 shows such a spectrum: the result of splitting sunlight into its different colours, or wavelength components. This demonstrates that white light is in fact made from a combination of different colours. It also reveals that there are particular wavelengths that are missing, leaving dark lines on the spectrum. While it would come to be understood that the dark lines corresponded to absorption of light by electrons, classical mechanics was unable to account for the discrete, 'quantized', nature of the dark lines.

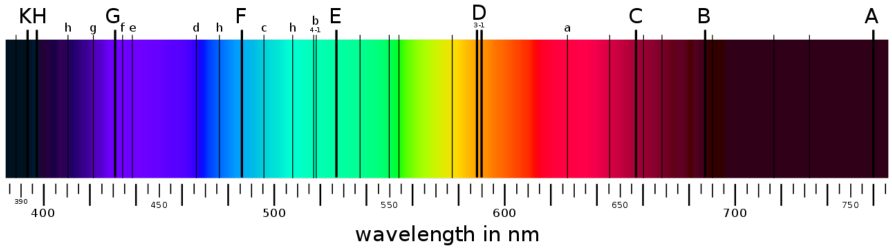

Figure 1.1: *Dark lines in the spectrum of solar light.* When studying the different wavelength components of light from the sun a continuum of colours is seen, except that specific wavelengths are missing – these show up as dark lines. It would take a quantum theory of matter and light to understand this. These features are named after Joseph von Fraunhofer, and the conventional labelling of the Fraunhofer lines is indicated. Image retrieved from `https://commons.wikimedia.org/wiki/File:Fraunhofer_lines.svg`

An intense period of research in the early 20th century resulted in a theory that could account for the dark lines with incredible accuracy. In this new 'quantum' mechanics, electrons in the atom can only exist at specific energy levels, and therefore can only absorb light of exactly the right wavelength to move between these levels. The dark lines seen in sunlight tell us about which wavelengths are absorbed in the sun, and allow us to work out what the sun is made from.

While quantum mechanics works well as an explanatory tool, it initially seemed like a very problematic as a picture of how the world really works. For example, quantum mechanics is fundamentally non-deterministic: it will never be possible to say exactly what will happen, only to give the likelihood of each possible outcome. This was a difficult concession to make philosophically, with Einstein famously writing 'God does not play dice' [22]. Quantum mechanics, while useful for predicting spectral data, was surely just an approximation to a more fundamental, deterministic, theory. Attempts to demonstrate this came to a head with Bell's theorem [23], which shows that unless more problematic concessions are made, no theory that has access to extra information can reproduce the predictions of quantum mechanics entirely[1]. Quantum mechanics, with all its idiosyncrasies, was here to stay.

Perhaps most fundamental to understanding quantum mechanics is to realize that it comes with some amount of irreducible uncertainty. In classical mechanics a probability distribution arises when we have imperfect knowledge - if we flip a fair classical coin and don't look, we can say the outcome will be heads with probability 0.5, or tails with probability 0.5. However this is only because we have missing information: if we look at the flipped coin we will know with certainty what the result is. In quantum mechanics there are probability distributions even if you have the most complete information possible.

The mathematics of quantum mechanics tells us how these probability distributions change over time. Remarkably, they evolve in the same way that waves do: they have peaks and troughs, amplitudes and phases, and so can reinforce or cancel out. The size of the probability wave at any point corresponds to the probability of that outcome. In this way small particles such as electrons can be shown, experimentally as well as theoretically, to behave as particles in some scenarios and as waves in others.

Another important aspect of quantum mechanics is the effect of measurements, as implied by the example of the classical coin toss. If the classical probabilities are banished by simply looking at the coin, what's to stop us looking at the quantum-mechanical coin? The answer is that in quantum mechanics, the act of measuring something can be destructive. Classical mechanics takes for granted the ability to measure anything we please, to accuracies only limited by our experimental ability, while leaving the system unchanged. Quantum systems are typically extremely small however, and will notice if they are being measured. In the coin example, the process of looking at the coin requires light to bounce off the face of the coin and to enter our eyes. Light bouncing off a quantum coin will alter its state, so that by the time the light leaves the coin the information it conveys is already out of date. In general, measurement of a quantum system will 'collapse' its probability distribution, so that even the most delicate measurement can radically alter the system's state, with the

---

[1] The list of more problematic concessions include: information travelling faster than the universal speed limit $c \simeq 3 \times 10^8 m/s = 671$ million mph; or a 'superdeterministic' universe – one without free will and where everything was determined before the universe began.

quantum wave-like behaviour collapsing entirely.

These are just some of the consequences of quantum mechanics. Clearly quantum systems exhibit a phenomonology very different to the world of classical mechanics. If these quantum effects can be reliably harnessed, how can they be used for quantum technologies?

Quantum technologies

What is required to develop a new technology? Just as a machine can be thought of as a device for converting input forces into more useful output forces, a technology repurposes some phenomena to a more useful end. Therefore having access to new phenomena means that it may be possible to use it to develop new technology. Experiments revealing the quantum nature of systems have revealed a host of such phenomena, raising the possibility of quantum technologies that take advantage of them.

Arguably the most successful quantum technology to date is semiconductor electronics based on miniaturized transistors. The properties of semiconductor metals are explained by quantum mechanics, and this understanding underpins the manufacture of anything with a computer chip. Perhaps surprisingly then the market is huge, with global semiconductor sales in excess of $400bn annually [24]. A crucial component in modern electronics is the transistor, which acts as a switch or amplifier for electrical signals. Early computers used switches built inside vacuum tubes made with glass, which were large, unreliable and expensive. The advent of quantum mechanics lead to an understanding of how electricity is conducted in semiconductor metals. With this understanding it was possible to see how semiconductors could be used to act as an electrical switch and amplifier, and so the transistor was invented. Further development led to radically smaller and smaller transistors on integrated chips, and transistors sold today can be as small as 5nm across, small enough to fit 4×10^{12} in a square centimetre[2].

Despite this astonishing success, semiconductor electronics is one of only a few quantum technologies developed in the 20th century. It's viability comes down to the robustness of the quantum phenomena that it makes use of. The band structure of electrons in metal, which explains how semiconductor devices work, is a quantum phenomena of rare stability. Electronic band structure exists for systems large enough to see with the naked eye, and without the sensitivity seen in many other quantum systems.

---

[2] That's four thousand billion or $4,000,000,000,000$ per square centimetre

The robustness of electronic band structure is an exception to the rule however. Quantum effects are usually extremely delicate and confined to very small systems, requiring sophisticated experimental techniques to precisely control and isolate from interactions with the system's environment. However experimental abilities are now sufficiently advanced, and theoretical schemes have been devised with large enough benefits, that a huge interest in new quantum technologies has developed.

Two exciting phenomena for making new quantum technologies are *superposition* and *entanglement*. Superposition describes the situation where quantum systems can exist simultaneously in different configurations with different probabilities. The sensitivity of superpositions can be exploited for incredible sensitive metrology, for example in gravity and inertial sensors that use quantum superposition to surpass classical sensors [25, 26]. Another important effect is quantum entanglement, where quantum systems can be correlated with one another in a way not possible in classical mechanics. These quantum correlations have the potential for a wide range of uses - entangled systems can be used to send messages more securely than possible classically, and a large enough quantum computer could crack common encryption protocols faster than much larger supercomputers[3].

Quantum entanglement

Entanglement is a key aspect of quantum mechanics. While quantum theory looks very different to classical mechanics, replacing determinism with probability distributions, many of its features could be explained by assuming that quantum theory simply misses out on something. That if we could expand the theory to capture some crucial layer of detail, then we would have a complete and deterministic theory. Inequalities by Bell and Clauser-Horne-Shimony-Holt [23, 28] take this possibility seriously to place bounds on measurable quantities: if they are exceeded, then there can't be another layer of detail. These inequalities can in fact be violated, and it takes entangled states to do so, making entanglement an important feature that distinguishes quantum from classical mechanics.

The term 'entanglement' was coined by Schrödinger to describe the situation in a many-body quantum state where the best possible knowledge of the system as a whole is more complete than the best possible knowledge of all of its parts. This is counter to classical physics, where a many-body system can be fully accounted for by looking at each of its parts in turn, and Schrödinger described it as '*the* characteristic trait of quantum mechanics' [29].

---

[3] This result and the accompanying algorithm kick-started an enthusiasm for quantum computers that is still going strong today [27].

To demonstrate this, consider a coin laying with either the heads (H) or tails (T) side facing up. Using the notation $|\ \rangle$ to denote the state of the coin, a regular, classical, coin can be in state $|\mathrm{H}\rangle$ (with heads up) or $|\mathrm{T}\rangle$ (with tails up). If we toss the coin and don't look at the outcome, we have a 50% chance of getting $|\mathrm{H}\rangle$ and a 50% chance of getting $|\mathrm{T}\rangle$. If we had tossed two coins there are four possible outcomes: $|\mathrm{HH}\rangle$, where both the first and second coins are heads, $|\mathrm{HT}\rangle$, $|\mathrm{TH}\rangle$, and $|\mathrm{TT}\rangle$. If these coins obeyed the laws of quantum mechanics then more states are available. For example the coins could be in a state like $|\mathrm{HH}\rangle + |\mathrm{TT}\rangle$, where the coins are *simultaneously* both heads and both tails. Writing this means the coins are in this state with 100% probability, however there is a new type of quantum uncertainty about this state. If we look at the first quantum coin, we will be equally likely to find it is heads or tails. Say we see the coin is H, then this collapses the coins,

$$|\mathrm{HH}\rangle + |\mathrm{TT}\rangle \xrightarrow[\text{on first coin}]{\text{measure `H'}} |\mathrm{HH}\rangle,$$

leaving them in the state $|\mathrm{HH}\rangle$. The strange thing is that now the second coin is now *guaranteed* to also be heads-up. The two coins are connected with one another, and can only be described adequately as a whole. Individually the best we could say is that each coin is 50% H and 50% T, but this would miss out on their connection. Quantum states with these properties are *entangled* and these correlations can be manipulated in ways not possible with classical mechanics. For example entangled states can be used to teleport quantum states over vast distances [30].

One important use for entangled states is in quantum computing. Quantum computers can gain an edge over their classical computers because of the existence of entangled states without a classical analogue. In fact, for a collection of quantum digits, there are very many more entangled states than non-entangled states [31]. This expanded set of possible states can be used to design quantum computing algorithms that can be proven to outperform any classical algorithm. The killer application in demonstrating this to the wider world was Shor's algorithm [27], which shows how a quantum computer can factorize large prime numbers exponentially more quickly than classical computers, making use of entangled states [32]. This is an important problem because the difficulty of doing this is the basis for common encryption protocols, for example those used to protect credit card details when shopping online.

Describing quantum systems

The possibility of entangled states means quantum systems can exist in many more configurations than classical systems, which can be used to perform tasks better. However this increased number of possibilities is a double-edged sword, as studying collections of quantum systems involves keeping track of all of these new configurations. This quickly becomes a difficult task.

This is exemplified by considering how computers process information. The base unit of a classical computer is a binary digit, shortened to 'bit', which is a number that takes two values, usually 0 or 1. If $|\text{C bit}\rangle$ is the state of some classical bit, then either $|\text{C bit}\rangle = |0\rangle$ or $|\text{C bit}\rangle = |1\rangle$. A quantum bit, shortened to 'qubit', can exist in a superposition of these two values. To describe its state a number, called the amplitude, must be assigned to each possibility. If the amplitude of $|0\rangle$ is c_0 and the amplitude of $|1\rangle$ is c_1, the state of the qubit is written

$$|1 \text{ qubit}\rangle = c_0|0\rangle + c_1|1\rangle.$$

These amplitudes describe how likely it is, if we were to measure the qubit, that we would find it in state $|0\rangle$ or $|1\rangle$[4].

Now consider what happens if we add another (qu)bit. The classical configurations are easy to list as the first four binary numbers: we can have $|00\rangle, |01\rangle, |10\rangle,$ or $|11\rangle$. Which one we have can be specified with two binary numbers, 0 or 1 for the first qubit and then 0 or 1 for the second qubit. Two qubits however can exist in many more states. If their state is denoted $|2 \text{ qubits}\rangle$, then four amplitudes are required, one corresponding to each classical configuration:

$$|2 \text{ qubits}\rangle = c_{00}|00\rangle + c_{01}|01\rangle + c_{10}|10\rangle + c_{11}|11\rangle.$$

How does this generalize as we go to 3 qubits, 4 qubits, and beyond? Every time we add a bit to the classical system, we only need to give one more number to describe the configuration – is the new bit a 0 or a 1? This doubles the number of possible configurations: we have all of the previous configurations plus the new bit as a 0, and we also have all of the previous configurations plus the new bit as a 1. While the classical description only needs one more number to specify the state, the quantum description needs an amplitude for each possible configuration. Since the number of configurations has doubled, so has the size of the quantum description. This

---

[4] A subtlety here is that it matters *how* we measure. If we perform a measurement that distinguishes $|0\rangle$ and $|1\rangle$, then the probability of each outcome is given by the Born rule [33, 34]: $\text{Prob}(0) = |c_0|^2, \text{Prob}(1) = |c_1|^2$.

Number of (qu)bits	Size of classical description	Size of quantum description
1	2	2
2	3	4
3	4	8
10	10	$2^{10} = 1024$
100	100	$2^{100} \simeq 1.3 \times 10^{30}$
1000	1000	$2^{1000} \simeq 10^{301}$
n	n	2^n

Table 1.1: *Describing quantum and classical bitstrings.* For a given number of (qu)bits, the size of the classical and quantum descriptions are given. Quantum descriptions grow exponentially fast, whereas classical descriptions increase only linearly with the number of (qu)bits. 'Size' here refers to the number of binary digits required in the classical case, and the number of amplitudes required in the quantum case. In fact an amplitude is a more computationally expensive number to work with than a binary digit, and this analysis also ignores details such as the normalization of the quantum state. However as the number of (qu)bits grows the most important fact is the exponential scaling, and at $n = 400$ the information capacity of the entire observable universe is exceeded [35].

simple rule - adding a classical bit requires one more number, but adding a quantum bit requires twice as many numbers - leads to an exponential growth in the size of the quantum description. This growth corresponds to extra quantum possibilities in terms of physics and possible technological applications, but even storing this numbers quickly becomes impossible, as illustrated by Table 1.1

Beating the exponential space requirement: We are seemingly faced with a stark choice: either to give up on the ability to describe quantum behaviour, or to grapple with an exponential storage requirement that limits us to small systems. However there are in fact various ways to get around this exponential space requirement. One way is to find mathematical simplifications, where the quantum effects being studied can be described in a well-suited specialized mathematical framework requiring considerable fewer variables. For example, the quantum behaviour of large numbers of electrons in metals can be analyzed by making use of the regular pattern of the atoms that also make up the microscopic structure. Many quantum effects involving macroscopic numbers of quantum particles have been studied using mathematical simplifications, however they can be difficult, sometimes impossible, to find. Another approach is to make assumptions about the structure of quantum states, and decide which sorts of states are likely to be important.

One such technique, that is used in this research, is to use *tensor network* approximations of the state. These are lightweight descriptions that rule out certain sorts of entanglement. By only capturing some of the possible entanglements in a quantum system the state can be defined with far fewer variables, and physical processes that only make use of such states can be studied to high accuracy. For example, *matrix product states* are one-dimensional tensor network states that have been used to infinite systems in one dimension. Their tensor network structure means they can only describe entanglement between nearby systems well, and fail to capture long-range entanglement. Specifying arbitrary states of infinite 1D systems requires infinite information, but the low-energy physics of such systems requiring only local entanglement has been explained very well using matrix product states [36].

Matrix product states are one of the main tools used in the research presented in this thesis. They are efficient approximations of quantum states with a 1D spatial structure with local entanglement, but can also be expanded to capture arbitrary states at the cost of reintroducing an exponential amount of information. These properties, efficiency for local entanglement and also an ability to tune the information cost with non-locality of entanglement, make matrix product states well suited for studying the dynamics and entanglement of many-body quantum systems.

Interactions with the environment

An important part of the dynamics of quantum systems is interactions they have with their immediate surroundings or environment. While quantum mechanics can offer an authoritative account of so-called ‘closed’ quantum systems, where interactions with the environment are negligible, no quantum system is ever really closed. An ‘open’ quantum system interacts with its environment, and the effect of this can cause a degradation of closed quantum behaviour.

An important problem in the physics of open quantum systems is how quantum systems thermalize. The classical account of how a classical system reaches the same temperature as its environment doesn’t work in quantum mechanics. Classical systems can evolve chaotically, resulting in an ergodic dynamics where the system moves through every possible configuration, leading to thermal equilibrium with its surroundings. Classical bodies are made from microscopic quantum systems, however the quantum mechanics of closed systems does not permit chaotic evolution. How can thermalization be explained at a quantum level, and how does chaotic dynamics emerge from an underlying non-chaotic quantum mechanics? A resolution of this is given by the eigenstates thermalization hypothesis [37, 38, 39], which explains how local properties of a quantum system can thermalize via interactions with the rest of the system, ie interactions with their environment. This suggests that open quantum system effects are of fundamental importance to answering questions of quantum thermalization, and of how classical mechanics emerges from quantum mechanics.

Describing environmental effects in open quantum systems requires different tools from closed system quantum mechanics. A naïve approach of simply describing the combined system and environment as itself a closed quantum systems quickly runs into two difficulties. The first is the exponential scaling of the information required to describe ever larger collections of quantum objects. This is compounded further by the second difficulty, which is that the environment of the quantum system itself has an environment. In an experiment on a quantum system, the experimental apparatus may be taken to be the relevant environment, but this apparatus itself is surrounded by the laboratory it lives in. The laboratory in turn has its own surroundings, and so on. Very soon any hope of a viable analysis is impossible, and in any case would be severe overkill.

Open quantum systems effects are very important for the development of quantum technologies. Many quantum phenomena that are hoped to lead to future quantum technologies rely on a degree of quantum coherence being maintained and preserved from environmental degradation. Understanding how quantum effects are affected by open systems effects helps to combat the effects: either by identifying vulnerable quantum states to avoid and robust states to make use of [5], or else by actively making use of the interaction, for example by using feedback to cancel out its effects [40].

There are many different approaches to studying open quantum systems. Often approximations are made about the environment. Savings can be made by not keeping track of the environment's internal dynamics, typically leading to a statistical account of the system-environment interaction. The exact form of such models varies a lot, but many fall into two broad categories. The first keeps track of each possible outcome of the randomized interactions, evolving an entire probability distribution over quantum states through time. This can be done using the formalism of density matrices, which give a complete statistical account at the expense of a higher information cost and some subtleties of interpretation. The second category looks at individual probabilistic trajectories of quantum states, many of which can be averaged to reproduce the density matrix account of the dynamics. Trajectories can be found more quickly, and can bear a closer resemblance to measured results. The results of quantum experiments often look noisy, and because of the tendency of quantum systems to collapse upon measurements, can exhibit sudden 'jumps'. These effects can also be seen in trajectory-based open quantum system models.

Part of the research presented in this thesis concerns a trajectory-based open systems model, inspired by the Langevin equation from classical mechanics. The classical Langevin has its origins in explaining Brownian motion [41, 42]. This is a randomized motion encountered in many different scenarios, from noisy electronics

---

[5] Indeed for particular types of environment there are known to be 'decoherence-free subspaces' of states that are impervious to open systems effects [30].

to financial markets. The canonical example of Brownian motion is the movement of a grain of pollen under a microscope: such a grain can be observed to undergo sudden changes of direction, to apparently random extents and at random time intervals, as well as a general reduction of speed in between. The explanation is that the grain is colliding with high-speed air molecules that are too small to be seen. The resulting motion is described well by the Langevin equation, where the usual Newtonian dynamics are modified with a random forcing and a frictional effect. This is an example of approximating the environment of an open classical system - rather than keeping track of many air molecules, their effect is approximated by stochastic collisions combined with an overall drag term. A similar model can be used to describe a quantum system coupled to its surroundings. A quantum Langevin equation modifies the closed behaviour of a quantum system with stochastic interactions and a frictional effect, giving a trajectory-based model for an open quantum system. By deriving a quantum Langevin equation over matrix product states, features of both Langevin equations and matrix product states can be used to study entanglement structure in open quantum systems.

Thesis summary and plan

The general aim of this thesis is to study the evolution of many-body quantum systems, to try and understand how open systems effects impact the entanglement structure and thermalization of such systems. The key techiques used involve matrix product states, efficient parameterizations of many body quantum states, and a quantum Langevin model of the environmental interaction. A scratch-built code library in MATLAB and ncon [43] was developed for the research.

The thesis is structured as follows. In the following chapter I introduce matrix product states, discussing their origin, definition, and techniques that have been developed for time evolving them. In chapter 3 I report on an investigation into quantum thermalization, where studying matrix product state dynamics a link is made between quantum thermalization and dynamical chaos. Chapter 4 presents a derivation and implementation of a Langevin equation over matrix product states, which in chapter 5 is be applied to ground state finding, thermal sampling, and a study of entanglement growth. In chapter 6 a detailed study of unstructured searching on a continuous-time quantum computer is presented, where optimization of different physical mechanisms is considered for a realistic machine – of intermediate size and subject to open systems effects. The thesis concludes with a summary discussion in chapter 7.

Chapter 2

Technical Introduction

The Hilbert space of many-body quantum systems grows exponentially with system size. Therefore so does the amount of information required to specify an arbitrary state. This exponential scaling is a significant barrier to numerical treatments, however it can be overcome by describing only the parts of Hilbert space that are important, by formulating a variational parameterization of the Hilbert space. Matrix product states provide one technique for this, and are particularly suited to systems with a one-dimensional geometry whose states exhibit only local entanglement. For a fixed correlation length of entanglement, a matrix product state can be specified with just a polynomial amount of information.

This chapter serves as a technical introduction to many of the methods used later in the thesis. Matrix product states are introduced and defined, and some of the key techniques and algorithms associated with them are explained. In the final section the time-dependent variational principle is discussed as a technique for time-evolving matrix product states, and the key algorithms are explained.

The research presented in this thesis was developed in parallel with a scratch-built code library written in MATLAB with the ncon function, which can be found in the publicly available repository at `https://github.com/JGMorley/mps_langevin`*.*

1 Introduction

Studying a quantum system composed of many subsystems is a difficult task. One of the primary difficulties lies in the size required for a complete description of the system as a whole. This is exemplified by the space requirements for storing the state of classical bits or quantum bits (qubits). The state of n classical bits is perfectly specified by n binary digits taking the value 0 or 1, this bitstring is sufficient to identify which of the 2^n possible states the bits are in. If a bit is added to the system, one extra binary digit is required.

However the state of n qubits requires more information. A probability amplitude must be specified for each of the 2^n possible bit strings, requiring $2^n - 1$ complex numbers (the requirement that the probabilities sum to 1 saves a complex number). If a qubit is added, the number of bitstrings $2^{n+1} = 2 \times 2^n$ is doubled, and therefore twice as many complex numbers need be specified.

This extra information requirement when adding quantum rather than classical systems goes hand in hand with quantum entanglement, where a system can be specified better as a whole then in terms of its parts individually. Specifying an exponential number of probability amplitudes accounts for the possibility that the quantum subsystems might be entangled.

In this section these ideas are fleshed out and the relationship between quantum entanglement and the size of the quantum state is formalized. Following this is a brief survey of methods developed to study the physics of many body quantum systems using approximations of the quantum state that ultimately led to the use of matrix product states.

1.1 Entanglement in many-body quantum systems

1.1.1 Quantum entanglement

The term quantum ‘entanglement’ was first used by Schrödinger in his response to the EPR paradox work [44]. Schrödinger used ‘entanglement’ to describe the situation in a many-body quantum state where the best possible knowledge of the system as a whole is more complete than the best possible knowledge of all of its parts. This is counter to classical physics, and Schrödinger described it as ‘*the* characteristic trait of quantum mechanics’ [45, 29]. It was realized early on in the development of quantum computing that entangled quantum states play a key role, and entanglement quickly became an important concept in the field.

Recent decades have seen the rapid development of a formal theory of quantum information [30] that seeks to quantify the phenomenon of entanglement and the extent to which quantum mechanics can be used to improve of technologies such as computing [6], cryptography [5], sensing and metrology [4]. Entangled quantum systems can be used to perform seemingly miraculous tasks. For example by distributing two entangled systems between parties A and B a large distance apart, it is possible to teleport the quantum state of a third system from A to B [30]. Quantum entanglement is now also used as a tool for understanding condensed matter physics [46], and recent developments are demonstrating how quantum entanglement in a many-body system can be measured directly [47].

Entanglement is defined with respect to partitionings of a composite system into smaller subsystems, which may or may not be entangled with one another. If the system consists of two irreducible parts, then there is only one non-trivial choice, which is to 'bipartition' the system. If there are more than two parts then the systems can be split into more than two pieces, giving rise to multipartite entanglement. However studying multipartite entanglement is much more difficult [48], and so the theory of bipartite entanglement is much better developed, and it is bipartite entanglement that is considered here.

Quantum states that are not entangled are called 'product states', or 'separable'. Complementary to the division of entangled and separable states is the division of 'mixed' and 'pure' states. A pure state, usually denoted as eg. $|\psi\rangle$, indicates the configuration of a system with zero uncertainty. A classical distribution $\{p_i\}$ over quantum states $|\psi_i\rangle$ can be described with a density matrix or operator $\hat{\rho} = \sum_i p_i |\psi_i\rangle\langle\psi_i|$. If the distribution is non-trivial, then the state is said to be 'mixed'. Entanglement for mixed states is hard to define without mixing up classical and quantum uncertainty. In this thesis pure states are implied unless explicitly stated otherwise.

Insight into the bipartite entanglement of a pure state can be extracted from the singular value properties of its matrix representation. Broadly, if one writes a matrix of coefficients C_{i_A,i_B} - one index each for the two subsystems A, B - the singular values of this matrix tell us directly about the entanglement between A and B. If there is just one non-zero singular value then A and B can be measured separately to yield a full description of the system, whereas if they are evenly spread then measurements of A and B yield uniformly random results that give no information about state of the system as a whole. To give two brief examples, the separable two-qubit state $(|00\rangle + |01\rangle)/\sqrt{2}$ has singular values $(1, 0)$, whereas the maximally entangled Bell state $(|00\rangle + |11\rangle)/\sqrt{2}$ has even singular values $(\frac{1}{\sqrt{2}}, \frac{1}{\sqrt{2}})$. By considering the singular value decomposition of C_{i_A,i_B} as probabilities for a sequence of letters formed by the corresponding basis states, techniques from information science can be used to quantify and study quantum entanglement [49].

1.1.2 Defining entanglement

Generally a composite system may be split into two subsystems A and B. Denoting local orthonormal bases for each system as $\{|i_A\rangle\}$ and $\{|i_B\rangle\}$, a generic state of the overall system may be written

$$|\psi_{AB}\rangle = \sum_{ij} c_{ij} |i_A\rangle \otimes |j_B\rangle , \tag{2.1}$$

where $\otimes$ denotes the tensor product [30] and usually won't be explicitly written from here on.

One way to study such a state is by considering the reduced density matrix of one of the subsystems. Eg, the reduced density matrix of subsystem A is given by

$$\rho_A = \sum_k \langle k_B|\psi_{AB}\rangle \langle\psi_{AB}|k_B\rangle = \sum_{ij} \rho_{ij} |i_A\rangle \langle j_A| , \tag{2.2}$$

where $\rho_{ij} = \sum_k c_{ik}\overline{c_{kl}}$, and an over-line denotes complex conjugation.

Measures of the entanglement between the two subsystems can be calculated from this reduced density matrix. The most common measure is the von Neumann entanglement entropy, which is calculated as

$$S(\rho_A) = -\mathrm{Tr}(\rho_A \log_2 \rho_A). \tag{2.3}$$

The von Neumann entropy is zero in the limit of unentangled states [30].

There is a freedom of representation in how we write down the bipartite quantum state in terms of local bases $\{|i_A\rangle\}$ and $\{|i_B\rangle\}$ for subsystems A and B in (2.1) - any choice of basis will do, and will correspond to a different set of amplitudes c_{ij}. In fact, it is always possible to choose bases so that the sum is diagonal, ie. $c_{ij} = \delta_{ij}c_{ii}$, and in this case the coefficients c_{ij} can be interpreted as telling us directly about the entanglement in the system. This is a result of the singular value decomposition theorem in linear algebra, which can be stated as the following [50]:

Singular Value Decomposition. *If A is a complex matrix $\in \mathbb{C}^{m\times n}$, then there exist unitary matrices $U \in \mathbb{C}^{m\times m}$ and $V \in \mathbb{C}^{n\times n}$ such that*

$$U^\dagger A V \equiv \Sigma = \mathrm{diag}(\lambda_1, \lambda_2, \ldots, \lambda_p) \in \mathbb{R}^{m\times n}, \tag{2.4}$$

where $p = \min\{m, n\}$ and $\lambda_1 \geq \lambda_2 \geq \cdots \geq \lambda_p \geq 0$.

Thus the complex matrix A can be written as $A = U\Sigma V^\dagger$, where the non-zero elements of Σ are the singular values of A. The number of singular values $p =$

$\min\{m,n\}$ is also known as the rank of A. The singular value decomposition can be applied directly to the matrix c_{ij} appearing in the bipartite state (2.1), yielding a diagonal sum over the singular values λ_k of c and unitary rotations of the local bases for A and B. Since unitary rotations preserve the inner product, the transformed basis states still form an orthonormal basis. This result is known as the Schmidt decomposition, which can be stated as [30]:

Schmidt Decomposition. *A (normalized) joint state $|\psi_{AB}\rangle$ of a composite system AB can be written in terms of orthonormal states $|k(A)\rangle$ for subsystem A and $|k(B)\rangle$ for subsystem B as*

$$|\psi_{AB}\rangle = \sum_k \lambda_k \, |k(A)\rangle \, |k(B)\rangle \,, \tag{2.5}$$

where λ_k are non-negative real numbers satisfying $\sum_k \lambda_k^2 = 1$ known as Schmidt coefficients or Schmidt values.

The spectrum of Schmidt coefficients tell us quite directly about the entanglement properties of the state. If $\lambda_1 = 1$, then $\lambda_{k\neq 1} = 0$ and the state $|\psi_{AB}\rangle = |k(A)\rangle \, |k(B)\rangle$ is unentangled. It is easy to see that the von Neumann entanglement entropy is zero-valued for this state. It is maximal when all λ_k are equal, and therefore states with large amounts of bipartite entanglement between A and B are characterized by a flat distribution of Schmidt coefficients. In terms of Schmidt values, the von Neumann entanglement entropy between A and B can be written as

$$S(|\psi_{AB}\rangle) = -\sum_k \lambda_k^2 \log_2 \lambda_k^2. \tag{2.6}$$

1.1.3 Entanglement in many-body quantum systems

The research presented in this thesis primarily concerns systems comprised of many discrete systems. The entanglement in such a system is subtle, as it depends on which of many possible bipartitionings are chosen. Some overall insight can be gained from simply considering the Hilbert space of such systems, as for example the dimensionality of the smallest partitioned subsystem constrains the maximum possible entanglement between it and the rest of the system.

Consider a single qubit (or any other two-level system) with state $|\psi\rangle$. A well-known representation for the Hilbert space of the qubit is to map it to the surface of a unit sphere (often called the 'Bloch sphere'), with coordinates given by $(x,y,z)^\intercal = \langle\psi|\hat{\vec{\sigma}}|\psi\rangle$ in terms of the Pauli matrices $\hat{\vec{\sigma}} = (\hat{\sigma}_x, \hat{\sigma}_y \hat{\sigma}_z)^\intercal$. This gives a pleasing graphical representation for qubit states and their trajectories, and even mixed states are captured as points with radius less than one. However finding visualizations for even more qubits gets increasingly difficult, not least because of the exponentially scaling dimensionality of their Hilbert space: for N systems each with local Hilbert space dimension d_n, the total Hilbert space has dimension $\dim(\mathcal{H}) = \prod_{n=1}^{N} d_n$.

In many situations, such as for open quantum systems, the entanglement in many-body quantum systems follows general patterns. If the Hamiltonian has only localized terms, then this places limits on how quickly long-range entanglement can be generated. Often the long-range entanglement in an open quantum system will deteriorate most quickly, which can lead to a finite entanglement correlation length in such systems. This idea can be quantified by categorizing states according to how the entanglement S_{AB} between a region A and the rest of the system B scales with the size of A. If entanglement only exists over short distances, then only parts of A and B close to the boundary will contribute to S_{AB}, which will therefore scale with the area of this boundary. This is known as area-law entanglement. On the other hand, if long-range entanglement exists then all parts of A can be entangled with parts of B, resulting in S_{AB} scaling with the total size of A. This is known as volume-law entanglement [51].

1.2 Origins of entanglement-based parameterizations

One of the key techniques used in this project is matrix product state methods. Here I summarize how matrix product states were originally found to be useful for finding ground states of condensed-matter problems, before going on to discuss their technical aspects in Sec 2.

Advances in quantum information began to develop rapidly, and help with condensed matter problems, shortly after important work on quantum teleportation in the early 1990s [46, 52, 30]. At about the same time a breakthrough was made in numerical methods for finding the ground states of condensed matter models. This breakthrough was the introduction of the density matrix renormalization group (DMRG) technique by White in 1992 [53]. This work improved on the previous standard, renormalization group (RG) techniques, which were introduced in 1975 by Wilson [54] to help find ground states of the Kondo impurity model in one dimension [55]. While Wilson's RG was successful for this, and for other impurity problems, when applied to other problems it often failed [56]. Both of the methods for finding ground states involve 'blocking' the system into small subsystems and processing these smaller blocks individually, before truncating the output and recombining. In the truncation step, the renormalization group method takes the block Hamiltonian and truncates to only the low energy components. It was found however that this fails to adequately describe the effects of the neighbouring blocks in a real-space lattice problem [57]. DMRG improves on this by taking the low energy states of the block, dividing the block into ‘system’ and ‘environment’ sub-blocks, computing the reduced density matrix of the system block, then retaining only the high-probability components of that density matrix. DMRG proved to be successful for a wide range of applications and quickly became established as the most powerful numerical method for one-dimensional quantum lattice problems [58]. Efforts to understand the remarkable success of DMRG methods led to the realization that DMRG is equivalent to finding the best MPS description of the ground state, thus cementing MPS as an invaluable tool for studying strongly coupled systems in one dimension.

1.3 Chapter summary

The remainder of this chapter sets out key definitions and techniques for working with matrix product states. In Sec. 2 definitions are given for finite and infinite matrix product state parameterizations, and the graphical tensor notation commonly used is illustrated. One feature of working with matrix product states is that particular gauge choices, or ‘canonical forms’, for the parameterization yield direct information about the entanglement in the system, and Sec. 2 continues by exploring this in more details and giving key algorithms for working with matrix product states. In Sec. 3 the time-dependent variational principle for evolving matrix product states is discussed, and key algorithms for implementing this for finite and infinite systems are given. This concludes with a discussion of how the code written for this research was validated against many-body dynamics which have been solved analytically.

2 Matrix product states

A practical solution to the problem of storing many body quantum states is provided by matrix product states. Matrix product states (MPS) allow for smaller, partial descriptions that capture states with localized entanglement. Moreover the size of a matrix product state can be increased or decreased to allow for more or less entangled states, spanning product states to arbitrary states in the Hilbert space. In this section matrix product states are defined and the common pictorial notation for describing their use is introduced. Then the standard techniques for manipulating matrix product states are explained. I start with how gauge freedoms are used to simplify calculations, and go on to discuss a number of important algorithms in their use. Finally I explore extensions of matrix product states to two dimensions, and to mixed states.

2.1 Definitions and notation

We start with the standard way of writing down the pure state of a many-body quantum system. This is done by writing a superposition over a complete basis for the system, which in turn is a composition of basis states for the individual systems. Throughout 'system' is used to refer to the system as a whole, and 'site' is used to refer to one of these subsystems. A generic pure state of such a system of N sites is

$$|\psi\rangle = \sum_{\sigma_1 \dots \sigma_N} = c_{\sigma_1 \dots \sigma_N} |\sigma_1 \cdots \sigma_N\rangle, \tag{2.7}$$

where $\{|\sigma_n\rangle\}$ is a basis for the nth site, indexed by σ_n. Here all the information is stored in the rank-N tensor of probability amplitudes, c. The number of elements in c is exponential in the system size: if the nth basis has dimension d_n, then the number of elements in c is $\prod_n d_n$, with the only redundancy being an overall phase factor.

Matrix product states are a variational parameterization of c, and are a particular example of 'network states'. The idea here is to decompose the (fully general) probability amplitude tensor c into a sub-exponential network of tensors. By finding a tensor network that effectively parameterizes a region of Hilbert space that is of interest, it is possible to make a numerical study of many-body quantum system without the burden of an exponentially scaling description. Matrix product states use a simple one-dimensional tensor network that provides a good description for locally entangled systems of a similar geometry.

2.1.1 Defining the matrix product state parameterization

A naïve parameterization would be to replace each of the amplitudes with a product of N complex numbers, like so

$$c_{\sigma_1\sigma_2\ldots\sigma_\mathrm{N}} = a^{[1]}_{\sigma_1} a^{[2]}_{\sigma_2} \ldots a^{[\mathrm{N}]}_{\sigma_\mathrm{N}}. \tag{2.8}$$

The number of degrees of freedom now increases only linearly with N, so this parameterization removes the exponential barrier to constructing the dynamics: the number of degrees of freedom is decreased from $\prod_n d_n$ to $\sum_n d_n$ which becomes a simple linear scaling dN if each local system has the same dimension d. However it is easily shown that this corresponds to a restriction to unentangled product states $|\psi\rangle = |\psi_1\rangle|\psi_2\rangle\cdots|\psi_N\rangle$, with $|\psi_n\rangle = \sum_{\sigma_n} a^{[n]}_{\sigma_n}|\sigma_n\rangle$. Though efficient, this parameterization therefore can't describe entangled states and so is not very useful.

A useful tool in analyzing tensor contractions is to represent them graphically, as summarized in Fig 2.1. In the graphical notation this looks like In this notation the product state parameterization (2.8) looks like the following:

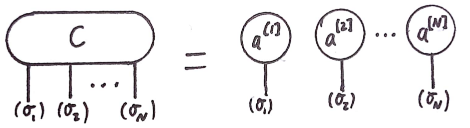

(2.9)

This notation highlights the independence of each local system, and hence the separability of the state. It is also suggestive of an improvement to the parameterization: introduce additional 'legs' (indices) connecting the local tensors. This would allow a co-dependence of the systems and hence describe a certain amount of entanglement. That is, let us parameterize the quantum amplitudes of our many-body system as

$$c_{\sigma_1\sigma_2\ldots\sigma_\mathrm{N}} = \underline{A}^{[1]\sigma_1\,\mathrm{T}}\,\underline{\underline{A}}^{[2]\sigma_2}\ldots\underline{\underline{A}}^{[\mathrm{N}\text{-}1]\sigma_{\mathrm{N}\text{-}1}}\,\underline{A}^{[\mathrm{N}]\sigma_\mathrm{N}}, \tag{2.10}$$

where a single underline denotes a vector and a double underline denotes a matrix. This parameterization defines a 'matrix product state'. Writing out the same equation in our pictorial notation we have:

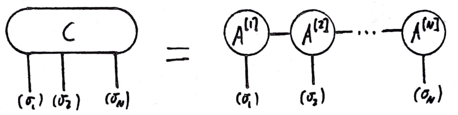

(2.11)

In a matrix product states the local amplitudes of a product state a_{σ_n} have become

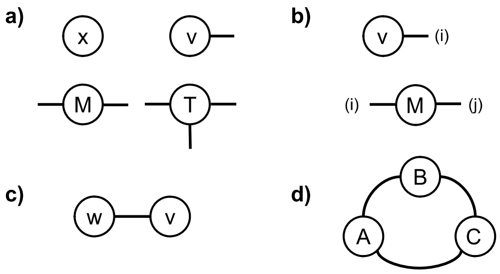

Figure 2.1: *Graphical representations of tensors and their contractions.* a) Tensors can be represented as labelled shape – in this case a circle – with indices represented by protruding legs. Here x is a number and doesn't have any indices. Vector v, matrix M, and tensor T have $1, 2, 3$ indices respectively. b) Particular elements of a tensor can be indicated by labelling the legs with the value taken by each index. Here v_i and M_{ij} are represented. c) Contractions of indices can be indicated by simply joining the respective legs. Here the indices of two vectors are joined to represent $\underline{w}^\intercal \underline{v} = \sum_i w_i v_i$. d) Using this more straightforward notation for tensor contractions can reveal interesting properties. Here we see an illustration of the cyclicity of the trace: $\sum_{ijk} A_{ij} B_{jk} C_{ki} = \mathrm{Tr}(ABC) = \mathrm{Tr}(BCA) = \mathrm{Tr}(CAB)$.

rank-3 tensors: the tensor for the nth site is written as $A^{[n]\sigma_N}_{ij}$. Here the physical index σ_n remains, but additional indices i, j are introduced. These 'auxiliary' or 'bond' indices are contracted between tensors, and allow the matrix product states to describe correlations between different sites.

An important parameter of a matrix product state of the 'bond dimension', D. This is equal to the maximum allowed number of auxiliary index values, across all auxiliary indices. By tuning the bond dimension the Hilbert space can be mapped out in discrete steps: if $D = 1$ we have the manifold of product states, and as D is increased more and more entanglement is permitted, until eventually an arbitrary state can be described.

2.1.2 Calculating expectation values

Some of the most important quantities to calculate are expectation values. As a generic example, take an operator $\hat{\mathcal{Q}}_{[n:n+\Delta]}$ that acts trivially only on sites $n, \ldots, n+\Delta$. Using the convention that conjugate tensors are written upside-down, this calculation looks like

$$\langle \psi | \hat{\mathcal{Q}}_{[n:n+\Delta]} | \psi \rangle =$$

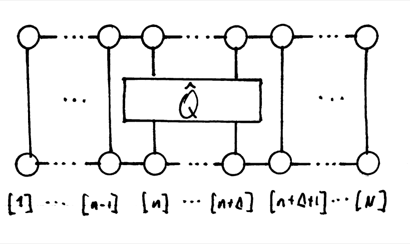

, (2.12)

where the site indices have been indicated in square bracket below the RHS.

The number of basic operations required to perform such tensor contractions depends on the order in which the sums over the various indices are performed. For example in calculating the expectation of the local operator (2.12) the fastest method is to start at one end, say the right, and contract in the following order: (1) the Nth physical index, (2) the $(N-1)$th physical index, then (3) both the $(N-1)$th auxiliary indices, and so on. This process is made more clear in diagrammatic form:

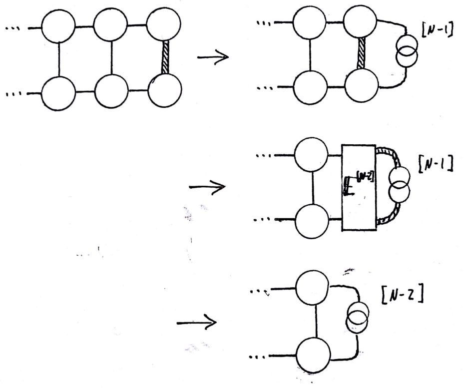

$$, \tag{2.13}$$

where the thicker, dashed line indicates which index is contracted in each step. Here two new tensors are introduced, a labelled rectangle indicating the transfer matrix, and two interlocking circles that for a label $[n]$ is the result the contraction of all the state tensors with site index greater than n. This object we refer to as the 'right environment' for the nth site. This can be defined by the recursive relation

$$r^{[n\text{-}1]}_{i_{n\text{-}1} j_{n\text{-}1}} = \sum_{\sigma_n} \sum_{i_n j_n} A^{[n]\sigma_n}_{i_{n\text{-}1} i_n} r^{[n]}_{i_n j_n} \overline{A^{[n]\sigma_n}_{j_{n\text{-}1} j_n}}, \tag{2.14}$$

or

$$\underline{\underline{r}}^{[n\text{-}1]} = \sum_{\sigma_n} \underline{\underline{A}}^{[n]\sigma_n} \underline{\underline{r}}^{[n]} \left(\underline{\underline{A}}^{[n]\sigma_n} \right)^{\dagger}, \tag{2.15}$$

and the boundary condition $R^{[\mathrm{N}]} = 1$.

Considering the analagous contraction from left to right we end up with a corresponding 'left environment' for each n that is the result of the contraction of all MPS tensors with site index less than n. The left environment of the nth site we denote $l^{[n]}$ and is defined by the end condition $l^{[1]} = 1$ and the recursive relation

$$\underline{\underline{l}}^{[n+1]} = \sum_{\sigma_n} \left(\underline{\underline{A}}^{[n]\sigma_n} \right)^{\dagger} \underline{\underline{l}}^{[n]} \underline{\underline{A}}^{[n]\sigma_n}. \tag{2.16}$$

So in practice as well as storing the MPS tensors $\{A^{[n]}\}$ the left and right environments for each site $\{R^{[n]}, L^{[n]}\}$ are also stored. Thus for (2.12) with $\Delta = 0$ the contraction would involve just 5 tensors, $A^{[n]}$, $\overline{A^{[n]}}$, $Q^{[n]}$, $r^{[n]}$ and $l^{[n]}$:

$$\langle \hat{Q}^{[n]} \rangle =$$

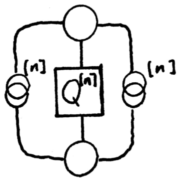

$$. \qquad (2.17)$$

2.1.3 Open, periodic, and infinite matrix product states

This general prescription for writing down a matrix product states can be used a few different ways in practice. Here I briefly discuss how matrix product states can look for finite systems, and infinite systems where $N \to \infty$.

Finite matrix product states

Matrix product states can be used to describe systems of a fixed number N of sites. By truncating the bond dimension, larger systems can be studied than via storing the probability amplitudes $c_{\sigma_1 \ldots \sigma_N}$ in full. This truncation works best for locally entangled systems in one dimension.

There is a choice of what to do with the end tensors. So far we have worked with the assumption that these obey open boundary conditions. Another option would be to have the 1st and Nth sites connected via an auxiliary index, leading to a periodic matrix product state. Throughout this thesis we will work with matrix product states with open boundary conditions.

Infinite matrix product states

For systems with a local homogeneous interaction, states can often be described with a fixed bond dimension matrix product states with a repeating unit cell. This affords a tractable description of bulk effects in a $N \to \infty$ limit [59, 60].

As long as only local expectation values are important, the end tensors become irrelevant. This can be seen by considering the 'transfer matrix', $\mathbb{E}_{(ii'),(jj')} = \sum_\sigma A^\sigma_{ij} \bar{A}^\sigma_{i'j'}$ for a one-site unit cell. A local expectation away from the ends of the system will involve raising $\mathbb{E}$ to a very high power. The result is dominated by a unique largest eigenvalue[1]: $\mathbb{E}^k \approx \lambda_1^k |R_1\rangle\langle L_1|$ with dominant right- and left-eigenvectors $|R_1\rangle$,$\langle L_1|$. These are the environments of the matrix product state and contract with the relevant part of the state as in Eq 2.17. The leftover environment on either side contracts with the rest of the chain to provide an overall phase factor equal to the norm of the

---

[1] If one exists. It turns out that the existence of a unique largest eigenvalue is a necessary condition for the state to be well described by a matrix product state in the first place [59].

state. The end tensors can therefore be ignored, and the state described simply by a rank-3 tensor A having dD^2 elements, where D is the bond dimension and D the local physical dimension. Extracting the left and right environments as the dominant eigenvectors of the transfer matrix $\mathbb{E}$ gives insight into the entanglement in the system[2] and allows for easy calculation of local expectation values.

2.2 Gauge choices

As touched on above, a pure quantum state has a gauge freedom in the form of an overall phase factor: the mapping $|\psi\rangle \rightarrow e^{i\phi}|\psi\rangle$ has no effect on any physical expectation. Matrix product states have much more freedom, and by taking advantage of this can be transformed into so-called ‘canonical’ forms that simplify many important contractions.

2.2.1 Gauge freedoms in matrix product states

A matrix product state is unchanged if a resolution of the identity matrix is inserted at any of the bond indices. That is, all tensors $A^{[n]}$ could be altered by $A^{[n]\sigma_n} \rightarrow M^{[n-1]-1}A^{[n]\sigma_n}M^{[n]}$, where for each n we have $M^{[n]}M^{[n]-1} = \mathbb{1}$, with $\mathbb{1}$ the identity.

This gauge freedom can be taken advantage of to simplify many commonly occuring contractions involving the matrix product state tensors, including those for calculating expectation values. By careful choices of gauge, many of the environments can be made trivial, and the Schmidt spectra and hence entanglement at each bond index can be extracted straightforwardly. These canonical forms for the matrix product states can elucidate the entanglement structure in the state, and are necessary for some important matrix product state algorithms[3].

2.2.2 Canonical gauge choices

Here I give a brief overview of the canonical forms used in this thesis. More detail, and algorithms for canonicalization of a matrix product state, can be found in [61, 62, 63].

Vidal form

The first canonical form, first defined by Vidal [63], contains the essential ideas of all the canonical forms discussed here. In the Vidal form, the matrix product state is

---

[2] via the Schmidt decomposition theorem.

[3] e.g. time-evolving an infinite matrix product state via the time-dependent variational principle, as discussed in Sec 3

decomposed as

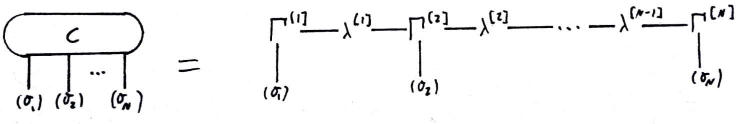

. (2.18)

The Γ and λ tensors satisfy the requirements of a Schmidt decomposition at each cut of the system into two contiguous parts: at the nth cut we have $|\psi\rangle = \sum_k \lambda^{[n]}_{kk} |L^{[1..n]}_k\rangle |R^{[n+1..N]}_k\rangle$, where the orthogonal bases $\{|L^{[1..n]}\rangle\}$, $\{|R^{[1..n]}\rangle\}$ are described by contracting the Γ and λ tensors either side of $\lambda^{[n]}$. The λ matrix itself is a diagonal matrix of the singular values of the state tensor grouped accoring to the partitioning, $c_{(\sigma_1,\ldots,\sigma_n),(\sigma_{n+1}\cdots\sigma_N)}$. These properties mean that the entanglement at each cut is easy to calculate as

$$S(n\text{th cut}) = -\sum_k \lambda^2_{kk} \log_2 \lambda^2_{kk}, \tag{2.19}$$

and moreover that contractions of the system environment to the right and left of the nth site are greatly simplified by the orthogonality condition, leading to the following:

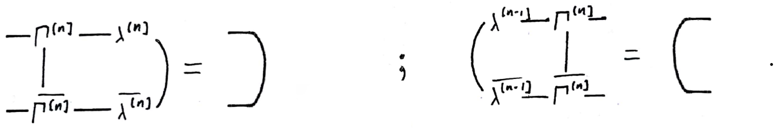

. (2.20)

Efficient algorithms exist for converting a generic state to a Vidal form matrix product state, and for converting a non-canonical matrix product state into Vidal form [58]. The properties that the Γ tensors and λ matrices inherit from the singular value decomposition theorem underlie the usefulness of the remaining canonical forms, which can be expressed in terms of them.

Left- and right-canonical forms

The idea behind the left- and right-canonical forms is to group Γ and λ tensors in order to make either all the left or all of the right environments trivial. For right canonical form this can be achieved by setting

$$\underline{\underline{A}}^{[n]\sigma_n} = \underline{\underline{\Gamma}}^{[n]\sigma_n} \underline{\underline{\lambda}}^{[n]}. \tag{2.21}$$

The effect of this is to make contractions of the right environments trivial ($\underline{\underline{r}}^{[n]} = \mathbb{1}$), and the left environments diagonal matrices with the corresponding squared Schmidt spectrum as the diagonal elements: $\underline{\underline{l}}^{[n]} = \underline{\underline{\lambda}}^{[n-1]2}$.

Similarly, a matrix product in left canonical form satisifes

$$\underline{\underline{A}}^{[n]\sigma_n} = \underline{\underline{\lambda}}^{[n-1]}\underline{\underline{\Gamma}}^{[n]\sigma_n}. \tag{2.22}$$

In left canonical form the left environments are the identity, and the right environments give the squared Schmidt spectrum: $\underline{\underline{l}}^{[n]} = \mathbb{1}$, $\underline{\underline{r}}^{[n]} = \underline{\underline{\lambda}}^{[n]}$.

Central canonical gauge

A final combination of Vidal form tensors is the central canonical form, which is useful when time-evolving finite-system matrix product states via the time-dependent variational principle [64]. In the central canonical form for the nth site, we have

$$\underline{\underline{A}}^{[n]\sigma_n} = \underline{\underline{\lambda}}^{[n-1]}\underline{\underline{\Gamma}}^{[n]\sigma_n}\underline{\underline{\lambda}}^{[n]}, \tag{2.23}$$

while tensors for sites $> n$ are in right canonical form, and sites $< n$ are in left canonical form. This means that for the nth site only, both right and left environments are the identity matrix. As we will see in Sec 3, this will be useful in avoiding inversion of Schmidt values in a particularly useful gauge choice for tangent vectors for variations on the nth site[4].

Unitary gauge

A related alternative gauge choice is motivated by considerations of tangent vectors for variations on each site. The time dependent variational principle evolution of matrix product states involves calculating ‘orthogonal’ tensors to each $\underline{\underline{A}}^{[n]}$. Specifically, an orthonormal set of vectors $\underline{\underline{v}}^k$ which satisfy $\sum_\sigma \underline{\underline{A}}^{\dagger\sigma}\underline{\underline{l}}^{\frac{1}{2}}\underline{\underline{v}}^k = 0$. The idea of the unitary gauge is to store the state tensor and these orthogonal tensors as the mutually orthonormal columns of a unitary matrix $\underline{\underline{U}}^{(i\delta),(\sigma j)}$, indexed by δ such that $U^{\delta=1} = A$ and $U^{\delta\neq 1} = v^\delta$.

This could prove to be useful when evolving matrix product states via the time-dependent variational principle, saving time by evolving both the state tensors and also the tangent space tensors. This unitary gauge choice is used when deriving a path integral over MPS in [65], a result we will build on in Chapter 4. It is also a natural choice when putting MPS on a quantum computer [66]. The term ‘unitary gauge’ is not in general use but has been adopted by our research group.

---

[4] This is desirable because it allows evolution through state where one or more Schmidt values are equal to or close to zero.

2.3 Properties of matrix product states

Matrix product states are parameterizations of a many-body state $|\psi\rangle$ that can offer a tuneable trade-off between the number of degrees of freedom and the degree of entanglement that can be captured. This can be seen directly in the $\underline{\underline{\lambda}}$ matrices described above: square diagonal matrices of dimension limited by the bond dimension of the matrix product state. The diagonal elements are the Schmidt values, amplitudes of the distribution of the corresponding orthogonal Schmidt basis of sates, from which the entanglement entropy can be calculated. The maximum possible entanglement for a normalized state is capped by the bond dimension. Normalization requires $\sum_k \lambda_k^2 = 1$, and the von-Neumann entropy is maximized by a flat distribution $\lambda_k = 1/\sqrt{D}$ giving an entropy of $S_{\max} = \log_2 D$.

The set of possible states described by a matrix product state will include the entire Hilbert space if the bond dimension is sufficiently large. The value required for this increases exponentially with the system size. However in one-dimensional spin-chain models, where the Hamiltonian exhibits a gap between the ground and excited states, the low energy states are known to obey an area law for entanglement, ie. the entanglement in such states is fixed as system size increases[62]. This makes matrix product states with a fixed bond dimension a good approximation for such states, even in the limit of infinite system size.

From a practical point of view, matrix product states are useful because storage and calculations with them are efficient. Storing N tensors with bond dimension D and physical dimension D requires just ND^2d parameters, rather than the exponential d^N number of parameters required for a full description. Calculating local expectation values is straightforward as those sites not involved can be reduced to 'environment' matrices $\underline{\underline{r}}, \underline{\underline{l}}$ as described in Eq 2.13[5] can be calculated in advance an re-used for many calculations on the state. Alternatively the state can be transformed into one of many useful canonical gauges, where these environments can be made equal to the identity, further simplifying calculations.

Matrix product states are a powerful tool for describing states with localized entanglement. However many questions about many body quantum systems involve dynamics. In the following section we show how matrix product states can be used to study the dynamics of many body quantum systems.

---

[5] The efficiency of this does not translate well to two dimensions. For example, projected entangled pair states are described by a square-grid tensor network, and the corresponding environments in such states look like entire matrix product states rather than D^2 square matrices [62].

3 Time-dependent variational principle

In this section we show how the time-dependent variational principle can be used to find equations of motion for matrix product states, and discuss algorithms for integrating these equations forwards. Finally we illustrate this using the code written for this research and explain how the time-dependent variational principle was implemented and tested.

3.1 The time-dependent variational principle (TDVP)

The time-dependent variational principle (TDVP) provides a route to time-evolving variational parameterizations of a quantum state. Here we write this as $|\psi(z)\rangle$, where z represents a collection of complex-valued parameters. The TDVP was first used by Dirac in 1930 to derive the time-dependent Hartree-Fock equations, often used in quantum chemistry to parameterize molecular electron orbitals [67, 68, 69, 70].

Time-evolving such parameterizations via the Schrödinger equation $\partial_t|\psi\rangle = -i\hat{H}|\psi\rangle$ is generally not possible. We have a restriction that we can only describe states within the manifold defined by our parameterization $|\psi\rangle = |\psi(z)\rangle$, so the time-derivative of the state looks like $|\partial_t\psi\rangle \simeq \sum_k |\partial_{z_k}\psi\rangle\, \dot{z}_k$. However the application of the Hamiltonian operator will in general lead to a derivative that can't be described in this way. The solution, due to Frenkel [68], is to take an inner product of the two terms with an arbitrary variation of the state, which can be written $|\delta\psi\rangle = \sum_k |\partial_{z_k}\psi\rangle\, \delta z_k$, with the vector of variations δz_k arbitrary. This leads to equations of motion for the variational parameters $z_k(t)$, which minimize[6] $||\hat{\mathcal{H}}\,|\psi\rangle - i\partial_t\,|\psi\rangle\,||$ at each point in time [71]:

$$i\sum_j \langle \partial_{\overline{z_k}}\psi|\partial_{z_j}\psi\rangle\, \dot{z}_j = \langle \partial_{\overline{z_k}}\psi|\mathcal{H}|\psi\rangle\,. \tag{2.24}$$

These equations can be thought of as optimizing a projection of the tangent state $-i\hat{H}|\psi\rangle$ onto the tangent space of the variational manifold, in such a way that the fidelity error is minimized.

The resulting TDVP trajectories form a symplectic manifold, that is, a classical phase space. This comes with its own conserved quantities, even when the full quantum dynamics can't be realized. In particular, the TDVP equations are inherently energy conserving. These conservations properties make the TDVP method of time-evolving matrix product states particular suited to situations where long-time evolution is of interest [72].

Here I give overviews of a few different ways of evolving matrix product states via

---

[6] Where the norm indicated here is the usual Fidelity measure for pure states: $|||\phi\rangle|| = |\langle\phi|\phi\rangle|^{1/2}$.

the TDVP. The key trick is a useful parameterization of the tangent space vectors, first reported in [72]. By using a basis of tangent vectors which are orthogonal to the state vector and to eachother, the matrix $G_{ij} = \langle \partial_{\bar{z}_k} \psi | \partial_{z_j} \psi \rangle$ in Eq 2.24 is simplified. In the basis of site index this becomes proportional to the identity, decoupling the equations for $\dot{A}^{[n]}$. This makes evolution of infinite matrix product states tractable, and greatly simplifies evolution of finite systems.

The discussions given in sections 3.2.1, 3.2.2 and 3.2.3 summarize the full presentations given in [72, 64], highlighting the key aspects used in this thesis.

3.2 Applying TDVP to matrix product states

Here I mainly describe the original implementation due to Haegeman et al in [72]. More modern approaches have followed, which will be touched on briefly. This discussion is intended to demonstrate the content and considerations of the method.

3.2.1 Parameterizing the tangent space

The TDVP equations for the tensors A of a matrix product state can be decoupled with the following parameterization of the tangent space. Only updates $A \to A + dA$ that are orthogonal to the state are considered, which is achieved by imposing a 'left-tangent gauge' condition: $\sum_\sigma A^{\dagger\sigma} l dA^\sigma = 0$. It is straightforward to see that this leads to $\langle \psi | \delta\psi \rangle = 0$ by considering contractions from the left, where the tangent state $|\delta\psi\rangle$ corresponds to replacing A with dA.

To do this $\dot{A}$ is written as a linear combination of an orthonormal set of vectors $\underline{\underline{V}}^k$ which satisfy $\underline{\underline{A}}^\dagger \underline{l}^{\frac{1}{2}} \underline{\underline{V}}^k = 0$, where A has been reshaped as $[\underline{\underline{A}}]_{(i\sigma),j} = A^\sigma_{ij}$ and similarly for $\underline{\underline{V}}^k$. To ensure the equations fully decouple, the tangent state is parameterized as the following:

$$\underline{\underline{\dot{A}}}^\sigma = \underline{l}^{-\frac{1}{2}} \underline{\underline{V}}^\sigma \underline{\underline{\dot{X}}} \, \underline{\underline{r}}^{-\frac{1}{2}}, \tag{2.25}$$

where now V is written with the physical index σ free and the orthonormal vector index k contracted with $\dot{X}$, *ie* $[\underline{\underline{V}}^\sigma]_{i,(kj)} = V^{\sigma k}_{ij}$. Sometimes it will be convenient to treat V and $\dot{X}$ in terms of a greek index δ over a full basis, so that $\delta = 1$ indexes the original state vector and $\delta \neq 1$ the orthogonal vectors. In this case they will be written as variants of $V^{\sigma(\delta\neq1)}_{ij}$ and $X^{(\delta\neq1)}_{ij}$.

The next step is to contract the open indices of $\langle \partial_{\bar{A}_k} \psi |$ on either side of the TDVP equation with all parts of this parameterization *apart from* $\dot{X}$. This now becomes $\langle \partial_{\bar{X}} \delta\psi |$, where $\langle \delta\psi |$ is a tangent state under the left-tangent gauge. The result is that the TDVP equations for each site decouple, and we have

$$\dot{X} = -i\langle \partial_{\bar{X}} \delta\psi | \hat{H} | \psi \rangle. \tag{2.26}$$

3.2.2 Infinite matrix product states

An infinite, homogeneous matrix product state can be time-evolved this way. Care needs to be taken when evaluating the RHS of Eq 2.26 for a repeating Hamiltonian of single-site and two-site terms, as detailed in [72]. One issue with evolving in this way come from the inversion of l and r environments in Eq 2.25: if one or more of the Schmidt values are zero, then these inverses don't exist. Even if they exist but are small, their inversion will lead to numerical errors. This is problematic for example when evolving from an initial product state under an entangling Hamiltonian. This can be resolved with an inverse-free algorithm, such as that detailed in [64], or alternatively one described in Chapter 3.

3.2.3 Finite matrix product states

For a finite system of N sites we have a slight modification that needs to be made for the end sites, that have just one bond index each. The left-tangent gauge parameterization can be extended as

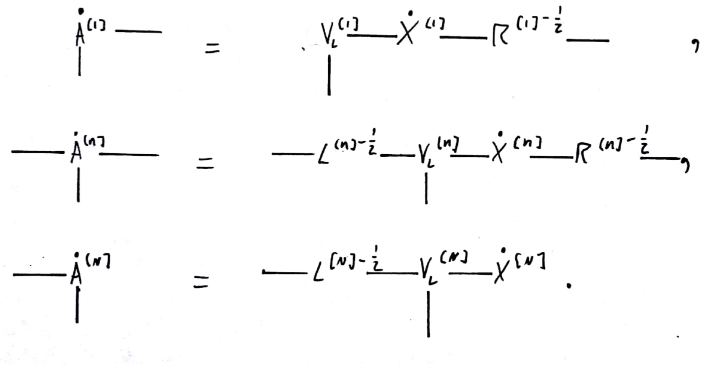

, (2.27)

where here the right and left environments are indicated as R and L. The TDVP equations for $X^{[1]}, X^{[n]}$ and $X^{[N]}$ then read

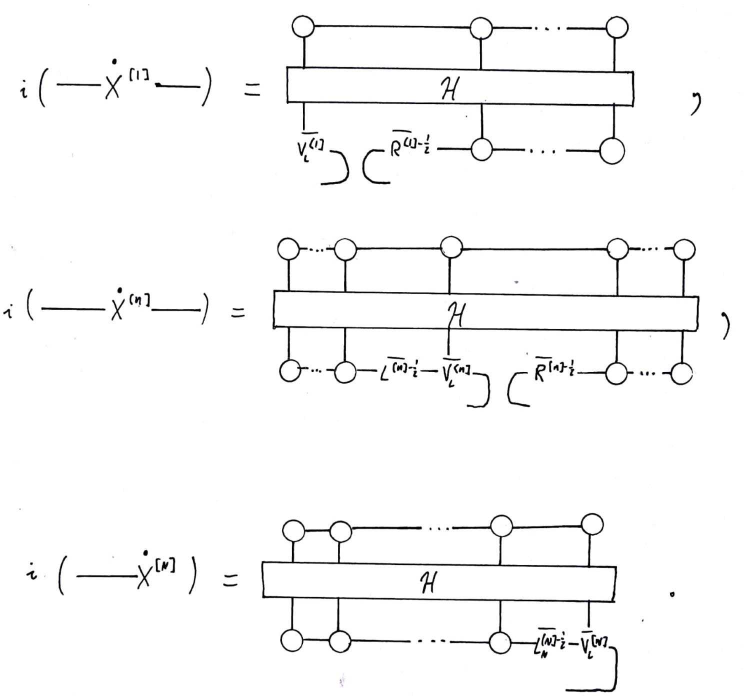

(2.28)

These equations suffer the same problem mentioned above: they require inverting Schmidt coefficients, which may be zero-valued. However this may be resolved by using an algorithm for sweeping along the system, updating each site in turn, also given in [64]. The essential idea is to use central canonical gauge with respect to the site being updates. Consider starting with a state in, say, right-canonical form. This turns out to be the same as the central gauge for the 1st site. The first of the lines in Eq 2.28 can be evaluated without issue, since in this central gauge $R^{[1]} = \mathbb{1}$ is trivially inverted. The first site can then be updated. Then, by acting only on the first two sites, the state can be transformed into the central gauge for the 2nd site, which can then be updated without inverting and Schmidt coefficients. This can be repeated until the Nth site is reached, after which point the updated state will be in the left-canonical form. An analogous sweep from right to left can then be made.

This sweeping update interleaves the update of site tensors and the canonicalization of the states, which is more efficient then separate update and canonicalization steps. In chapters 4, 5 and 6 of this thesis a Langevin open systems model is given for matrix product states, the implementation of which extends this sweeping algorithm to calculating additional noise and friction terms.

3.3 Code validation

As part of the research presented in this thesis, a code library was built from scratch in MATLAB and the ncon function. The ncon function in MATLAB can contract tensor networks, calculating the optimal order to contract indices. More details can be found here [43].

The code library consists of scripts and functions for studying both finite and infinite matrix product states. For both varieties, there are routines for canonicalization, and various analysis functions eg. for calculating expectation values. Implementations of TDVP have been developed for both finite and infinite systems. Additionally an implementation of a Langevin open systems model for finite matrix product states was developed, which is discussed further in Chapter 4.

To validate my implementations of TDVP several approaches were taken. At the most basic level each subroutine was checked for correct behaviour, and unit tests were written to automate this process to an extent. The next step was to test local dynamics, which can be straightforwardly checked with exact diagonalization. Testing non-local dynamics with the infinite-system TDVP (which was written first) required methods beyond exact diagonalization. This was done by calculating the rate function for quenches in cases where exact expressions are known. The rate function here is defined by

$$l(t) = -\log|\langle\psi(0)|\psi(t)\rangle|, \tag{2.29}$$

where t is the time since a quench with the system in the ground state $|\psi(0)\rangle$ of a different Hamiltonian. This is a useful test because it involves a non-trivial evolution through entangled parts of the manifold of matrix product states. In the infinite-system example, the exact expression for the rate function exhibits non-analytic cusps, and reproducing these cusps requires a high level of precision.

Infinite TDVP

For the infinite code I looked at a quench of the spin-1/2 Ising model, for which an analytical expression for the rate function is given in [73]. The Hamiltonian is

$$\hat{H} = -J\sum_i \left(\hat{\sigma}_i^z\hat{\sigma}_{i+1}^z + g\hat{\sigma}_i^x\right), \tag{2.30}$$

and the system is quenches from the ground state at $g = g_0 = 1.5$, in the ferromagnetic phase, to $g = g_1 = 0.2$ in the paramagnetic phase.

The analytical expression for the rate function was compared against numerical results from the infinite-chain TDVP code. The numerical results were obtained

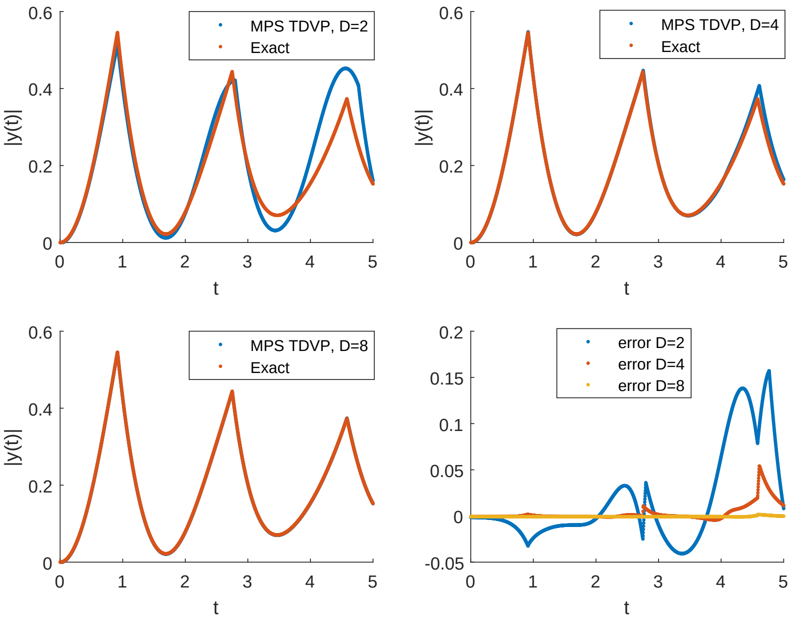

Figure 2.2: *Testing infinite TDVP:* Ising quench with $J = 1$, $g_0 = 1.5$, $g_1 = 0.2$, with analytical and numerical values of the rate function compared for increasing bond dimension $D = 2, 4, 8$. Also shown is a comparison of the absolute error for each bond dimension.

by first evolving a randomized state with $J = 1, g = g_0$ and imaginary timesteps $\Delta t \leftarrow i\Delta t$ for a long time to reach a good approximation to the ground state. Finally this state was evolved in real time with $J = 1, g = g_1$ via the TDVP code to find $|\psi(t)\rangle$ and hence the rate function $l(t)$. The results are shown in Fig 2.2 for bond dimensions $D = 2, 4, 6, 8$. Substantial improvement with bond dimension is seen, and the non-analytical behaviour of the cusps is well reproduced, indicating that the code is working well.

Finite TDVP

For the finite-chain code two rate function checks were carried out. The first is for a simplified XXZ model of spin-1/2s [74]:

$$\hat{\mathcal{H}} = J \sum_j [\hat{S}^x_j \hat{S}^x_{j+1} + \hat{S}^y_j \hat{S}^y_{j+1}] + \sum_j (-1)^j h_{\text{st}} \hat{S}^z_j. \tag{2.31}$$

We start from the ground state when $J = 0, h_{\text{st}} \neq 0$. This is just a Néel state where the spins alternate between aligning parallel and antiparallel to the z direction. The Hamiltonian is then instantaneously changed to $h_{\text{st}} = 0, J \neq 0$. For a number of sites N an integer multiple of 4 an analytical expression for the rate function can be derived, and we test our finite-chain TDVP integrator against this. The results are shown for full bond dimension with $N = 8$ in Fig 2.3 and show good agreement.

The second rate function test for the finite-chain code is for the Ising model, where

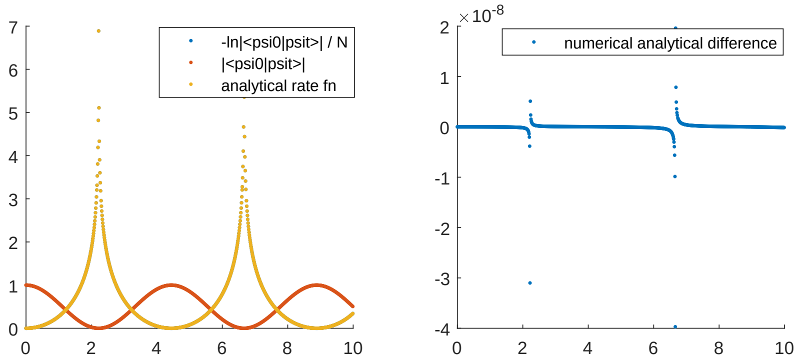

Figure 2.3: *Testing finite TDVP:* Quench of equation (2.31) from $J = 0, h_{\text{st}} \neq 0$ to $J \neq 0, h_{\text{st}} = 0$. Numerical results compare well with analytical expression for rate function.

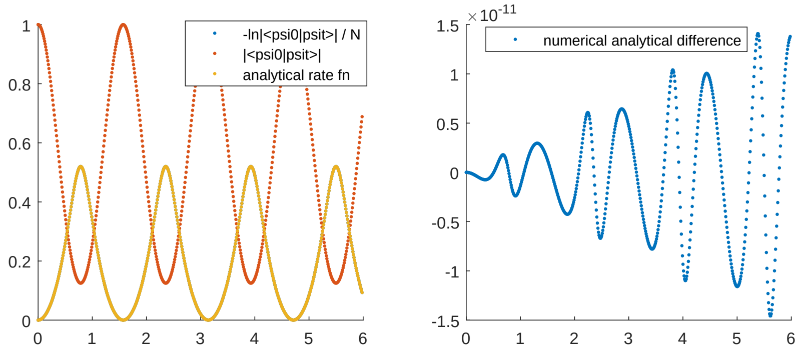

Figure 2.4: *Testing finite TDVP:* Finite chain quench of Ising model (2.30) from $J = 0, g \neq 0$ to $J \neq 0, g = 0$, showing good agreement between analytical expression and numerical values for rate function. Number of sites $N = 8$.

the 1st and Nth sites are also coupled. If N is a multiple of 4 then an exact expression for the rate function is given in [73]. Quenching from $J = 0, g \neq 0$ to $J \neq 0, g = 0$ we get good agreement, as shown in figure Fig 2.4 for $N = 8$.

Chapter 3

Quantum chaos - tracking Lyapunov coefficients

A key difference between classical and quantum mechanics is dynamical chaos. While in classical systems a small difference in initial conditions can lead to exponentially different outcomes, a quantum system undergoes unitary time evolution in which the distance between trajectories stays constant. This chaotic behaviour underpins many phenomena associated with classical systems - it fundamentally limits the work of predicting weather systems, and provides an explanation for thermalization.

In this chapter I report on research into these questions using trajectories of approximate quantum states described by the time-dependent variational principle. Such trajectories are governed by a classical Hamiltonian system of equations, and therefore exhibit classical chaos.

This work is original, and was conducted in collaboration with Andrew G Green and Andrew Hallam, and published here [75]. My contribution to the work was developing time-dependent variational principle code precise enough to generate long-time trajectories, and also involvement in development of code for extracting Lyapunov exponents.

1 Thermalization

Quantum thermalization can be understood in terms of quantum chaos [76], through the study of systems whose classical limit is chaotic, or of many-body systems dominated by single-particle dynamics [77, 78, 79, 80, 81, 82, 83]. For many-body quantum systems where these approximations can't be made, progress can be made by applying random matrix theory to the spectral statistics to reveal the underlying chaos [84, 85, 86, 87, 88, 89, 90]. However this leaves the link between classical and quantum chaos in these many-body systems unclear.

In this section I briefly recap how dynamical chaos leads to thermalization in many-body classical systems, and how this may be measured via Lyapunov coefficients. Then I discuss the study thermalization in many-body quantum systems.

1.1 Dynamical chaos in many-body classical systems

Thermalization is the process by which a system reaches a thermal equilibrium state, characterized only by the system's temperature. This describes processes where a system equilibriates with its environment. It also describes how an isolated many-body system evolves into a dynamical regime where temperature is the only practically useful state variable. Though the microscopic dynamics of classical systems are time-reversible, thermalization leads to an emergent preferred direction or 'arrow' of time via an increased entropy, *i.e.* decreased information content.

This emergence is explained by the tendency of many body classical systems to dynamical chaos. Motion is chaotic when a small difference in initial configurations can grow exponentially. This is illustrated by the famous example of the 'butterfly effect' in complicated weather systems, where in principle the actions of a lone butterfly could determine whether a tornado might form at a later time. However chaos occurs in many simpler classical systems, for example a double pendulum where a second pendulum is hung from the end of the first. Dynamical chaos offers an intuitive explanation for the loss of information content of a system - tracing dynamics backwards in time becomes exponentially more difficult with time. More importantly, it leads to the system exploring all of its possible configurations in a fixed time interval. In this 'ergodic' limit the tools of statistical mechanics can be applied, where only the statistical properties of the possible configurations of the system are important.

Chaos is often studied by looking explicitly at diverging trajectories. The divergence can be quantified in terms of Lyapunov coefficients. For a system with just one degree of freedom $\mathbf{X(t)}$, we can consider the displacement between neighbouring trajectories starting at $\mathbf{X}(0)$ and $\mathbf{X}(0) + d\mathbf{X}(0)$. If at a time t the displacement has become $d\mathbf{X}(t) = Y(\mathbf{X}, t)d\mathbf{X}(0)$, then the corresponding Lyapunov coefficient is defined as[1]

$$\lambda = \lim_{t\to\infty} \frac{1}{t} \log \frac{|d\mathbf{X}(t)|}{|d\mathbf{X}(0)|} = \lim_{t\to\infty} \frac{1}{t} \log |Y(\mathbf{X}, t)d\mathbf{X}(0)|, \tag{3.1}$$

so that expontial divergence of $d\mathbf{X}$ is captured by the growth factor $e^{\lambda t}$. In non-chaotic dynamics, the trajectories may converge ($\lambda < 0$), or stay a fixed distance apart ($\lambda = 0$). Eq 3.1 is also valid for a multi-variable system if $\mathbf{X}$ is a vector and Y a matrix, in which case it will converge on the largest Lyapunov exponent for almost all trajectories $\mathbf{X}(t)$ and tangent vectors $d\mathbf{X}(t)$ [91, 92].

1.2 Eigenstate thermalization in many-body quantum systems

Unlike classical systems, the overall dynamics of quantum many body systems are very much un-chaotic and therefore non-ergodic. Trajectories under the time-dependent Schrödinger equation neither diverge nor converge, in the sense that two states initially with fidelity $|\langle\psi_0|\psi'_0\rangle| = 1 - \epsilon$, will after evolving under a constant Hamiltonian $\hat{H}$ for a time t be separated by the exact same fidelity: $|\langle\psi_t|\psi'_t\rangle| = |\langle\psi_0|e^{+i\hat{H}t}e^{-i\hat{H}t}|\psi'_0\rangle| = 1 - \epsilon$. Moreover any differences in expectation values will scale with ϵ, so that states close in fidelity will stay close in fidelity, and their observables will remain close also[2]. The emergence of thermalization from quantum microscopics must be therefore be different in origin to the classical case.

The eigenstate thermalization hypothesis (ETH) refers to a collection of ideas about the conditions under which quantum systems may exhibit thermalization. These ideas successfully descibe thermalizing behaviour in a large number of many-body quantum models. The general idea is that the expectations values of local observables are, over a long-time average, dominated by terms diagonal in the energy eigenbasis. Moreover that such local expectations ought to vary smoothly with the energy of the state. Therefore the eigenstate expectation values should match up with the thermal Gibbs states at equal energies. The dominance of the diagonal contributions – and the loss of knowledge about the initial state – are thought to occur via dephasing between the local region of the system and its larger complement. A large number of many-body quantum systems appear to behave in a way consistent with ETH[3], and the study and refinement of the conditions and mechanisms of ETH is an

---

[1] Here the $d\mathbf{X}(0)$ in the denominator leads to zero contribution in the infinite time limit. The $d\mathbf{X}(0)$ in the numerator is left in for consistency with the vectorized expression.

[2] This can be seen by defining a basis $\{\psi'_t, \{\psi^{\intercal}_{i,t}\}\}$, having constant overlaps with the initial state $f_t \equiv \langle\psi'_t|\psi_t\rangle$, $f_{i,t} \equiv \langle\psi^{\intercal}_{i,t}|\psi_t\rangle$. Normalization of $|\psi_t\rangle$ requires that $|f_t|^2 + \sum_i |f_{i,t}|^2 = 1 \implies |f_{i,t}|^2 \leq 1 - |f_t|^2 = \epsilon$. Then, writing $|\psi_t\rangle = f_t|\psi'_t\rangle + \sum_i f_{i,t}|\psi'_{i,t}\rangle$, the difference in expectation value of some operator $\hat{O}$ is straightforwardly shown to be $\Delta O_t = \langle\psi_t|\hat{O}|\psi_t\rangle - \langle\psi'_t|\hat{O}|\psi'_t\rangle = -(1 - |f_t|^2)\langle\psi'_t|\hat{O}|\psi'_t\rangle + \sum_i |f_{i,t}|^2\langle\psi^{\intercal}_{i,t}|\hat{O}|\psi^{\intercal}_{i,t}\rangle$, that is, $\Delta O_t \sim \epsilon$.

[3] With some exceptions, for example in many-body localized systems [93, 94, 95].

active area of research.

The research presented in this chapter, and in the associated paper [75], pioneers a new technique for studying thermalization in fundamentally many-body quantum systems. By evolving such a system through a variational manifold via the time-dependent variational principle (TDVP), its thermalization may be related to dynamical chaos. In the following section I discuss this approach, and explain how Lyapunov coefficients for these dynamics can be calculated.

2 Tracking chaos with TDVP

The dynamics of a closed quantum system are unitary, ie. not chaotic. Yet despite this, and despite a lack of any external interactions, many system are known whose local expectations appear to thermalize, converging on the values predicted by statistical mechanics. In this section I show how chaotic trajectories in manifolds of localized matrix product states can be found, moreover how Lyapunov coefficients can be extracted to help explain quantum thermalization in many-body systems.

First I explain how Lyapunov coefficients can be defined and extracted in the geometrically non-trivial manifold of matrix product states. Then I introduce the thermofield purification of the density matrix into a matrix product state, and explain how this can be used to explore states near the centre of the spectrum.

2.1 Projecting quantum dynamics

A link can be made between thermalization in classical and quantum many-body systems by projecting the dynamics of the latter. Using the time-dependent variational principle to find the dynamics of a reduced parameterization of the system leads to effective classical, Hamiltonian equations of motion through the corresponding variational manifold [96, 97]. Thermalization in the quantum system can then be described *via* classical thermalization – that is, it via dynamical chaos [98, 99, 100]. As time progresses, dynamical modes of the system reveal a chaotic nature, at a rate given by the inverse of the corresponding Lyapunov exponent. Thermalization of the system as a whole can be studied by calculating the Lyapunov spectrum.

2.2 Extracting the Lyapunov spectrum

The entire spectrum of Lyapunov coefficients, describing the behaviour of displacements in every dimension, can be found by adapting Eq 3.1. If the space of possible displacements is spanned by d tangent vectors, consider a parallelepiped whose edges are formed by these tangent vectors at point $\mathbf{X}(t)$, $\mathbf{U}(t) = \{d\mathbf{X}^1(t), d\mathbf{X}^2(t), \ldots, d\mathbf{X}^d(t)\}$. The spectrum of the d Lyapunov coefficients can be obtained from the evolution of the volume of this parallelepiped, via

$$\sum_{i=1}^{d} \lambda_i = \lim_{t\to\infty} \frac{1}{t} \log(\mathrm{Vol}^d(Y(\mathbf{X}, t)\mathbf{U}(0))). \tag{3.2}$$

However this alone doesn't provide a practical route to finding the coefficients. Over time the tangent vectors will be biased towards the direction of the largest Lyapunov coefficient, with the effects of the smaller coefficients becoming harder to distinguish. The algorithm of Bennetin et al [99] may be used to overcome this difficulty. This works by separating the rotational and amplitude variations of the tangent vectors, and re-orthogonalizing them at regular intervals. More details are given in Appendix A.

As a first step to deducing the Lyapunov spectrum for MPS, we must assign a distance measure on the variational manifold. This is done using the fidelity between states with two different coordinates $\mathbf{X}$ and $\mathbf{X} + d\mathbf{X}$. In the case of translationally invariant states, we must use the fidelity density rather than fidelity, since the fidelity between translationally invariant states described by an MPS tensor A^{σ}_{ij} and one described by a tensor $A^{\sigma}_{ij} + dA^{\sigma}_{ij}$ scales as one over the total length of the system. As described in Chapter 2, a small deviation from a translationally invariant MPS state described by a tensor A^{σ}_{ij} may be parametrized[96] in terms of freely-chosen complex tensor dX^{σ}_{ij}: $A^{\sigma}_{ij} \rightarrow A^{\sigma}_{ij} + dA^{\sigma}_{ij}$. Suppressing auxiliary indicies for a moment for clarity, we can write $dA^{\sigma} = \sum_{\delta=1}^{d-1} l^{-1/2} V^{\sigma\delta} dX^{\delta} r^{-1/2}$, where l and r are the left and right environments respectively, and $V^{\sigma\delta}_{ij} \equiv V^{\sigma\delta}_{ij}(A)$ is a tensor of null vectors to $A^{\sigma}_{ji}{}^{*}$ (reshaped into a matrix by pairing indices σ and j). This parametrization was a crucial development of Haegeman *et al* in making the TDVP applied to MPS states tractable [96]. The distance measure takes a particularly simple form in terms of X:

$$dS^2 = \sum_{\sigma ij} dX^{\sigma}_{ij}{}^{*} dX^{\sigma}_{ji}. \tag{3.3}$$

This parametrization is useful in determining the Lyapunov spectrum, the details of which we turn to next.

Linearized TDVP and the Lyapunov Spectrum

We are interested in the evolution of the difference of two trajectories, *i.e.* the tangent vectors to the variational manifold. The equation of motion of these is given by linearizing the TDVP equation for matrix product states given in Chapter 2 using the parametrization in terms of $\dot{X}$ given by Eq 2.26. The result of this linearization is given in Box 2.1.

The Lyapunov spectrum is calculated by measuring the extent to which a tangent vector $dX(t)$ has changed in magnitude between a time t and $t+\delta t$. Eq.(3.4) describes how the components dX_a transform but does not account for the transformation of the tangent space basis. This may be captured by allowing for parallel transport along the trajectory. Box 2.2 shows how Eq.(3.4) looks after taking into account the parallel transport.

Box 2.1 Linearized TDVP

Linearizing the time-dependent variational principle gives:

$$\begin{aligned} d\dot{X}_a(t) &= i\langle \partial_{\bar{X}_a}\partial_{\bar{X}_b}\psi|\hat{\mathcal{H}}|\psi\rangle d\bar{X}_b(t) \\ &\quad + i\langle \partial_{\bar{X}_a}\psi|\hat{\mathcal{H}}|\partial_{X_b}\psi\rangle dX_b(t). \end{aligned} \tag{3.4}$$

Our notation indicates a reshaping of the $(d^2-1)D \times D$ matrix dX into a complex $(d^2-1)D^2$ vector. The right hand side of Eq.(3.4) contains two parts: $F_1 = \langle \partial_{\bar{X}_a}\psi|\hat{\mathcal{H}}|\partial_{X_b}\psi\rangle$ is manifestly Hermitian and generates unitary rotations of the tangent vectors. $F_2 = \langle \partial_{\bar{X}_a}\partial_{\bar{X}_b}\psi|\hat{\mathcal{H}}|\psi\rangle$ is not Hermitian. Instead it is a symmetric matrix $F_2 = F_2^T$ and is responsible for the non-unitary evolution of tangent vectors.

Box 2.2 Linearized TDVP with parallel transport

Taking into account parallel transport of the tangent space vectors, the linearized time-dependent variational principle becomes:

$$d\dot{X}(t) = \tilde{F}_1 dX(t) + \tilde{F}_2 d\bar{X}(t), \tag{3.5}$$

where F_1 and F_2 have been modified as follows:

$$F_1 \to \tilde{F}_1 = \langle \partial_{\bar{X}_b}\psi|\hat{\mathcal{H}}|\partial_{X_a}\psi\rangle - \Gamma^c_{ab}\dot{X}_c \tag{3.6}$$

$$F_2 \to \tilde{F}_2 = \langle \partial_{\bar{X}_a}\partial_{\bar{X}_b}\psi|\hat{\mathcal{H}}|\psi\rangle - \bar{\Gamma}^c_{ab}\dot{X}_c, \tag{3.7}$$

with $\bar{\Gamma}_{a,bc} = \langle \partial_{\bar{X}_b}\partial_{\bar{X}_c}\psi|\partial_{X_a}\psi\rangle$ and $\Gamma_{a,bc} = \langle \partial_{\bar{X}_b}\psi|\partial_{X_c}\partial_{X_a}\psi\rangle$ the Christoffel symbols for the variational manifold. With this modification we can calculate the Lyapunov spectrum. We separate the real and imaginary components of $dX = dX^R + idX^I$, $\tilde{F}_1 = \tilde{F}_1^R + i\tilde{F}_1^I$ and $\tilde{F}_2 = \tilde{F}_2^R + i\tilde{F}_2^I$. Eq.(3.4) can be rewritten as:

$$\begin{pmatrix} d\dot{X}^R \\ d\dot{X}^I \end{pmatrix} = \begin{pmatrix} \tilde{F}_1^I + \tilde{F}_2^I & \tilde{F}_1^R - \tilde{F}_2^R \\ -\tilde{F}_1^R - \tilde{F}_2^R & F_1^I - \tilde{F}_2^I \end{pmatrix} \begin{pmatrix} dX^R \\ dX^I \end{pmatrix}. \tag{3.8}$$

When $\tilde{F}_2 = 0$ the Hermitian property of $\tilde{F}_1$ would result in a totally antisymmetric matrix in Eq.(3.8), generating purely orthogonal rotations on the tangent vectors. $\tilde{F}_2$ is responsible for the changing magnitude of a tangent vector upon moving along a trajectory, and therefore for the generation of a non-zero Lyapunov spectrum. Local Hamiltonians $H = \sum_i h_i$ are important examples in which $\tilde{F}_2 = 0$. In this case, the parallel transport term cancels with F_2, guaranteeing that the Lyapunov spectrum is zero for all states. Having accounted for these details, the Lyapunov spectrum of the system can be calculated using Eq.(3.8) and the methods in Appendix A.

2.3 Accurate numerical integration

Extracting the Lyapunov spectrum in the way described here requires numerically evolving matrix product state trajectories accurately for long times. The time-dependent variational principle, where state updates are projected onto the reduced manifold in order to maximize fidelity, was used for this. When a reduced parameterization is used, we get classical Hamiltonian equations, with their own set of conserved quantities - any conserved quantity corresponding to a symmetry that is reflected in the underlying manifold of states is also conserved under the related TDVP equations [71].

Extracting the Lyapunov spectrum in the way described here requires numerically evolving matrix product state trajectories accurately for long times. In order to achieve this the time-dependent variational principle method, discussed in chapter 2, was used. However, in order to achieve the extreme accuracy required for faithfully extracting long-time Lyapounov coefficients, careful development of the code was required.

While the TDVP algorithm is sufficient to determine the time evolution of a matrix product state at fixed bond dimension it has two flaws. Firstly, it necessarily involves inverting Schmidt coefficients and therefore encounters issues when a state has small Schmidt values. Secondly, there is no easy way to increase the bond dimension of the matrix product state as may be necessary if we start from say a product state initial state. Both of these issues can be solved by using an inverse-free version of the TDVP algorithm [64]. In Box 2.3 we provide minor modifications to this algorithm required for real-time evolution rather than imaginary-time evolution as studied in [64]. It is straightforward to check the size of the smallest Schmidt value, and use this to dynamically shift between using this inverse free algorithm (when Schmidt values are small) and an algorithm that is faster but uses inverse Schmidt values.

Additional steps that can be taken to improve the long-time accuracy of the code are to use higher order integrators. Here we used two higher order schemes. The first was a 4th-order Runge Kutta scheme, which has an error that goes as $(\Delta t)^5$ where Δt is the numerical timestep. The second was a reversible midpoint algorithm following [72], which takes advantage of the fact that a numerical integration algorithm that is reversible in time gains an extra power in Δt in its error term, so that a 4th order Runge-Kutta integrator with a reversible timestep has an error that goes as $(\Delta t)^6$.

Box 2.3 Inverse free TDVP

An inverse-free algorithm uses A in both left and right canonical forms, A_L and A_R respectively. For A_L the dominant left eigenvector of the transfer matrix is $l = \mathbb{I}$ and dominant right eigenvector is $r = cc^\dagger$. For A_R the dominant left eigenvector of the transfer matrix is $l = c^\dagger c$ and dominant right eigenvector is $r = \mathbb{I}$. The algorithm has three key steps:

i. A_R and c can be calculated from A_L in an inverse-free method by iterating RQ decompositions

$$c_{(i+1)}A_{R(i+1)} \overset{\mathrm{RQ}}{=} A_{L(i)}c_{(i)} \tag{3.9}$$

until $c_{i+1} \approx c_i$.

ii. An inverse-free update of $A_L(t)$ is found by solving

$$\min_{\tilde{A}_L} |\tilde{A}_L c(t+\delta t) - A_C(t+\delta t)| \tag{3.10}$$

where we have defined $A_C = A_L c = cA_R$, with $A_C(t+\delta t) = A_L(t)c(t) + \delta t\ d(A_L c)/dt$ and $c(t+\delta t) = c(t) + \delta t\ dc/dt$. The time derivative of A_L is obtained *via* the TDVP equations and that of c from

$$(\mathbb{I} - \sum_{\sigma=1}^{d} A_L^\sigma \otimes \bar{A}_R^\sigma)\frac{dc}{dt} = \sum_{\sigma=1}^{d} \frac{dA_L^\sigma}{dt} c A_R^{\sigma\dagger}. \tag{3.11}$$

Eq.(3.11) follows from writing $\frac{dc}{dt} = \frac{d}{dt}(\sum_{\sigma=1}^{d} A_L^\sigma c \bar{A}_R^\sigma)$ and using the right gauge fixing condition on A_R to impose $\sum_{\sigma=1}^{d} A_{ij}^\sigma c_{jk} dA_{R,kl}^{\sigma\dagger} = 0$.

iii. Eq.(3.10) can be solved performing qr decompositions on $c(t+\delta t)$ and $A_C(t+\delta t)_{(\sigma i),j}$, $c(t+\delta t) = qr$ and $A_C(t+\delta t)_{(\sigma i),j} = QR$. We find $r = R$ so $A_L(t+\delta t)_{(\sigma i),j)} = Qq^\dagger$ and $A_L(t+\delta t)_{ij}^\sigma$ can be found by reshaping this matrix.

2.4 The thermofield double

The MPS ansatz applied in the usual way efficiently describes states near to the top and bottom of the spectrum. States near to the centre of the spectrum require an alternative variational parametrization. We use an MPS parametrization of the thermofield double [101], which represents a purification of the density matrix. For a (diagonalized) density matrix $\hat{\rho} = \sum_\alpha \gamma_\alpha |\alpha\rangle\langle\alpha|$, the corresponding purification is written for a doubled system as $|\pmb{\psi}\rangle = \sum_\alpha \sqrt{\gamma_\alpha}|\alpha\rangle \otimes |\alpha\rangle$, so that tracing out one of the subsystems of $|\pmb{\psi}\rangle\langle\pmb{\psi}|$ recovers $\hat{\rho}$. Here γ_α are real positive weights that correspond to the Gibbs weights in thermal equilibrium, and α labels the eigenstates, $|\alpha\rangle$.

Expectation values can be calculated by applying the relevant operator only to the first copy of the system, so that $\langle\pmb{\psi}|\hat{\theta} \otimes \mathbb{1}|\pmb{\psi}\rangle = \mathrm{Tr}(\hat{\theta}\hat{\rho})$. The thermofield double is time-evolved with a Hamiltonian $\pmb{\mathcal{H}} = \mathcal{H} \otimes \mathbf{1} + \mathbf{1} \otimes \mathcal{H}$ which acts symmetrically on the two copies of the system.

The next step is to make MPS parameterizations of the thermofield double. This entails a few differences from when working with MPS representing pure states. If a reduced manifold, *ie* a truncated bond dimension, is used then pure states are taken to mixed states. This means that the bond order of a thermofield MPS no longer yields direct information about the entanglement in the system. Evolving a thermofield MPS via the time-dependent variational principle consists of minimizing fidelity error at each point in time. For a thermofield MPS this fidelity measure is the trace-norm of the true updated density matrix with its MPS approximation. Although TDVP has been applied to the density matrix before [102], as far as we are aware, this is the first time that it has been used to follow real time evolution of a matrix product ansatz for it (though see [103] for a related work).

We parametrize the thermofield double state $|\pmb{\psi}(\pmb{A})\rangle$ by an expanded matrix product state $\pmb{A}^{\sigma\delta}_{IJ}$ with a doubled physical index representing the two copies of the system. The thermofield double state is evolved using the expanded Hamiltonian, $\pmb{\mathcal{H}}$. The time-dependent variational principle, as detailed in Chapter 2, is modified accordingly with $A \to \pmb{A}$, $\mathcal{H} \to \pmb{\mathcal{H}}$ and $\{i, j, \sigma\} \to \{I, J, \sigma, \delta\}$.

In order to obtain accurate results, we have made an important modification to the algorithm developed in [96] for MPS representations of the state. The thermofield double is evidently symmetrical between the two copies of the physical space; observations made on either copy will yield the same result. However, this is not necessarily reflected in an explicit symmetry of the tensor $\pmb{A}^{\sigma\delta}_{I,J}$ and this can lead to the accumulation of numerical errors that break the symmetry. The MPS for the thermofield double can be written such that the symmetry between the two copies of the physical space is explicit. This is achieved for a bond order $\mathbb{D} = D^2$ thermofield MPS by imposing the symmetry $\mathbb{A}^{\sigma\delta}_{I,J} = \mathbb{A}^{\delta\sigma}_{\tilde{I},\tilde{J}}$ using an additional tangent space gauge fixing, where $I \equiv i \otimes i'$ and $\tilde{I} \equiv i' \otimes i$ with the indices $i, i', j, j' \in \{1, 2, ...D\}$[4].

In order to calculate our tangent state we find it more convenient to work in the a slightly different gauge in which the symmetry condition is $\mathbb{A}^{\sigma\delta}_{I,J} = M_{IK}\mathbb{A}^{\delta\sigma}_{KL}M_{LJ}$, where

$$M = \begin{pmatrix} \mathbb{I}_{\frac{D}{2}(D+1)} & 0 \\ 0 & -\mathbb{I}_{\frac{D}{2}(D-1)}, \end{pmatrix} \tag{3.12}$$

The tangent gauge fixing is then achieved as described in Box 2.4.

Box 2.4 Fixing thermofield double tangent gauge

We first calculate $\mathbb{W}^{\sigma\delta}_{L,(IJ)}$ using the methods of Chapter 2. Symmetric $(\frac{1}{2}\mathbb{W}^{\sigma\delta}_{L,(I,J)} + M_{L,L'}\frac{1}{2}\mathbb{W}^{\delta\sigma}_{L',(IJ)})$ and antisymmetric $(\frac{1}{2}\mathbb{W}^{\sigma\delta}_{L,(IJ)} - M_{LL'}\frac{1}{2}\mathbb{W}^{\delta\sigma}_{L',(I,J)})$ parts of $\mathbb{W}$ contribute separately to $d\boldsymbol{A}$ with corresponding symmetric and antisymmetric parts of the matrices X. The symmetrized and anti-symmetrized spaces are each smaller than the doubled space. A complete orthonormal basis for $\mathbb{W}$ is obtained by keeping the first $(d^2-1)D(D+1)/2-D$ or $(d^2-1)D(D-1)/2+D$ (where $\mathbb{D} = D^2$) columns of the Q from a QR decomposition of the symmetrized or anti-symmetrized $\mathbb{W}$ respectively.

This constraint also requires the modification of step iii. in the inverse-free algorithm. $\mathbb{A}_L(t+\delta t)$ is calculated using QR decompositions on $\mathbb{c}(t+\delta t)$ and $\mathbb{A}_C(t+\delta t)$ but the symmetry constraint requires Q to be modified. A new Q is obtained by performing a QR decomposition on the symmetrised $\frac{1}{2}Q_{((\sigma\delta)I),((\sigma\delta)'I')} + \frac{1}{2}MQ_{((\delta\sigma)\tilde{I}),((\delta\sigma)'\tilde{I}')}M^\dagger$ and keeping the first $\mathbb{D}$ columns.

The infinite temperature state takes a particularly simple and instructive form when represented in terms of a thermofield MPS. At $\mathbb{D} = 1$ it is given by $\boldsymbol{A}^{\sigma\delta} = \delta^{\sigma\delta}/\sqrt{2}$. At $\mathbb{D} = D^2 > 1$ there are many ways to represent the state. A class of symmetrical thermofield MPS states can be constructed from a unitary matrix $U \in SU(dD)$ as

$$\boldsymbol{A}^{\sigma\delta}_{IJ} = \frac{1}{\sqrt{d}} \sum_{\gamma=1}^{d} U_{(\sigma i),(\gamma j)} U_{(\delta i'),(\gamma j')}. \tag{3.13}$$

---

[4] Note that a pure state with bond order D wavefunction MPS tensor A^{σ}_{ij} can be represented as a thermofield MPS of bond order $D = \mathbb{D}$ and tensor $\mathbb{A}^{\delta\sigma}_{ii',jj'} = A^{\sigma}_{ij}A^{\delta}_{i'j'}$

This follows from noting that i. the infinite temperature state is the same for any Hamiltonian and ii. that it is invariant under evolution with the Hamiltonian. Eq.(3.13) follows by representing an arbitrary time evolution of $\boldsymbol{A}^{\sigma\delta} = \delta^{\sigma\delta}/\sqrt{2}$ with a bond operator representation of the time-evolution operator using the unitary U. This manifold of equivalent representations of the infinite temperature state resolves an apparent contradiction: on the one hand a state at the middle of the spectrum of a given Hamiltonian is expected to evolve towards the infinite temperature state, whilst on the other hand the projected dynamics is classically Hamiltonian and so cannot evolve to a single point in phase space. It also holds the seed of how to compress the thermofield MPS representation of a thermalizing system at late times[5].

---

[5] A. Hallam and A. G Green work in progress.

3 Results

By simulating the dynamics of a truncated matrix product state description, an associated chaotic classical system can be investigated. In this section are results for an infinite spin chain in integrable, nearly integrable, and non-integrable (thermalizing) limits. The dynamics near the bottom of the spectrum were investigated using wavefunction matrix product states, and the dynamics near the centre were studied using thermofield matrix product states.

We use these tools to study the thermalization of the Ising model with longitudinal and transverse fields:

$$\hat{H} = \sum_i \left[J \hat{\sigma}^{\mathrm{z}}_i \hat{\sigma}^{\mathrm{z}}_{i+1} + h^{\mathrm{x}} \hat{\sigma}^{\mathrm{x}}_i + h^{\mathrm{z}} \hat{\sigma}^{\mathrm{z}}_i \right]. \tag{3.14}$$

The properties of this model are well known; it is integrable when the longitudinal field h^z is zero and non-integrable otherwise. This allows us to investigate: i. integrable systems ($J = O(1)$, $h^{\mathrm{x}} = O(1)$ and $h^{\mathrm{z}} = 0$), ii. non-integrable/thermalizing systems $J = O(1)$, $h^{\mathrm{x}} = O(1)$ and $h^{\mathrm{z}} = O(1)$), and iii. nearly integrable systems $J = O(1)$, $h^{\mathrm{x}} = O(1)$ and $h^{\mathrm{z}} \ll h^{\mathrm{x}}$). We apply the machinery of the time-dependent variational principle to determine trajectories, and the linearized time-dependent variational principle to determine Lyapunov spectra. Reflecting their different encodings of the relevant physics and different regimes of validity, we separate our discussions of the wavefunction MPS and thermofield MPS.

3.1 Wavefunction matrix product state

First we calculate Lyapunov spectra evaluated from the wavefunction MPS starting from an initial product state $\left|\psi(0)\right\rangle_i = (0.382 - 0.382i)\left|\uparrow\right\rangle_i + (-0.595 + 0.595i)\left|\downarrow\right\rangle_i$ near the bottom of the spectrum.

Lyapunov spectrum: The Lyapunov spectrum for the non-integrable, integrable and nearly-integrable cases are shown in Fig. 3.1. All show a broad distribution of exponents, with no strong differences apparent between integrable and non-integrable cases. Although there is a difference between the non-integrable and integrable or nearly-integrable cases, this is insufficient to provide a diagnostic of integrability.

A translationally invariant MPS is parametrized by a set of $D \times D$ matrices, where D is the bond order. Since the nonlinearities and chaos of our dynamics arise from projection to the variational manifold, the Lyapunov spectrum varies with bond order. This situation is unlike the conventional use of matrix product methods, where increasing bond order gives increasingly accurate results. The dependence of the

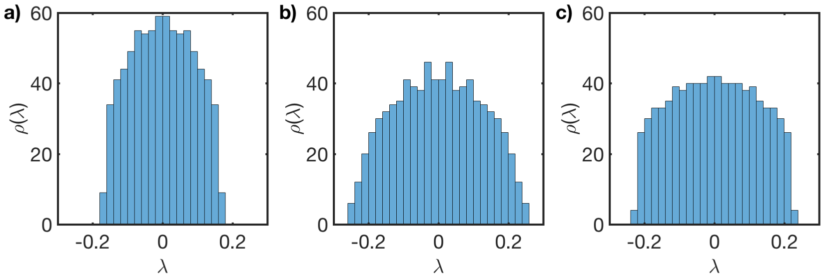

Figure 3.1: *Lyapunov Spectrum for a wavefunction MPS representation of Ising model dynamics*: a) Non-integrable case with $J = 1$, $h^x = 0.5$, $h^z = 1$. b) Integrable case with $J = 1$, $h^x = 0.5$, $h^z = 0$. c) Nearly Integrable case with $J = 1$, $h^x = 0.5$, $h^z = 0.1$ In all cases the spectrum is obtained for an MPS representation of the wavefunction at bond order $D = 20$.

maximum Lyapunov exponent, $\lambda_{\max}$, upon D is shown in Fig 3.2. This shows a decrease from $D = 2$ as $D \to \infty$. The following discussion demonstrates the consistency of these results with physical observations. Note that in the translationally invariant case with spin 1/2, the projected dynamics is not chaotic at $D = 1$ by the Poincaré-Bendixson theorem, since the phase space is two-dimensional. The Lyapunov exponents are therefore zero in this case.

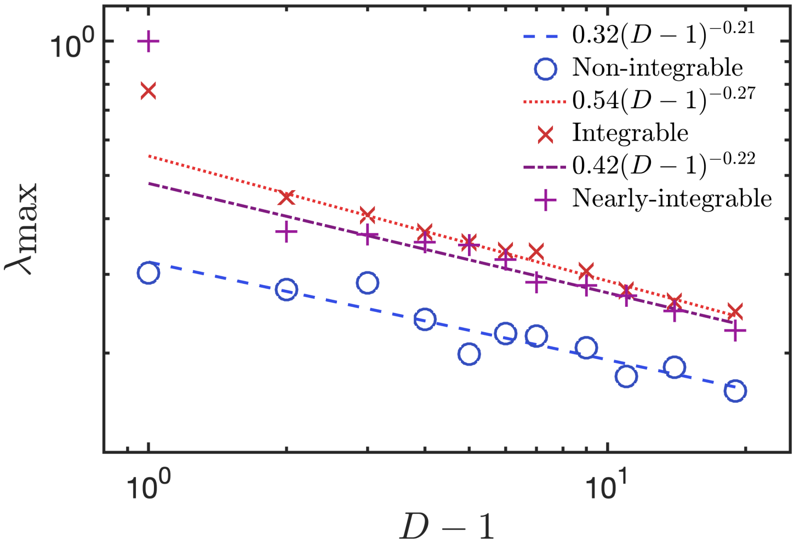

Figure 3.2: *Maximum Lyapunov exponent versus bond order:* The maximum Lyapunov exponent depends strongly upon the projection non-linearities at different bond orders, tending to zero in the limit $D \to \infty$. Here we show the largest exponent varying with bond order for Non-Integrable (circles), Integrable (crosses) and Nearly integrable (pluses) systems. The largest exponent decreases like $\lambda_{\max}(D) = 0.32(D-1)^{-0.21}$ for Non-Integrable systems, $\lambda_{\max}(D) = 0.54(D-1)^{-0.27}$ for Integrable systems and $\lambda_{\max}(D) = 0.42(D-1)^{-0.22}$ for Nearly-Integrable systems.

Maldacena et al.[104] have conjectured that the largest Lyapunov exponent of a quantum system has an upper bound related to its temperature $\lambda_{\max} \leq 2\pi k_B T/\hbar$. The behaviour of $\lambda_{\max}$ for initial states of different energy can be seen in Fig 3.3. At low energies the exponent appears to increase as a power law before saturating at

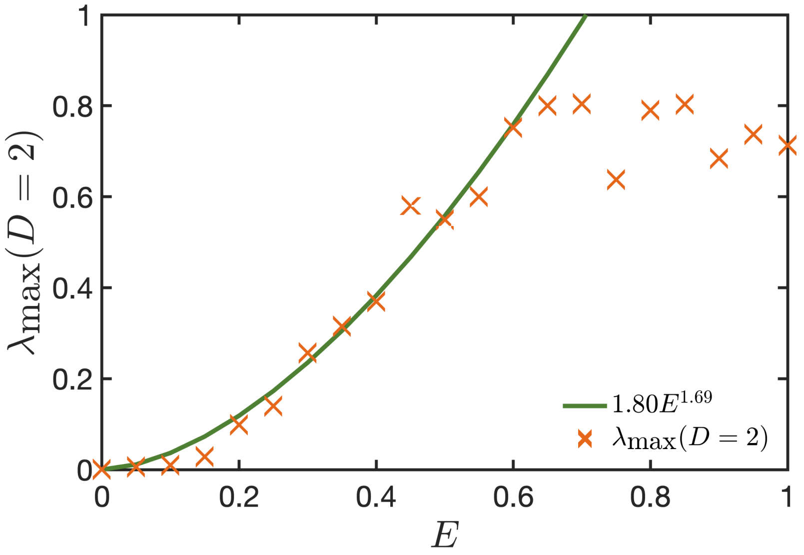

Figure 3.3: *Maximum Lyapunov exponent versus energy density:* It has previously been conjectured that $\lambda_{\max} \leq 2\pi k_{\mathrm{B}} T/\hbar$, here we observe that $\lambda_{\max}(D=2)$ increases with energy density above the ground state but appears to saturated at $E \approx 0.6$. The initial growth of $\lambda_{\max}$ was fitted with a power law $1.80E^{1.69}$.

$E \approx 0.6$.

Entropy growth: The dependence of the entanglement entropy S_{E} upon time is shown in Figs. 3.4 and 3.5. S_{E} grows until saturation at a point that increases with bond order. This saturation point can be well approximated by drawing the Schmidt coefficients s_n from a distribution given by the modulus of the elements of a random $O(D)$ vector. The mean Schmidt coefficients then correspond to $s_n = n\sqrt{6}/\sqrt{D(1+D)(1+2D)}$, from which one may deduce a saturation entanglement at large bond order given by

$$S_{\mathrm{E}}^{\mathrm{Sat}}(D) = -\sum_{n=1}^{D} s_n^2 \log s_n^2 \approx \log[0.65(D-1)+1]. \tag{3.15}$$

With growing entanglement, the effective bond order of the quantum state (the bond order required for an accurate description) grows. We can use Eq.(3.15) to deduce this time-dependence; at the point where S_E crosses the bond order D saturation value, the bond order must be increased. A continuous approximation can be found by equating $S_{\mathrm{E}}^{\mathrm{Sat}}(D-1) = S_{\mathrm{E}}(t)$, from which we obtain

$$D(t) = 1.54(e^{S_E(t)} - 0.997) + 2. \tag{3.16}$$

As we discuss presently, this dependence of bond order upon time allow us to demonstrate the consistency of the Lyapunov spectrum and its variation with D with the physically relevant dependence of the entanglement entropy upon time.

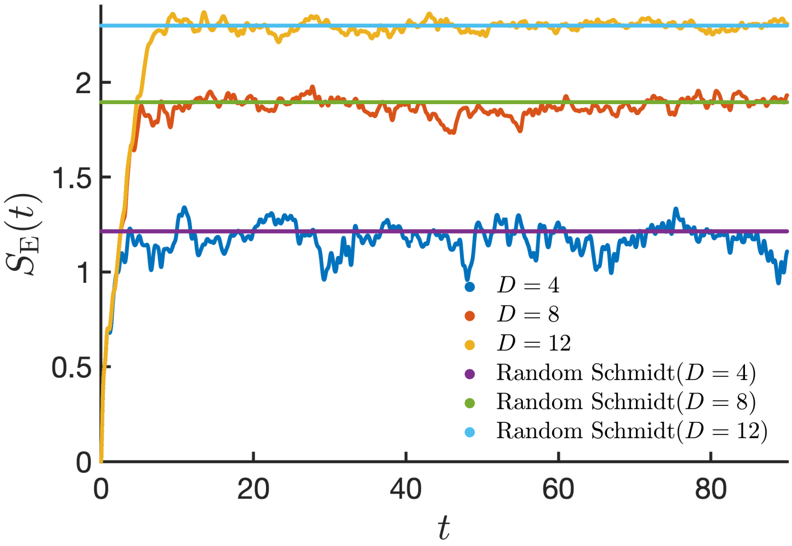

Figure 3.4: *Entanglement entropy across a bond compared to randomly distributed Schmidt coefficients:* At a given bond dimension the entanglement entropy will saturate after a short time. The saturation value for the entanglement entropy is in strong agreement with a random uniform distribution of Schmidt coefficients.

The Kolmogorov-Sinai entropy S_{KS} is a measure of how quickly knowledge of a system's initial state is lost in a chaotic system. It determines the growth-rate of the volume of a region of phase space and, following Pesin's theorem [105], is given by the sum of the positive Lyapunov exponents. The Kolmogorov-Sinai entropy is therefore straightforwardly calculated from our results.

Studies of single particle quantum chaos have shown the relationship $\dot{S}_{\mathrm{E}}(t=0) = S_{\mathrm{KS}}$, provided that starting wavefunction is as classical as possible [106, 107, 108]. Here we find — as indicated in Fig. 3.5 — that $\dot{S}_{\mathrm{E}}(t=0) = S_{\mathrm{KS}}(D=2)$. $D = 2$ corresponds to the most classical, non-trivial (recall that $D = 1$ has vanishing Lyapunov exponents) projected dynamics and is the many-body equivalent of the single particle result. We speculate the following extension of this result:

$$\dot{S}_{\mathrm{E}}(t) = \frac{S_{\mathrm{KS}}(D(t))}{(D(t)-1)^2}. \tag{3.17}$$

Our main justification is the very good, zero-parameter fit that it gives between our results for the entanglement and Lyapunov spectrum. A derivation may be possible from the entangled path integral [65], where a similar result is obtained for the growth rate of bosonic fluctuations at a particular bond order. Fig. 3.6 shows the Kolmogorov-Sinai entropy scaled by $(D-1)^2$ and its dependence upon bond order.

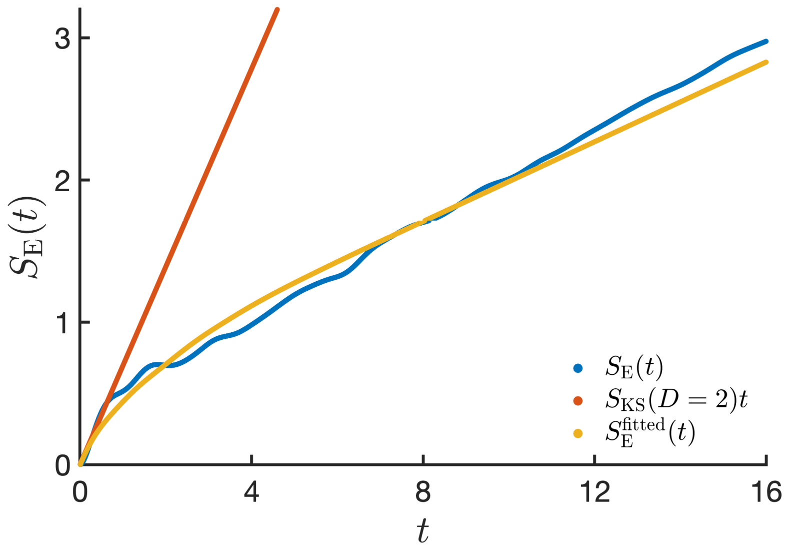

Figure 3.5: *Entanglement entropy and Kolmogorov-Sinai entropy:* The gradient of the entanglement entropy is determined by the Kolmogorov-Sinai entropy. The Kolmogorov-Sinai entropy at $D = 2$ accurately predicts the gradient of the entanglement entropy at $t = 0$ (orange). Substituting fitted forms for the Lyapunov spectrum and saturation entanglement into Eq.(3.17) gives a zero parameter fit to the entanglement entropy (yellow). This fits may both be compared with the time evolution of $S_E(t)$ found using iTEBD at $D = 100$.

At long times we expect $S_{\mathrm{E}}(t) \sim t$ for thermalising systems, which using Eq.(3.17) suggests the fit

$$\frac{S_{\mathrm{KS}}(D)}{(D-1)^2} = 0.14 + 1.6e^{-1.08(D-1)}. \tag{3.18}$$

Combining Eqs.(3.16), (3.17) and (3.18) the Lyapunov data imply a differential equation for $S_{\mathrm{E}}(t)$ that we can integrate to find $S_{\mathrm{E}}(t)$. Fig. 3.5 shows the result plotted alongside entanglement obtained from a high bond-order iTEBD algorithm. The Lyapunov spectra underestimate the late-time linear growth rate of entanglement by about 15%. Note that Fig. 3.5 is plotted to times that extrapolate beyond times where our TDVP simulations are accurate.

It is apparent from these observations that the Lyapunov spectrum extracted from mapping the quantum dynamics of the wavefunction to classical Hamiltonian dynamics is not unique. There is no sense in which spectra collected in this way show numerical convergence, with increasing bond order. A moments reflection about the way in which the wavefunction MPS captures the physics of thermalization shows why. At low bond order, the dynamics is very non-linear and thermalization occurs via chaotic classical dynamics. Thermal averages are recovered in temporal averages of the simulated dynamics. As bond order increases, the MPS ansatz make better and better approximation to the underlying eigenstates and ultimately, thermalization is captured in the same way as the conventional picture of eigenstate thermalization.

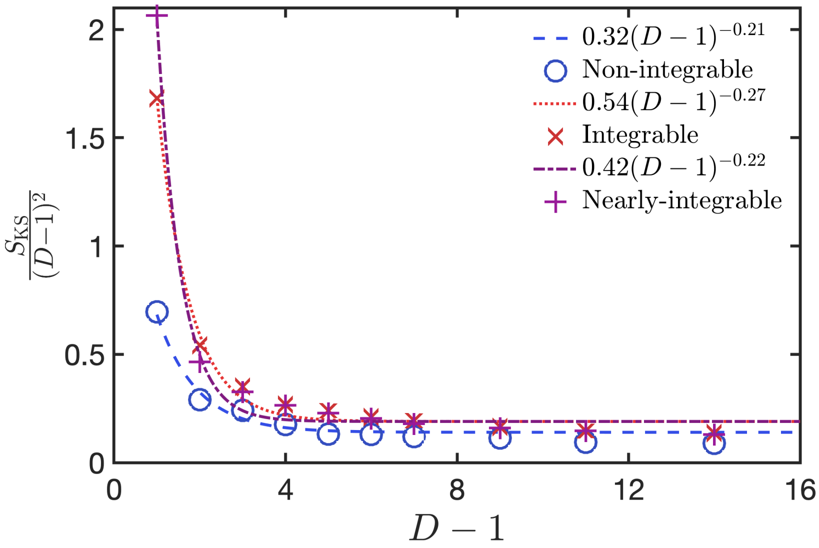

Figure 3.6: *Kolmogorov-Sinai entropy versus bond order:* The Kolmogorov-Sinai entropy scaled by $(D-1)^2$ is related to entanglement growth at short times. Here we show the scaled KS entropy varying with bond order for Non-Integrable (circles), Integrable (crosses) and Nearly integrable (pluses) systems. The Non-Integrable KS entropy decreases like $0.14 + 1.6e^{-1.08(D-1)}$, the Integrable KS entropy decreases like $0.19 + 6.6e^{-1.32(D-1)}$ and the Nearly-Integrable KS entropy decreases like $0.19 + 11.4e^{-1.81(D-1)}$.

Thermal averages are obtained in instantaneous measurements after an initial period of dephasing reveals the intrinsic properties of the underlying eigenstates. However, the Lyapunov spectrum does have physical meaning. We have demonstrated how the physical quantity, $S_{\mathrm{E}}(t)$, is related to the Lyapunov spectrum obtained on a sequence of variational manifolds.

3.2 Thermofield matrix product state

While MPS approximations of pure states allowed us to relate thermalization to chaotic projected dynamics near the edge of the spectrum, the practical limitations of working with large bond dimension mean it can't be applied near the middle. Here we use MPS approximations of the thermofield double to calculate the Lyapunov spectrum near the middle of the spectrum. We consider an initial pure state near to the middle of spectrum, $|\psi(0)\rangle_i = 0.448\,|\uparrow\rangle_i + 0.873\,|\downarrow\rangle_i$. The late time dynamics of this are similar to the infinite-temperature state, which is well captured by the thermofield double.

The Lyapunov spectra for the thermofield MPS dynamics are shown in Fig. 3.7. There is now a clear distinction between the non-integrable, and integrable and nearly-integrable cases. The former has a semi-circular distribution, whereas the latter are narrower and fit a Gaussian distribution (with long tails that have been cut off in Fig. 3.7). For long time averages, the Lyapunov spectrum for the nearly integrable case is expected to crossover from a pre-thermalization Gaussian to a semi-circle distribution. There is a narrowing of the tails of our spectra at late times, but a clear demonstration of the emergence of a semi-circle is a subject for further study. The semi-circular distribution in the non-integrable case suggests a connection to random matrix theory. Such a connection has previously been explored in the context of matrix models [109, 110].

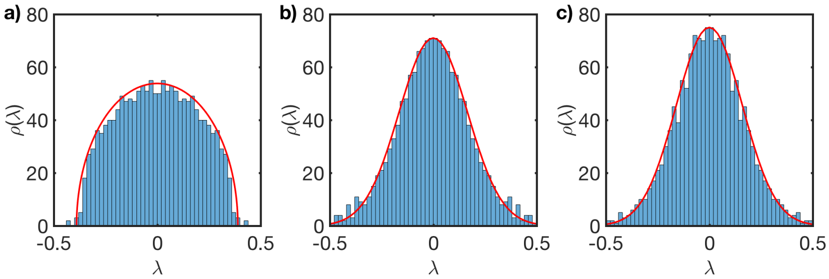

Figure 3.7: *Lyapunov Spectrum for a thermofield MPS representation of Ising model dynamics*: a) Non-integrable case with $J = 1$, $h^x = 0.5$, $h^z = 1$. b) Integrable case with $J = 1$, $h^x = 0.5$, $h^z = 0$. c) Nearly Integrable case with $J = 1$, $h^x = 0.5$, $h^z = 0.1$ In all cases the spectrum is obtained for a wavefunction MPS at bond order $\mathbb{D} = 16$. The non-Integrable case appears to fit a semicircle distribution with radius $r = 0.39$, the Integrable case appears to be Gaussian with standard deviation $\sigma = 0.167$ and the nearly integrable case appears to be Gaussian with standard deviation $\sigma = 0.161$.

Fig. 3.8 shows the variation of the maximum Lyapunov exponent with bond order for the non-integrable case. Symmetry constraints that we impose upon the thermofield MPS tensor, as discussed earlier in this Chapter, restrict the bond order to $\mathbb{D} = 1, 4, 9, 16$ *etc*, and together with the rapid growth of the number of Lyapunov exponents as $2(d^2 - 1)\mathbb{D}^2$ this leads to rather few points in the figure. Note that since the dimension of the local Hilbert space is d^2, dynamical chaos occurs at $\mathbb{D} = 1$. Our numerics are fit by $1.09\mathbb{D}^{-0.373}$, or $1.17e^{-0.0173\mathbb{D}}$, but are also consistent with convergence $0.410 + 0.1740e^{-0.0116\mathbb{D}}$. The latter might be expected since the thermofield double (being a purification of the density matrix) encodes a limited set of observations corresponding roughly to a window of size $\frac{1}{2}\log_2 \mathbb{D}$. When this window is larger than the correlation length timescales of the dynamics are expected to converge to values characteristic of the observable thermalization process.

The Kolmogorov Sinai entropy for the thermofield MPS is shown in Fig. 3.9. This is fit with $1.427\mathbb{D}^{1.58}$ to high accuracy. This scaling is less than $\mathbb{D}^2$ (the volume of phase space) of a typical classical dynamical system. This is consistent with unitary dynamics as $\mathbb{D}$ tends to infinity. Unlike wavefunction MPS, we have been unable to find a simple relationship between the Kolmogorov-Sinai entropy and thermofield entanglement.

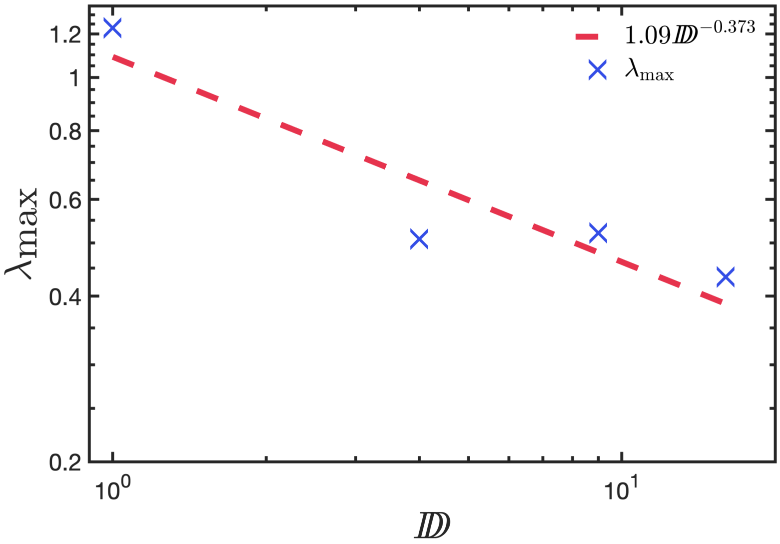

Figure 3.8: *Maximum Lyapunov Exponent vs Thermofield MPS Bond Order for Non-Integrable System:* The largest Lyapunov exponent for the Ising model with $J = 1$, $h^x = 0.5$, $h^z = 1.0$ obtained for an MPS representation of the Thermofield double. The exponent appears to be approaching zero like $\lambda_{\max} = 1.09\mathbb{D}^{-0.373}$

4 Discussion

This chapter has presented a new collection of techniques for studying thermalization in strongly coupled, many-body, quantum systems, where no easy simplifications are available. By casting the quantum dynamics of the system to MPS approximations – either of pure states near the edge, or density matrices near the middle of the spectrum – chaotic classical trajectories emerge via the time-dependent variational principle. This provides an explicit realization of the conventional picture of dephasing of eigenstates, as seen in eigenstate thermalization, and brings the study of quantum chaos full circle. Previous studies of quantum chaos have focussed on single-particle quantum systems with a chaotic semi-classical limit, or else on regimes where many-body quantum dynamics are dominated by single-particle behaviour [77, 78, 79, 80, 81, 82, 83]. Following this approach the level statistics of the system can be used as a diagnostic of chaotic behaviour, giving insights that can be extended to genuinely many-body dynamics [84, 85, 87, 88]. The techniques presented here instead allow genuinely many-body systems to be studied in a semi-classical context via MPS descriptions.

One outcome of this research is evidence of a new relationship between the Komogorov-Sinai entropy, MPS bond order, and entanglement (Eq 3.17). Here entropy is related to the growth of bond dimension $D(t)$ and the related Komogorov-Sinai entropy $S_{\text{KS}}(D(t))$. Another outcome is the striking Gaussian and semi-circular distribution of Lyapunov coefficients seen for the thermofield MPS in integrable and non-integrable systems respectively. The circular distribution for non-integrable systems has been

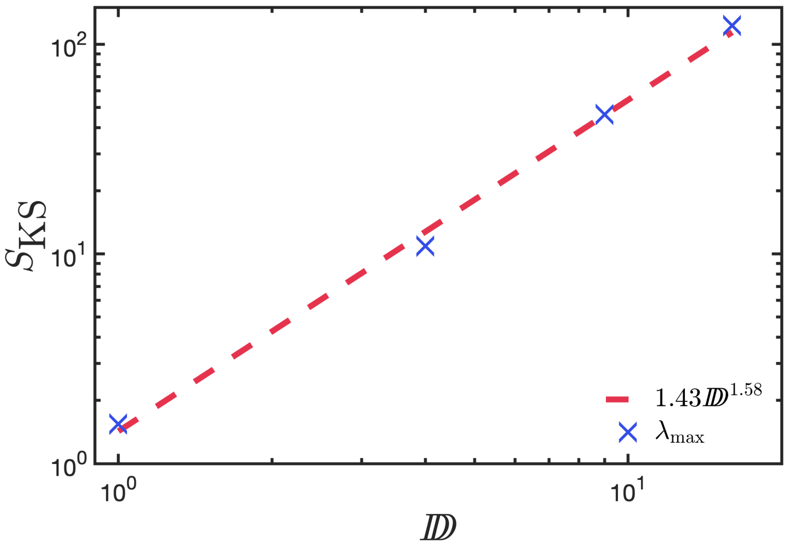

Figure 3.9: *Kolmogorov-Sinai entropy vs Thermofield MPS Bond Order for Non-Integrable System:* The Kolmogorov-Sinai entropy for the Ising model with $J = 1$, $h^{\mathrm{x}} = 0.5$, $h^{\mathrm{z}} = 1.0$ obtained for an MPS representation of the Thermofield double. The KS entropy appears to be diverging, growing like $S_{\mathrm{KS}} = 1.4270\mathbb{D}^{1.58}$.

predicted in studies of gravitation [109, 110] and conjectured to be universal.

A natural extension of this work is to adapt the method to finite systems, where for example comparisons could be made with previous calculations of out-of-time ordered correlators [111, 112, 113, 114, 115]. These results suggest a route to numerical studies of quantum systems that sidestep the usual barrier of exponential memory requirements. Dynamical modes that have revealed themselves to be chaotic act as a chaotic bath for the remaining quasi-regular modes. If these were modelled as such, via a Langevin description, the memory requirement could be substantially reduced, and the short- and long-time dynamics captured as dissipative and diffusive effects respectively. Methods for formulating and applying a Langevin equation over matrix product states are given in Chapter 4 and 5. Another interesting extension to this work would be to look for quantum analogues of behaviour described by the KAM theorem for classical systems. The KAM theorem codifies the robustness of classical integrable systems to perturbations, and its applicability in quantum systems has been speculated on [116]. Projecting quantum dynamics to the classical dynamics of a reduced MPS description suggests a promising route to investigating the robustness of quantum integrability.

Chapter 4

A Langevin equation for matrix product states

A key challenge in developing quantum technologies is understanding how a quantum system is affected by its environment. This can be modelled with a quantum Langevin equation, which adds the effects of noise and dissipation to the Schrödinger equation. However these techniques are generally either limited to describing non-entangled states, or burdened with carrying along a full description of an arbitrary (entangled) quantum state. This chapter presents a quantum Langevin equation over matrix product states, which combines the power of a quantum Langevin equation with an efficient matrix product state parameterization of partially entangled states.

First I present a general survey of techniques for studying open systems, with a focus on how Langevin techniques have been applied to many-body quantum systems. Next I show how a quantum Langevin equation for matrix product states can be derived and illustrate its properties with an exactly soluble model for two spins. Finally I discuss the practicalities of implementation, and the algorithms developed for this purpose as part of this research. The following chapters will use these techniques.

The original work in this chapter consists of the techniques for implementing the quantum Langevin equation for matrix product states for arbitrary matrix product states, and writing the associated code. [article in preparation]

1 Langevin methods for open quantum systems

The Langevin equation for the dynamics of a classical particle accounts for the particle's surroundings with two effects: i. a stochastic forcing, and ii. a deterministic friction, accounting for the viscosity of the surroundings with a drag term proportional to the speed of the particle.

A similar Langevin equation can also be formed for a quantum particle by adding noise and friction terms to the Schrödinger equation for single particle quantum mechanics. While this allows a fairly direct translation of some of the classical techniques, a single-particle Langevin equation can't account for quantum entanglement.

This can be resolved by deriving a stochastic Schrödinger equation for the full wavefunction of a many-body quantum system, as described in [117]. However this approach quickly runs into the usual difficulties of working with many-body wavefunctions: the exponential amount of information required to store the state.

The methods introduced in this chapter allow a Langevin modelling of entangled many-body quantum systems via a Langevin equation over matrix product states. The purpose of this section is to illustrate how this development sits in the current literature. First I give an overview of classical Langevin equations, illustrating the key features that carry over to their quantum counterparts. Then follows a summary discussion of the open quantum systems toolkit, including the key difficulties and common steps made to overcome these. Finally I discuss Langevin equations for many-body quantum systems.

1.1 Classical Langevin equations

Langevin equations were first developed by Paul Langevin to explain Brownian motion, where a visible particle moves according to interactions with an invisible fluid [42]. The most famous example of Brownian motion is the perplexing movements of a pollen particle suspended in water [41]. Einstein explained this motion in 1905 in terms of collisions between the pollen particle and the water molecules, by deriving equations of motion for the probability density of the pollen particle, in a precursor to Fokker-Planck equations. Langevin published his complementary approach in 1908 that modified Newton's second law with noisy and friction terms. Langevin's approach was more intuitive, dealing with stochastic trajectories of Brownian particles, though this came with the price of requiring the sophistications of dealing with stochastic differential equations.

By way of illustration, Box 1.1 gives an example of a classical Langevin approach to modelling a harmonic oscillator. Langevin equations give stochastic trajectories, whose properties can be used to calculate the effects of diffusion.

Box 1.1 Classical Langevin Harmonic Oscillator

An example of a classical Langevin model is a harmonic oscillator in thermal contact with an environment, as studied in [118]. The oscillator is modelled with a modified version of Newton's equation $F = m\ddot{x} = -kx$:

$$m\ddot{x} = -kx - \gamma\dot{x} + \sqrt{2k_B\gamma T}\eta(t).$$

The environment is modelled with a damping term tuned by γ proportional to the velocity $\dot{x}$ and a noise term proportional to a δ-correlated Gaussian white noise $\eta(t)$ obeying

$$\langle\eta(t)\rangle = 0, \quad \langle\eta(t)\eta(t')\rangle = 2k_B\gamma T\delta(t-t').$$

This model can be solved, giving a stochastic solution in terms of a noise sequence $\eta(t)$. The resulting trajectory $x(t)$ can be interpreted as a possible motion of the oscillator, and expectations such as the mean $\langle x(t)\rangle$ and variance σ_x^2 can be computed. In this case, $\langle x(t)\rangle = 0$ and $\sigma_x^2 \propto T$. The noise term balances the energy of the system at long times, resulting in $\frac{1}{2}m\langle v^2(t)\rangle = k_BT$, in agreement with the equipartition theorem.

Fluctuation Dissipation Relations: The fluctuation dissipation relation describes the balance between thermal fluctuations and friction[119, 120]. It is an important result that explains the form of the noise term in Box 1.1. Here the noise is δ-correlated in time with zero mean and variance equal to $2k_B\gamma T$, where k_B is Boltzmann's constant. This variance codifies the relation between the strength of the friction γ, the temperature of the bath T, and the size of the noise fluctuations.

The insight of fluctuation dissipation relations is that for systems in thermal contact, every dissipative process has an associated fluctuation. Dissipative processes generate heat, which in turn induces fluctuations. When detailed balance conditions are satisfied, the relationship between these paired dissipative and fluctuating processes can be quantified. In the case give above, of thermal coupling to a bath in the Markovian limit, the fluctuations of the noise are related to the dissipative friction of strength γ by the following relation

$$\langle \eta(t)\eta(t')\rangle = 2k_B\gamma T\delta(t-t'). \tag{4.1}$$

The fluctuation dissipation theorem is a powerful result and occurs in many contexts. As well as Brownian motion discussed above, other example include Jonhson-Nyquist noise in electrical resistors, where the dissipative slowing of current generates heat which in turn causes current fluctuations [121, 122]. Another example is Kirchoff's law for thermal radiation, where the dissipative process is absorption of radiation, which is associated with a fluctuating emission of radiation [123].

1.2 The open quantum systems toolkit

A quantum system is considered to be 'open' if its interactions with its surroundings are important. There are a variety of useful techniques for studying open quantum systems. Sometimes exact solutions are possible, but more often some degree of approximation is made for the environment, resulting in a plethora of models for open quantum systems [124, 125]. Typically approximations of the environment result in a probabilistic element to the system's dynamics. One approach is to use a density matrix description, leading to master equations that describe the evolution of probability distributions over the system state, in analogy with Einstein's approach to studying Brownian motion. Another is to use stochastic trajectories of pure quantum systems, which on averaging over noise reproduce the results of master equations, similar to Langevin's approach. The relative merits of the two approaches are similar to the classical case: while density matrix methods give useful results about noise-averaged quantities, they can be more difficult to compute. Additionally density matrices suffer from a freedom of decomposition - many different ensembles of pure state can produce the same density matrix - that can make an interpretation in terms of individual processes difficult. On the other hand, trajectories are faster to compute and easier to interpret, but give a less complete account of averaged behaviour.

Here I give a general survey of techniques used to model open quantum systems, expanding on density matrix and trajectory-based methods in more detail. I then introduce the Caldeira-Leggett model for the system-environment interaction, which is used later in the chapter.

1.2.1 General survey

The Hamiltonian of a system and its environment (or bath) is often written as

$$\hat{H} = \hat{H}_{\mathrm{S}} + \hat{H}_{\mathrm{B}} + \hat{H}_{\mathrm{I}}, \tag{4.2}$$

where the terms affecting just the bath or just the environment are separated into $\hat{H}_{\mathrm{B}}$ and $\hat{H}_{\mathrm{B}}$ respectively, and terms involving degrees of freedom from both are included in the interaction Hamiltonian $\hat{H}_{\mathrm{I}}$. The joint system-bath state at a time t is given by $|\Psi_{\mathrm{SB}}(t)\rangle = \exp(-i\int_t \hat{H}dt)|\Psi_{\mathrm{SB}}(0)\rangle = \hat{U}(t,0)|\Psi_{\mathrm{SB}}(0)\rangle$.

Two common assumptions made are i. that the initial state is separable between the system and environment, ie $|\Psi_{\mathrm{SB}}(0)\rangle = |\psi_{\mathrm{S}}(0)\rangle \otimes |\psi_{\mathrm{B}}(0)\rangle$, and ii. that the interaction is Markovian. Markovianity means that the interaction at a given time is independent of the state at previous times, ie. the bath is ‘memoryless’. This is true when the timescale of environmental relaxation after an interaction is much faster than the timescale of the system dynamics.

Master equations

Master equations describe the evolution of the system density matrix, related to the joint system-bath state by

$$\hat{\rho}_{\mathrm{S}}(t) = \mathrm{Tr}_{\mathrm{E}}\left[|\Psi_{\mathrm{SB}}(t)\rangle\langle\Psi_{\mathrm{SB}}(t)|\right]. \tag{4.3}$$

Deterministic equations of motion for $\hat{\rho}_{\mathrm{S}}(t)$ can be derived through a variety of methods. One starting point is to take the trace over the environment of the Liouville-von Neumann equation to write

$$\frac{d\hat{\rho}_{\mathrm{S}}}{dt} = \mathrm{Tr}_{\mathrm{E}}\left[\frac{d\hat{\rho}}{dt}\right] = -i\mathrm{Tr}_{\mathrm{E}}\left\{[\hat{H}, \rho]\right\}, \tag{4.4}$$

where $\hat{\rho}$ is the joint system-bath density matrix. With the help of an initially separable state and assumptions of Markovianity, it is possible to derive a RHS to this equation in terms of just the system density operator $\hat{\rho}_{\mathrm{S}}$. The effects of the environment are accounted for by a collection of super-operators that act on $\hat{\rho}_{\mathrm{S}}$, often called Lindblad or Kraus operators.

Master equations give deterministic equations of motion for $\hat{\rho}_{\mathrm{S}}$, and while this does give an account of the measurement statistics, they do not describe any particular history of the system: the underlying probability distribution's essential properties are conserved, but the unitarity of the evolution of individual state vectors is lost. This makes 'unravelling' a density matrix an ambiguous task, in particular it is very difficult to extract meaningful entanglement measures from a density matrix [126, 30].

Trajectory-based methods

As mentioned above, there are various ways to 'unravel' a the ensemble of pure-state quantum trajectories summarized by the system density matrix. Trajectory-based open systems methods find stochastic equations of such trajectories. Techniques of this variety include *stochastic Schrödinger equations*, where noisy terms are added to the usual time- dependent Schrödinger equation [127, 128, 129], and Monte-Carlo methods, where a change in the system, for example a photon detection event, is described by a Poisson process [130, 131]. Trajectory based methods can sometimes be interpreted as a single run of an experiment that produces differing outcomes each time it is performed. Only having to evolve one state vector gives square-root saving in the number of degrees of freedom to be considered in master equations, and can allow a description of dynamics that are conditional upon measurement [132].

The subject of the latter sections of this chapter is a quantum Langevin equation, a trajectory-based open quantum system model. Quantum Langevin methods give a good account of the thermal properties of the system-bath interaction, accounting for both the temperature of the bath and strength of its coupling to the system via the fluctuation-dissipation theorem. These effects are separate terms in a Langevin equation, allowing each effect to be studied independently, and the size of each effect to be varied. The derivation of this equation starts with a model of the system-bath interaction, ie an appropriate choice of $\hat{H}_{\mathrm{B}}$ and $\hat{H}_{\mathrm{I}}$. A commonly used model is that of Caldeira and Leggett, where the system is coupled linearly to harmonic baths, which is discussed below.

1.2.2 Caldeira-Leggett model

The Caldeira-Legget model describes a system coupled to one or more baths of harmonic oscillators. Indexing the oscillators by j, so that x_j and p_j are the position and momentum of the jth oscillator with mass m_j and angular frequency ω_j, the bath's Hamiltonian is

$$\hat{H}_{\mathrm{B}} = \sum_j \left(\frac{p_j^2}{2m_j} + \frac{1}{2} m_j \omega_j^2 x_j^2 \right). \tag{4.5}$$

If the system-bath interaction is sufficiently weak then it can be well approximated with a linear coupling:

$$\hat{H}_{\mathrm{I}} = -\sum_j g_j \hat{F}_j \hat{x}_j, \tag{4.6}$$

where $\hat{F}_j$ is an operator that acts on the system. The advantage of the Caldeira-Leggett model is its simplicity to write down, its amenability to analytical treatments, and its wide range of applicability. The Caldeira-Leggett model has been used to describe Markovian quantum Bronian motion [133, 134], and quantum tunnelling [135, 136], and is a widely used model for approximating system-bath interaction [125].

1.3 Trajectories for open many-body quantum systems

The Langevin approach of describing the fluctuations and dissipation caused by the environment was first used in quantum settings in the 1970s and 1980s [137, 138, 139, 140, 141]. These added noise and friction terms to the closed-system quantum equations of motion. More recently quantum Langevin equations have been used to study quantum optical systems [142], optomechanical systems [143], and even the motion of Bohmian wavepackets [144].

These techniques are targeted at individual quantum systems, and therefore don't provide an account for entanglement in the quantum system. This can be addressed with stochastic Schrödinger equations for the entire wavefunction of a many-body quantum system. However the scope of such an approach is limited by the exponential scaling of the Hilbert space of a many-body quantum system. Matrix product states provide a useful tool for studying the evolution of entanglement in quantum systems, because the size of their description can be tuned by the bond dimension.

One such technique involves combining time-dependent density matrix renormalization methods for evolving matrix product states with 'jump' operators that encode the environmental interaction [145, 146, 147]. These models are derived from master equations for quantum optical systems, which are then unravelled into pure state trajectories under an effective Hamiltonian, with derivatives of the Lindblad operators applies as 'jumps' at random times. This provides useful trajectories in a quantum optics setting by modelling randomly occurring events like spontaneous emission. The jumps can be combined with time-dependent density matrix renormalization methods, which work by applying discretized time-evolution operators to the matrix product state, by modifying the effective Hamiltonian when a jump is to be applied. By using matrix product states, many-body quantum systems undergoing dynamics with limited entanglement can be studied efficiently. This approach is different to the matrix product state Langevin equation discussed later in this chapter, which comes from a different set of approximations, and for example allows the temperature and coupling strength of the environmental interaction to be tuned.

Langevin methods based on assumptions of separability between subsystems, and stochastic trajectories of the entire wavefunction, have their advantages and disadvantages. When entanglement is not important a product state Langevin equation can be shown to work well, and if entanglement is important then a Langevin equation over the full many body state can be applied. However unless the number of subsystems is small or significant simplifications can be made, it is impractical to work with the full many body state. We now go on to discuss how this problem can be addressed by combining Langevin techniques with an efficient, entanglement-based parameterization of the full wavefunction: matrix product states.

2 A quantum Langevin equation for MPS

Existing quantum Langevin equations consist of methods for non-entangled states, or for generic states where entanglement is captured faithfully but the memory scaling is exponential in system size. A middle ground is provided by matrix product states, where the memory size can be tuned between a product state and a generic description, optimizing numerical performance with ability to capture long-range entanglement.

Starting with a Caldeira-Leggett type Hamiltonian, where the system is coupled to an oscillator bath via a system operator $\hat{F}$, we derive a Langevin equation over matrix product states can be derived that takes the form

$$\dot{A}_\alpha = -i\langle \partial_{\bar{A}_\alpha}\psi| \left(\hat{H} - \eta(t)\hat{F} + \gamma \frac{d\langle \hat{F}\rangle}{dt}\hat{F} \right) |\psi\rangle, \tag{4.7}$$

where $\eta(t)$ is a Gaussian white noise related to the frictional strength γ *via* a fluctuation-dissipation relation. Here, the usual terms of the time-dependent variational principle have been supplemented with a stochastic fluctuation term and a frictional dissipative term.

In this section we show how this quantum Langevin equation over matrix product states can be derived, first with a heuristic derivation that communicates the key ideas, and then with a more rigorous derivation from a Keldysh path integral over the system density matrix, which permits a more transparent discussion of the applicability and assumptions underlying the result.

2.1 Heuristic derivation

We split the Hamiltonian into the terms for the isolated system and environment, $\hat{H}_\mathrm{s}$ and $\hat{H}_\mathrm{bath}$, and an interaction term $\hat{H}_\mathrm{int}$:

$$\hat{H} = \hat{H}_\mathrm{s} + \hat{H}_\mathrm{bath} + \hat{H}_\mathrm{int}. \tag{4.8}$$

We keep $\hat{H}_\mathrm{s}$ general for now, set $\hat{H}_\mathrm{bath} = \sum_\alpha \omega_\alpha \hat{a}^\dagger_\alpha \hat{a}_\alpha$, and couple the system and bath via $\hat{H}_\mathrm{int} = \hat{F}_\mathrm{s} \sum_\alpha g_\alpha \left(\hat{a}^\dagger_\alpha + \hat{a}_\alpha \right)$, where $\hat{F}_\mathrm{s}$ is an Hermitian operator that acts on the system. The bath consists of independent quantum harmonic oscillators. For these we work in the coherent state basis $|\phi\rangle = \exp(\phi \hat{a}^\dagger)\,|0\rangle$ where $\hat{a}^\dagger$ is the creation operator and ϕ a complex number. The system state is parameterized by variables z, ie. $|\psi\rangle = |\psi(z)\rangle$.

Here we present a heuristic derivation for the quantum Langevin equation by taking variations about a system+bath time-dependent Schrödinger equation (TDSE).

The result, in the Markovian limit, is

$$i\sum_i G_{ji}\dot{z}_i - \langle\partial_{\bar{z}_j}\psi|\hat{H}_\mathrm{s}|\psi\rangle - [\partial_{\bar{z}}f(\bar{z},z)]\left(\eta(t) - \gamma\partial_t f(\bar{z},z)\right) = 0, \tag{4.9}$$

where $G_{ij} = \langle\partial_{\bar{z}_i}\psi|\partial_{\bar{z}_j}\psi\rangle$ and $f(\bar{z},z) = \langle\psi|\hat{F}|\psi\rangle$. The friction rate γ depends on the coupling strengths g_α and is related to the Gaussian white noise $\eta(t)$ via its variance: $\langle\eta(t)\eta(t')\rangle = 2\gamma T\delta(t-t')$. This is a fluctuation-dissipation relation for the interaction, and depends on the bath temperature T.

Starting from the Schrödinger equation

This derivation follows in spirit the Frenkel principle for deriving the TDVP equations [68], allowing for the effects of coupling to the environment. We start by expanding $i\partial_t|\Psi\rangle$ with a chain rule over the variational parameters z and ϕ_α of the system and bath modes α, respectively. We set this equal to the RHS of the Schrödinger equation and then take carefully chosen inner products to isolate the terms we want.

Before taking the inner products, we have

$$\sum_i |\partial_{z_i}\psi\rangle\,\dot{z}_i\left(\otimes_\alpha|\phi_\alpha\rangle\right) + |\psi\rangle\otimes\sum_\beta\left(\otimes_{\alpha\neq\beta}|\phi_\alpha\rangle\right)|\partial_{\phi_\beta}\phi_\beta\rangle\,\dot{\phi}_\beta \simeq -i\hat{H}\,|\psi\rangle\left(\otimes_\alpha|\phi_\alpha\rangle\right). \tag{4.10}$$

Noting that $\langle\phi|\phi'\rangle = \exp(\bar{\phi}\phi')$ we take an inner product with $\langle\partial_{z_j}|\left(\otimes_{\alpha'}\langle\phi_{\alpha'}|\right)$ to find

$$G_{ji}\dot{z}_i\left(\prod_\alpha e^{\bar{\phi}_\alpha\phi_\alpha}\right) = -i\left(\langle\partial_{\bar{z}_j}\psi|\hat{H}_\mathrm{s}|\psi\rangle + \langle\partial_{\bar{z}_j}\psi|\hat{F}|\psi\rangle\sum_\alpha g_\alpha(\bar{\phi}_\alpha+\phi_\alpha)\right)\prod_\beta e^{\bar{\phi}_\beta\phi_\beta}, \tag{4.11}$$

where we have used $\hat{a}|\phi\rangle = \phi|\phi\rangle$ and $\langle\partial_{z_j}\psi|\psi\rangle = 0$, and also defined $G_{ji} = \langle\partial_{\bar{z}_j}\psi|\partial_{z_i}\psi\rangle$. Cancelling the common phase factors and identifying $\partial_{\bar{z}}f_\alpha(\bar{z},z) = \langle\partial_{\bar{z}}\psi|\hat{O}_\mathrm{s}|\psi\rangle$, we have:

$$G_{ij}\dot{z}_j = -i\,\langle\partial_{\bar{z}_j}\psi|\hat{H}_\mathrm{s}|\psi\rangle - i\partial_{\bar{z}_j}f(\bar{z},z)\sum_\alpha g_\alpha(\bar{\phi}_\alpha+\phi_\alpha). \tag{4.12}$$

Now we instead take an inner product of Eq. (4.10) with $\langle\psi|\left(\otimes_\alpha\langle\phi_\alpha|\right)$ to find

$$\sum_\alpha\bar{\phi}_\alpha\dot{\phi}_\alpha = -i\,\langle\psi|\hat{H}_\mathrm{s}|\psi\rangle - i\sum_\alpha\omega_\alpha\bar{\phi}_\alpha\phi_\alpha - i\sum_\alpha f_\alpha(\bar{z},z)(\phi_\alpha+\bar{\phi}_\alpha). \tag{4.13}$$

Differentiating this with respect to $\bar{\phi}_\alpha$ (for some particular value of the bath index α) yields us:

$$\dot{\phi}_\alpha = -i\omega_\alpha - f_\alpha(\bar{z},z). \tag{4.14}$$

We can use an integrating factor of $\exp(i\omega_\alpha t)$ and integrate this by parts to find an expression for $\phi_\alpha(t)$:

$$\phi_\alpha(t) = \phi_\alpha(0)e^{-i\omega_\alpha t} - \int_0^t ie^{i\omega_\alpha(t'-t)}f(\bar{z},z)dt'. \tag{4.15}$$

Combining to form quantum Langevin equation: First we define the retarded Green's function for the bath as, up to normalization,

$$ie^{i\omega(t'-t)} \to G^R(t'-t) = -i\Theta(t-t')\left\langle \hat{a}^\dagger(t')\hat{a}(t)\right\rangle, \tag{4.16}$$

where Θ is the Heaviside theta-function. We can then substitue Eq. (4.15) into Eq. (4.12) to find

$$\begin{aligned} iG_{ij}\dot{z}_j - \langle\partial_{\bar{z}_j}\psi|\hat{H}_\mathrm{s}|\psi\rangle =& [\partial_{\bar{z}}f(\bar{z},z)](\bar{\phi}(0)e^{i\omega t} + \phi(0)e^{-i\omega t}) \\ &+ [\partial_{\bar{z}}f(\bar{z},z)]\biggl(\int_0^t G^R(t'-t)f(\bar{z},z)dt' \\ &- \int_0^t \overline{G^R(t'-t)}\,\overline{f(\bar{z},z)}dt'\biggr). \end{aligned} \tag{4.17}$$

The terms in $\phi(0)$ we treat as stochastic noise and define as $\eta(t)$. The second integral is zero because of the Heaviside function in the definition of G^R. We can make progress with the first integral by defining $\partial_t\Gamma(t) = G^R(t)$. Integrating by parts we find

$$i\sum_i G_{ji}\dot{z}_i - \langle\partial_{\bar{z}_j}\psi|\hat{H}_\mathrm{s}|\psi\rangle - [\partial_{\bar{z}}f(\bar{z},z)]\left(\eta(t) - \int_0^t \Gamma(t'-t)\partial_t f(\bar{z},z)dt'\right) = 0. \tag{4.18}$$

Limit of high-temperature, Ohmic bath: The fluctuation dissipation theorem tells us that the noise $\eta(t)$ and dissipation (given by the time integral of the retarded Green's function of the bath $\Gamma(t)$) due to the same bath oscillator obey the following relations:

$$\langle\eta(t)\eta(t')\rangle = \frac{1}{4\pi}\int_0^\infty d\omega J(\omega)\cos(\omega t)\coth\left(\frac{\omega}{2T}\right). \tag{4.19}$$

$$\Gamma(t) = \frac{1}{2\pi}\int_0^\omega \frac{d\omega}{\omega}J(\omega)\cos(\omega t). \tag{4.20}$$

For an Ohmic bath the bath spectral function is $J(\omega) = 4\gamma\omega$. If we also work in the high temperature limit $T \gg \omega$ where ω is the frequency scale of interest, our quantum Langevin equation emerges as

$$i\sum_i G_{ji}\dot{z}_i - \langle\partial_{\bar{z}_j}\psi|\hat{H}_\mathrm{s}|\psi\rangle - [\partial_{\bar{z}}f(\bar{z},z)]\left(\eta(t) - \gamma\partial_t f(\bar{z},z)\right) = 0, \tag{4.21}$$

with a delta-correlated second moment of the noise fields, $\langle\eta(t)\eta(t')\rangle = 2\gamma T\delta(t-t')$.

This high-temperature limit of an Ohmic bath is a separation of frequency scales that is equivalent to a Markov approximation.

Box 2.1 illustrates this quantum Langevin equation for a single spin coupled to a harmonic bath.

Box 2.1 Toy model: one spin coupled to bath

This Langevin equation was used in [148] to derive an anisotropic Landau-Lifschitz-Gilbert equation for isolated spins coupled to a bath in just one direction. Taking $\hat{\mathcal{H}} = -\vec{\sigma} \cdot \vec{B}/2$ and $\hat{F} = \sigma_z$, an equation of motion for the Pauli vectors $\vec{s} = \langle \hat{\vec{\sigma}} \rangle$ can be derived:

$$\dot{\vec{s}} = \vec{s} \times (\vec{B} + \eta(t)\hat{\vec{z}}) - \gamma \dot{s}_z \vec{s} \times \hat{\vec{z}},$$

where $\hat{\vec{z}}$ is the z-direction unit vector. The form of the environmental coupling is fairly clear here: as well as the Hamiltonian procession $\dot{\vec{s}} = -\vec{s} \times \vec{B}$, the spin feels a fluctuating field in the z-direction, and a dissipative field also in the z-direction and proportional to $\dot{s}_z$. This dissipative field will try to draw energy from the system to the bath, by aligning $\vec{s}$ with $\vec{B}$. How well it achieves this depends on γ and the the temperature of the bath T, which controls the strength of the noise fluctuations via Eq. 4.34.

2.2 Derivation from Keldysh field theory

A more complete derivation may be made using the tools of Keldysh field theory. This section now concludes by giving this derivation. The approach taken is similar to that presented in [119] and [148]. The key difference – and the new feature of the present work – is the derivation for evolution over matrix product states.

2.2.1 Forming a Keldysh path integral from the propagator

The fundamental object in Keldysh field theory is a partition function Z. This is written in terms of a propagator for the system+bath density matrix $\hat{\rho}(A, \{x_k\})$. Since this is an operator it is evolved in time via $e^{-i\int \hat{H} dt} \hat{\rho} e^{i\int \hat{H} dt}$. The forwards and backwards parts instantiate the Keldysh time contour. Here A denotes all of system fields, and $\{x_k\}$ are the bath fields, indexed by k. Under a certain set of assumptions [discussed below], this is equivalent to an ensemble of trajectories described by a quantum Langevin equation.

Forming the Keldysh path integral begins with the following expression for the partition function:

$$Z = \frac{\mathrm{Tr}\{\hat{\mathcal{U}}_C \rho_{-\infty}\}}{\mathrm{Tr}\{\hat{\rho}_{-\infty}\}} = \frac{\mathrm{Tr}\{\hat{\mathcal{U}}_{-\infty,+\infty} \hat{\rho}_{-\infty} \hat{\mathcal{U}}_{+\infty,-\infty}\}}{\mathrm{Tr}\{\hat{\rho}_{-\infty}\}}, \tag{4.22}$$

where $\mathcal{U}_C$ is the unitary time-evolution operator along the 'Keldysh contour' C, which follows the (real) time axis from negative to positive infinity and then back again. Here we perform this for a system parameterized by a matrix product state in contact with a harmonic bath as described in Eqs 4.5,4.6.

Writing a path integral over Matrix Product States

A path integral over matrix product states was introduced in [65], where the key insight was to introduce resolutions of the identity into the time evolution over matrix product states. Ignoring the bath for now, we can insert resolutions of the identity into the time-evolution operator $\hat{\mathcal{U}}_C$ at regular time intervals Δt and take the limit $\Delta t \to 0$. This gives us a path integral $Z = \int DA e^{iS[A]}$, where $A(t)$ represents the matrix product state variables at time t, and DA is a gauge-invariant measure over these variables. The existence and construction of a suitable gauge was demonstrated in [65], where it was also shown how the path integral may be made local, meaning the standard techniques for manipulating path integrals may be applied.

2.2.2 Derivation

This derivation consists of standard manipulations of a non-standard MPS Keldysh path integral [119, 65]. Starting with the partition function in Eq 4.22, we insert resolutions of the identity into the forwards and backwards time evolution operators to write Z as a path integral. The system is parameterized by matrix product state variables A, and the baths by their positional and moment operators x_k, p_k. Because the Keldysh contour runs the length of the time axis and back again, it is necessary to distinguish fields on the forward part of the contour ('+') from those on the backwards part ('-'). A Keldysh rotation is then performed, forming 'classical' and 'quantum' fields as the sum and difference of the forward and backwards fields. Ie, $A^{\mathrm{cl}} = (A^+ + A^-)/2$ and $A^{\mathrm{q}} = (A^+ - A^-)/2$. These are so-called because the saddle point equations derived from a Keldysh path integral become recognizable classical equations in the classical fields, provided fluctuations in the quantum field can be considered small. In a path integral over matrix product states the saddle point gives the time-dependent variational principle equations over matrix product states, which include a degree of quantum entanglement. So that this doesn't become misleading, the 'cl' superscript will be dropped for the classical fields.

The next step is to expand to linear order in the quantum fields. Starting with a linear coupling between the system and harmonic baths, as described in equations 4.5, 4.6, the action is now of the following form

$$S = \int_{-\infty}^{+\infty} (\mathcal{L}_S + \mathcal{L}_{\text{int}} + \mathcal{L}_{\text{bath}}) dt, \tag{4.23}$$

with system, bath and interaction Lagrangians given by

$$\mathcal{L}_S = 2 \sum_\alpha A_\alpha^{\text{q}} \left(\frac{\partial \mathcal{L}_0}{\partial A_\alpha} - \frac{d}{dt} \frac{\partial \mathcal{L}_0}{\partial \dot{A}_\alpha} \right) \tag{4.24}$$

$$\mathcal{L}_{\text{bath}} = 2 \sum_k \begin{pmatrix} x_k & x_k^{\text{q}} \end{pmatrix} \begin{pmatrix} F^{\text{q}} \\ F \end{pmatrix} \tag{4.25}$$

$$\mathcal{L}_{\text{int}} = \sum_k \begin{pmatrix} x_k & x_k^{\text{q}} \end{pmatrix} \begin{pmatrix} 0 & [D_k^A]^{-1} \\ [D_k^R]^{-1} & [D_k^{-1}]^K \end{pmatrix} \begin{pmatrix} x_k \\ x_k^{\text{q}} \end{pmatrix}. \tag{4.26}$$

The system Langrangian is given in terms of the bare Lagrangian $\mathcal{L}_0$. Matrix product state variables are indexed by α, and bath oscillators by k. F and F^{q} are the classical and quantum parts of the expectations of the system operator $\hat{F}$ that couples to the oscillators (ie. $F^q = A^q \cdot \partial F / \partial A$). This action is quadratic in the bath variables, a fact which is used later to integrate these variables out. D^A, D^R, D^K are the advanced, retarded and Keldysh correlators, and appear in the action in an inverted form:

$$\underline{\underline{D}}^{-1} = \begin{pmatrix} D_k^K & D_k^R \\ D_k^A & 0 \end{pmatrix}^{-1} = \begin{pmatrix} 0 & [D_k^A]^{-1} \\ [D_k^R]^{-1} & [D_k^{-1}]^K \end{pmatrix}. \tag{4.27}$$

The Keldysh correlator originates at the turning point of the Keldysh contour ie. $t = +\infty$, and encodes a fluctuations dissipation relation between the system and bath. For bath temperature T, the Fourier components of these correlators are [119]:

$$D_k^{R(A)}(\omega) = \frac{1}{2} \frac{1}{(\omega \pm i0)^2 - \omega_0^2}, \tag{4.28}$$

$$D_k^K(\omega) = \coth\left(\frac{\omega}{2T}\right) \left[D_k^R(\omega) - D_k^A(\omega) \right], \tag{4.29}$$

where the latter equation is a statement of the fluctuation dissipation theorem.

As already mentioned, this action is quadratic in each of the bath fields, ie. the partition function is a Gaussian integral over these. This integral may be performed to give a dissipative action for the system:

$$S_{\text{diss}} = \int_{-\infty}^{+\infty} \begin{pmatrix} F & F^{\text{q}} \end{pmatrix} \begin{pmatrix} 0 & D^A \\ D^R & D^K \end{pmatrix} \begin{pmatrix} F \\ F^{\text{q}} \end{pmatrix}, \tag{4.30}$$

where the unindexed correlators are defined through $D^X = \sum_k g_k^2 G_k^X$ for $X = A, R, K$. This dissipative action is quadratic in the system's quantum fields A^{q}, ie. it looks like the result of a Gaussian integral. A Hubbard-Stratonovich transformation 'undoes' this hypothetical Gaussian integral, with the effect of linearizing the action in the A^{q} fields, and introducing the integration variable $\eta(t)$. This will become the stochastic factor in the Langevin equation. The result of the Hubbard-Stratonovich transformation is

$$\begin{aligned} S_{\text{diss}} &= \int_{-\infty}^{+\infty} dt \left(2F^{\text{q}} D^R F + 2F^q \eta - \eta [D^K]^{-1} \eta \right) && (4.31) \\ &= \int_{-\infty}^{+\infty} dt A^{\text{q}} \cdot \left(2\frac{\partial F}{\partial A} D^R F + 2\frac{\partial F}{\partial A}\eta - \eta [D^K]^{-1} \eta \right). && (4.32) \end{aligned}$$

The total action now looks like $S = \int_{\mathbb{R}} \mathcal{L}_0 dt + S_{\text{diss}}$, with both of these terms linear in the matrix product state fields A^{q}. These may now be integrated out of the partition function to yield a delta function action for the system variable. This leads to the following equation of motion for the system matrix product state. Working in a Markovian approximation, in which $G^R(t-t') = \pm\gamma\delta(t-t')\partial_{t'}$, we have

$$\frac{d}{dt}\frac{\partial \mathcal{L}_0}{\partial \dot{A}_\alpha} - \frac{\partial \mathcal{L}_0}{\partial A_\alpha} + \gamma \frac{\partial F}{\partial A_\alpha}\frac{dF}{dt} = \frac{\partial F}{\partial A_\alpha}\eta. \tag{4.33}$$

The first two terms are in fact the time-dependent variational principle equations for closed evolution of the system through the matrix product state manifold. The next term, proportional to γ, is the dissipative term, depending also on dF/dt. The term on the RHS accounts for fluctuations in the system via the (Gaussian, white noise) stochastic variable η. The fluctuation dissipation relation is reflected in the properties of η, having zero mean and a variance given by

$$\langle \eta(t)\eta(t') \rangle = 2\gamma T \delta(t-t'), \tag{4.34}$$

where T is the bath temperatures.

Evaluating Eq 4.33 with $\mathcal{L}_0 = \langle i\delta_t - \hat{\mathcal{H}} \rangle$ we obtain Langevin modifications to the time-dependent variational principle equations for matrix product states. A matrix product state typically describes a spin-chain system, or equivalent. In such a system a reasonable model of the environmental coupling is that each subsystem should be coupled to its own oscillator bath. If the interaction Hamiltonian is duplicated to account for multiple local couplings $\hat{F}_k$ to independent oscillator baths, the above derivation is easily extended to yield

$$i\sum_{\beta}\langle\partial_{\bar{A}^{\alpha}}\psi|\partial_{A^{\beta}}\psi\rangle\dot{A}^{\beta}=\langle\partial_{\bar{A}^{\alpha}}\psi|\hat{\mathcal{H}}|\psi\rangle+\sum_{k}\left(\gamma_k\frac{d\langle\hat{F}_k\rangle}{dt}\langle\partial_{\bar{A}^{\alpha}}\psi|\hat{F}_k|\psi\rangle-\eta_k(t)\langle\partial_{\bar{A}^{\alpha}}\psi|\hat{F}_k|\psi\rangle\right). \tag{4.35}$$

These equations are worked through for the particular example of two spin-1/2s in box 2.2.2.

Discussion

The Langevin equation over matrix product states (4.35) models a system in thermal contact with oscillator baths, and parameterized by matrix product states. In addition to the time-dependent variational principle, the evolution of the system through the matrix product state manifold is affected by friction and noise terms. The friction terms depend on a friction parameter γ and the rate of change of the relevant coupling operator $d\langle\hat{F}\rangle/dt$. The fluctuating noise terms have a Gaussian white noise $\eta(t)$ as a prefactor, having zero mean and delta-correlated variance equal to $2\gamma T$ at equal times.

Forming the Keldysh path integral over a basis of matrix product states, instead over non-entangled product states as is usual, allows the resulting saddle-point dynamics to capture quantum entanglement. This engenders a difference of interpretation in the 'quantum' and 'classical' fields along the Keldysh contour. Usually path integrals are constructed over product states, and expanding to linear powers in the quantum fields leads to classical equations of motion in just the classical fields - hence the terminology. However here the prescription has been to use matrix product states, and expanding to linear powers in the quantum fields leads in fact to the time-dependent variational principle for the system. For unbounded bond dimension this recovers the time-dependent Schrödinger equation.

This approach allows the tunability of matrix product state manifolds to be combined with Langevin modelling of an open quantum system, where noise and friction effects can be independently tuned. One downside to Langevin equations is that they can get the wrong thermal equilibrium values for certain systems. Averages over Langevin trajectories sample over the variational manifold instead of energy eigenstates. This is particularly apparent in the case of a single spin, which is examined in more depth in Sec 2, but less of a problem in larger collections of spins. The above derivation is applicable to more than just matrix product states, and would look the same for any complex variational parameterization of the system state.

One technical challenge in evaluating the matrix product state Langevin equation comes from the non-locality of matrix product states - in effect, each tensor sees not just its own bath, but all the other baths too. This leads to non-locality in $\langle\hat{F}_k\rangle$, the time-derivative of which appears in the friction term. Expanding this we have $\partial_t\langle\hat{F}_k\rangle = \langle\psi|\hat{F}|(\partial_t|\psi\rangle) + h.c. = \langle\psi|\hat{F}\sum_\beta |\partial_{A^\beta}\psi\rangle\dot{A}^\beta + h.c.$, where the summation index β runs over all the subsystems, not just that relating to $\hat{F}_k$. The dissipation term therefore couples this matrix product state tensors *via* a transcendental set of equations. Solving these requires methods beyond those used to solve the closed-system time-dependent variational principle for matrix product states.

Box 2.2.2 Simple case: two spins

Here we apply the matrix product state Langevin equation to the case of two spin-1/2s, each coupled to a bath via local operators $\hat{F}_i$, where $i = 1, 2$ indexes the spins. Using the left-gauge tangent basis, only the second site's tensor will be updated[a]: $\dot{A}^{[1]} = 0$, $\dot{A}_i^{[2]\sigma} = \sum_j V_{L,ij}^\sigma \dot{X}$. Applying the Langevin equation (4.35), we find i. the Hamiltonian and noise parts looks like regular TDVP with a stochastic Hamiltonian $\hat{\mathcal{H}}_{\mathrm{st}} = \hat{\mathcal{H}} + \sum_i \eta_i \hat{F}_i$; ii. the friction terms look like

$$\gamma_i \partial_t \langle\hat{F}_i\rangle \langle\partial_{\dot{\bar{X}}}\psi|\hat{F}_i|\psi\rangle, \tag{4.36}$$

where

$$\begin{aligned} \partial_t\langle\hat{F}_i\rangle &= \langle\dot{\psi}|\hat{F}_i|\psi\rangle + \langle\psi|\hat{F}_i|\dot{\psi}\rangle & (4.37) \\ &= \dot{\bar{X}}\langle\partial_{\bar{X}}\psi|\hat{F}_i|\psi\rangle + \langle\psi|\hat{F}_i|\partial_X\psi\rangle\dot{X}. & (4.38) \end{aligned}$$

The consequences for evaluating the Langevin equation are twofold: i. this is a stochastic differential equation and will need to be treated as such, and ii. the equation for $\dot{X}$ is transcendental: it depends in a non-trivial way on itself and its complex conjugate. These aspects will be treated in more detail in Sec. 3.

---

[a] As long as there is some entanglement in the system so that $A^{[1]}$ is full rank.

Integrating the matrix product state Langevin equation numerically is not straightforward. In the following we discuss the techniques developed to achieve this.

3 Numerical Implementation

A numerical algorithm for evolving the Langevin equation over matrix product states will allow the study of systems of many spins/qubits, revealing the interplay of internal entanglement structure with the coupling to the bath. In this section I describe how the methods for numerically integrating the time-dependent variational principle are extended to deal with the Langevin equation. These extensions are i. proper treatment of the stochastic element, and ii. evaluating the non-local and transcendental dissipative term.

I begin with the noise effect and the elements of stochastic calculus required to evaluate it. The dissipative effect is particularly troublesome: without dissipation, the equation of motion can be integrated by updating one tensor at a time. However, even with a bath of independent local harming oscillators, the non-local entanglement structure embodied by the tensor network allows distant parts of the environment to affect the tensors on any given site. In the latter part of this section we show how this can be accounted for, and simplified in the case where the subsystems are only entangled locally.

3.1 Noise term

Setting the dissipative term to one side for the moment, the matrix product state Langevin equation with just the noise term looks the same as the time-dependent variational principle, only with a stochastic effective Hamiltonian. They can therefore be evaluated with the techniques discussed in chapter 2. However convergence for stochastic differential equations works quite differently.

In this subsection I will give a brief summary of relevant stochastic differential equation methods, starting with how convergence criteria are defined, going on to discuss Ito and Stratonovich definitions of the differential, and finally focussing in on some strongly convergent methods. A full discussion can be found in the book by Kloeden and Platen [149].

3.1.1 Numerical methods for stochastic differential eqns

A stochastic different equation in one dimension X can be written in the form

$$dX_t = a(X_t)dt + b(X_t)dW_t. \tag{4.39}$$

The first term depends non-deterministically on some function $a(X_t)$ of the current value of X and the time differential dt. The second term depends on the differential of a (stochastic) Wiener process W_t. This is a zero-mean, unit variance stochastic process, which has no degree of autocorrelation: $\langle W_t W_{t' \neq t} \rangle = 0$.

Apart from particular examples where the stochastic differential equation can be solved exactly, the usual approach to studying such equations is to numerically integrate forwards with a finite stepsize Δt. The corresponding step in the Wiener process is $\Delta W_t = W_{t+\Delta t} - W_t$ and satisfies

$$\langle \Delta W_t \rangle = 0, \quad \langle (\Delta W_t)^2 \rangle = \Delta t. \tag{4.40}$$

These can be simulated in practice by generating a random number from a zero mean, unit variance Gaussian distribution, and then multiplying by $\sqrt{\Delta t}$. Sampling a realization of the Wiener process W_t realizes a particular trajectory. Many trajectories can be found to study the statistical properties of the solution to the underlying equation.

Unfortunately, numerical methods for integrating deterministic differential equation can't usually be ported straightforwardly to stochastic different equations. For many techniques, the resulting trajectories do not converge in any meaningful way as the stepsize $\Delta t \to 0$. There are two criteria used to define convergence in numerical methods for stochastic differential equations, known as 'strong' and 'weak' convergence criteria.

A numerical method is weakly convergence if the trajectories it produces give, *on ensemble average*, converging values for $\langle X_t^n \rangle$ for $n = 1, 2, \ldots$ as the stepsize $\Delta t \to 0$. A strongly convergent method on the other hand should give trajectories that converge individually as the stepsize is decreased.

For integrating the matrix product state Langevin equation, stepsizes are chosen so that the trajectories produced are converged in the strong sense, allowing an interpretation of the results as possible realizations of a physical process. The method used is a simple Euler step, which has a basic convergence order of 0.5 in Δt.

3.1.2 Ito and Stratonovich differentials

One subtlety in dealing with stochastic differential equations relates to how the underlying Wiener process W_t is sampled. In general, for a step from time t to $t + \Delta t$, W_t can be taken from anywhere in the interval $[t, t + \Delta t]$. The two most common choices are the Itô differential, where W_t is taken at the end of the interval, and the Stratonovich differential, where W_t is taken at the centre.

The choice of Itô or Stratonovich leads to self-consistent, but potentially quite different strongly convergent trajectories. In this research the Stratonovich interpretation is used. This is motivated by the Wong-Zakai theorem [149, 150, 151], which shows that the Stratonovich differential is most appropriate when the Wiener process is an approximation of a time-correlated process. This is indeed the case for the Markovian fluctuations from the environment characterized in Eq. 4.34.

3.1.3 Strong convergence in the MPS Langevin equation

Here I discuss strongly convergent methods for evaluating the matrix product state Langevin equation. First I describe the Euler- Maruyama method, which is a straightforward application of the regular Euler method to the Wiener increment ΔW_t, and is straightforward to evaluate. A demonstration of the code written for this research finding strongly converged trajectories is given.

Euler-Maruyama method

The Euler-Maruyama method approximates the solution of Eq. 4.39 with the process Y_n, where n indexes times $t_n = t_0 + n\Delta t$ [149]:

$$Y_{n+1} = Y_n + a(Y_n)\Delta t + b(Y_n)\Delta W_n. \tag{4.41}$$

For well-behaved functions a and b the trajectories Y will strongly converge as $(\Delta t)^{0.5}$.

Fig 4.1 demonstrates the convergence of solutions of the matrix product state Langevin equation for a system of x qubits under the influence of a randomized Hamiltonian and anisotropic coupling to oscillator baths. This can be achieved by running with the same parameters at different stepsize. Care needs to be taken that this is done properly for the underlying Wiener process, here this is achieved by using a reference process with 2520 steps and coarse grained processes with exact divisors as the number of steps. 2520 is a highly composite number, so this allows 16 different levels of coarse-graining above 100 steps each. This is repeated for 10 different noise processes, and the average error in fidelity compared with the stepsize, showing in this case strong convergence scaling with $(\Delta t)^2$ for this particular error measure.

Higher order schemes involve calculating derivatives in the prefactor of dW in the stochastic term. This is highly non-trivial for the multi-dimensional matrix product state Langevin equation, and so the Euler-Maryama method is used here.

3.2 Friction term

The dissipative friction term is the source of the fundamental difficulty of evaluating the matrix product state Langevin equation. Whereas in closed evolution the equation

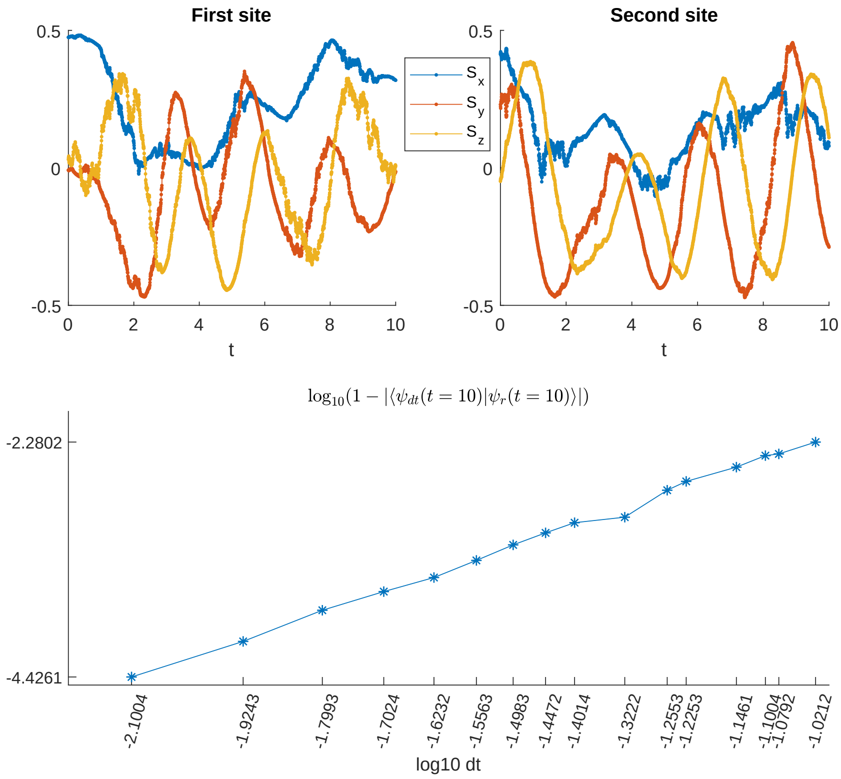

Figure 4.1: *Demonstrating convergence of stochastic matrix product state Langevin equation.* A 2-qubit system anisotropically coupled to oscillator baths evolves according to the matrix product state Langevin equation in the dephasing limit, $\gamma \to 0$, γT finite. Trajectories are calculated for 10 different Wiener processes and the resulting errors averaged to give an estimate of the order of strong convergence. Top: evolution of the expectations of the x,y and z spin operators for the first and second site in one of the reference trajectories $|\psi_r(t)\rangle$. This uses 2520 steps to evolve through 10 units of time. The Hamiltonian terms and temperatures are of order 1. Bottom: convergence in final state fidelity error for trajectories with larger stepsize dt sampling the same Wiener process. The order of convergence can be estimated from the slope of this graph as $\simeq 2$.

of motion for the tensors on each site decouple, the friction is fundamentally non-local and couples the sites together. This has consequences for the scaling of such an approach, giving a quadratic increase in the number of terms to be evaluated. However frictional inter-site coupling between weakly entangled parts of the system will be correspondingly weak, so if local entanglement is expected then savings can be made by imposing a maximum length for frictional coupling.

In this subsection I explain the techniques developed to compute the friction term. First I show how the matrix product state Langevin equation may be rearranged to find an explicit form for the tensor updates. Then I present an algorithm for adapting finite-chain time dependent variational principle methods for the Langevin equation. Finally I discuss how, by approximating the friction as being local to some degree, a more efficient friction update may be made.

3.2.1 Explicit expression for friction

Following the notation of Chapter 2, the update for the ith component of a matrix product state in the matrix product state Langevin equation can be written in terms of the tangent vector $|\delta\psi\rangle$ as

$$\Delta X_i = -i\langle \partial_{X_i^*}\delta\psi|\left(\hat{H}\Delta t - \hat{F}\Delta W\right)|\psi\rangle - i\gamma\frac{d\langle\hat{F}\rangle}{dt}\langle\partial_{X_i^*}\delta\psi|\hat{F}|\psi\rangle, \tag{4.42}$$

where the system Hamiltonian is $\hat{H}$ and for now we consider a single coupling to a bath via $\hat{F}$. Writing $d\langle\hat{F}\rangle/dt = \langle\partial_t\psi|\hat{F}|\psi\rangle + \langle\psi|\hat{F}|\partial_t\psi\rangle$ and expanding in terms of the matrix product state updates ΔX_j we can see that

$$\frac{d\langle\hat{F}\rangle}{dt} = \sum_j \left(\Delta X_j^*\langle\partial_{X_j^*}\delta\psi|\hat{F}|\psi\rangle + \langle\psi|\hat{F}|\partial_{X_j}\delta\psi\rangle\Delta X_j\right). \tag{4.43}$$

These expressions illustrate the difficulty of solving for the frictional update. Whereas the first term on the RHS of Eq 4.42 can be straightforwardly calculated for each tensor in the matrix product state, the frictional part couples all of these updates together with their complex conjugates.

This can be made more clear by defining $h_j = -i\langle\partial_{X_j^*}\delta\psi|\hat{H}|\psi\rangle$ (so that the time-dependent principle is $\Delta X_j = -ih_j\Delta t$), and $q_j = -i\langle\partial_{X_j^*}\delta\psi|\hat{F}|\psi\rangle$. Furthermore, if the elements of $\Delta X, h, j$ are reshaped into column vectors $\Delta\vec{X}, \vec{h}, \vec{k}$, we have

$$\Delta\vec{X} = \vec{h}\Delta t - \vec{q}\Delta W + \gamma\vec{q}\left(i\Delta\vec{X}^\dagger\vec{q} - i\vec{q}^\dagger\Delta\vec{X}\right) \tag{4.44}$$

$$= \vec{h}\Delta t - \vec{q}\Delta W - i\gamma\vec{q}\begin{pmatrix}\vec{q}\\ -\vec{q}^*\end{pmatrix}^\dagger\begin{pmatrix}\Delta\vec{X}\\ \Delta\vec{X}^*\end{pmatrix}, \tag{4.45}$$

together with the conjugate equation for $\Delta\vec{X}^*$. Note that since $d\langle\hat{F}\rangle/dt$ is real, this looks the same in the conjugate equation. Finally, these equations can be merged by combining the vectors with their conjugates to define $\Delta\mathcal{X} = \left(\Delta\vec{X}, \quad \Delta\vec{X}^*\right)^\intercal$, $\mathcal{H} = \left(\vec{h}, \vec{h}^*\right)^\intercal$, $\mathcal{Q} = \left(\vec{q}, \quad \vec{q}^*\right)^\intercal$ and $\mathcal{Q}' = \left(\vec{q}, -\vec{q}^*\right)^\intercal$. This gives

$$\Delta\mathcal{X} = \mathcal{H}\Delta t - \mathcal{Q}\Delta W - i\gamma\mathcal{Q}\mathcal{Q}'^\dagger\Delta\mathcal{X}, \tag{4.46}$$

or for the case of multiple couplings to the bath, labelled by k, via system operators $\{\hat{F}^{[k]}\}$:

$$\Delta\mathcal{X} = \mathcal{H}\Delta t - \sum_k \left(\mathcal{Q}^{[k]}\Delta W^{[k]} + i\gamma^{[k]}\mathcal{Q}^{[k]}\mathcal{Q}^{[k]\prime\dagger}\Delta\mathcal{X}\right). \tag{4.47}$$

In these equations $\Delta\mathcal{X}$ appears on both the LHS and RHS, which demands an extension to the techniques of evaluating the time-dependent variational principle.

One coupling operator The case of just one coupling operator is simple enough that Eq 4.46 can rearranged for $\Delta\mathcal{X}$. This can be done by working in the 2D subspace of $\mathcal{Q}$ and $\mathcal{Q}'$. If the updates $\Delta\vec{X}$ are found in the central gauge, then it is straightforward to show that $\vec{q}^\dagger\vec{q} = \langle\hat{F}^2\rangle$, and therefore $\mathcal{Q}$ and $\mathcal{Q}'$ are orthogonal and have norm $2\langle\hat{F}^2\rangle$. The friction term can then be brought onto the LHS and inverted:

$$\begin{aligned}
&\Delta\mathcal{X} &&= \mathcal{H}\Delta t - \mathcal{Q}\Delta W - i\gamma\mathcal{Q}\mathcal{Q}'^\dagger\Delta\mathcal{X} && (4.48)\\
\implies &\left(\mathbb{1} + i\gamma\mathcal{Q}\mathcal{Q}'^\dagger\right)\Delta\mathcal{X} &&= \mathcal{H}\Delta t - \mathcal{Q}\Delta W && (4.49)\\
\implies &\left(\hat{\mathbb{P}}_{T_{\mathcal{Q}\mathcal{Q}'}} + \begin{pmatrix} 1 & 2i\gamma\langle\hat{F}^2\rangle \\ 0 & 1 \end{pmatrix}\right)\Delta\mathcal{X} &&= \mathcal{H}\Delta t - \mathcal{Q}\Delta W, && (4.50)
\end{aligned}$$

where in the last line $\hat{\mathbb{P}}_{T_{\mathcal{Q}\mathcal{Q}'}}$ is the projector onto the orthogonal space to $\mathcal{Q}$ and $\mathcal{Q}'$, and the 2x2 matrix is written the basis of normalized $\mathcal{Q}$ and $\mathcal{Q}'$ vectors. This matrix can be inverted to find

$$\begin{aligned}
\Delta\mathcal{X} &= \left(\hat{\mathbb{P}}_{T_{\mathcal{Q}\mathcal{Q}'}} + \begin{pmatrix} 1 & -2i\gamma\langle\hat{F}^2\rangle \\ 0 & 1 \end{pmatrix}\right)\left[\mathcal{H}\Delta t - \mathcal{Q}\Delta W\right] && (4.51)\\
&= \left(\mathbb{1} - i\gamma\mathcal{Q}\mathcal{Q}'^\dagger\right)\left[\mathcal{H}\Delta t - \mathcal{Q}\Delta W\right], && (4.52)
\end{aligned}$$

where the norms of $\mathcal{Q}$ and $\mathcal{Q}'$ have been re-absorbed in the last line.

Defining the frictionless change in $\mathcal{X}$ as $\Delta\mathcal{X}_0 = \left(\Delta\vec{X}_0, \quad \Delta\vec{X}_0^*\right)^\intercal$ and the (first-order) variation in $\langle\hat{F}\rangle$ due to $\Delta\mathcal{X}_0$ as $\Delta\langle\hat{F}\rangle_0 = \Delta\vec{X}_0^\dagger\partial_{\vec{X}^*}\langle\hat{F}\rangle + \Delta\vec{X}_0^\intercal\partial_{\vec{X}}\langle\hat{F}\rangle = -i\mathcal{Q}'^\dagger\Delta\mathcal{X}_0$, we get

$$\Delta\mathcal{X} = \Delta\mathcal{X}_0 + \gamma\mathcal{Q}\Delta\langle\hat{F}\rangle_0. \tag{4.53}$$

In terms of $\Delta\vec{X}$ this reads:

$$\Delta\vec{X} = \Delta\vec{X}_0 + \gamma\vec{q}\,\Delta\langle\hat{F}\rangle_0, \tag{4.54}$$

or if we unpack the notation,

$$\Delta\vec{X}_j = -i\langle\partial_{\bar{X}_j}\delta\psi|(\hat{H}\Delta t - \hat{F}\Delta W + \gamma\hat{F}\Delta\langle\hat{F}\rangle_0)|\psi\rangle, \tag{4.55}$$

where

$$\begin{aligned}
\Delta\langle\hat{F}\rangle_0 &= \hat{H}\Delta t - \hat{F}\Delta W)|\psi\rangle\langle\psi|\hat{F}|\partial_{X_k}\delta\psi\rangle + c.c. && (4.56)\\
&= -i\left\langle[\hat{H},\hat{F}]\Delta t - [\hat{F},\hat{F}]\Delta W\right\rangle && (4.57)\\
&= -i\left\langle[\hat{H},\hat{F}]\right\rangle\Delta t, && (4.58)
\end{aligned}$$

finally giving us

$$\begin{aligned}
\Delta\vec{X}_j &= -i\langle\partial_{\bar{X}_j}\delta\psi|(\hat{H}\Delta t - \hat{F}\Delta W - i\gamma\hat{F}\langle[\hat{H},\hat{F}]\rangle\Delta t)|\psi\rangle && (4.59)\\
&= \ \vec{h}_j\Delta t - \vec{q}_j\Delta W - i\gamma\langle[\hat{H},\hat{F}]\rangle\ \vec{q}_j\Delta t && (4.60)
\end{aligned}$$

We see the friction term recast as deterministic and imaginary, and proportional to the commutator between the Hamiltonian and the coupling operator.

Multiple coupling operators In the general case of multiple coupling operators we can get as far as Eq 4.49:

$$\left(\mathbb{1} + i\sum_k \gamma^{[k]}\mathcal{Q}^{[k]}\mathcal{Q}^{[k]\prime\dagger}\right)\Delta\mathcal{X} = \mathcal{H}\Delta t - \sum_k \mathcal{Q}^{[k]}\Delta W^{[k]}, \tag{4.61}$$

where k indexes coupling operators. However, the structure of the LHS is more complicated. The approach taken in this research is to explicitly compute and invert this matrix. Defining $\mathbb{P}$ the matrix premultiplying $\Delta\mathcal{X}$, the updates are then found as

$$\Delta\mathcal{X} = \mathbb{P}^{-1}\left(\mathcal{H}\Delta t - \sum_k \mathcal{Q}^{[k]}\Delta W^{[k]}\right). \tag{4.62}$$

In the following I describe how this can be combined with the 'sweeping' algorithm for updating via the time-dependent variational principle as described in Chapter 2.

3.2.2 Algorithm for finding friction update to MPS

In the closed-system time dependent variational principle equations for matrix product states, the state can be updated one site at a time. This can be combined with

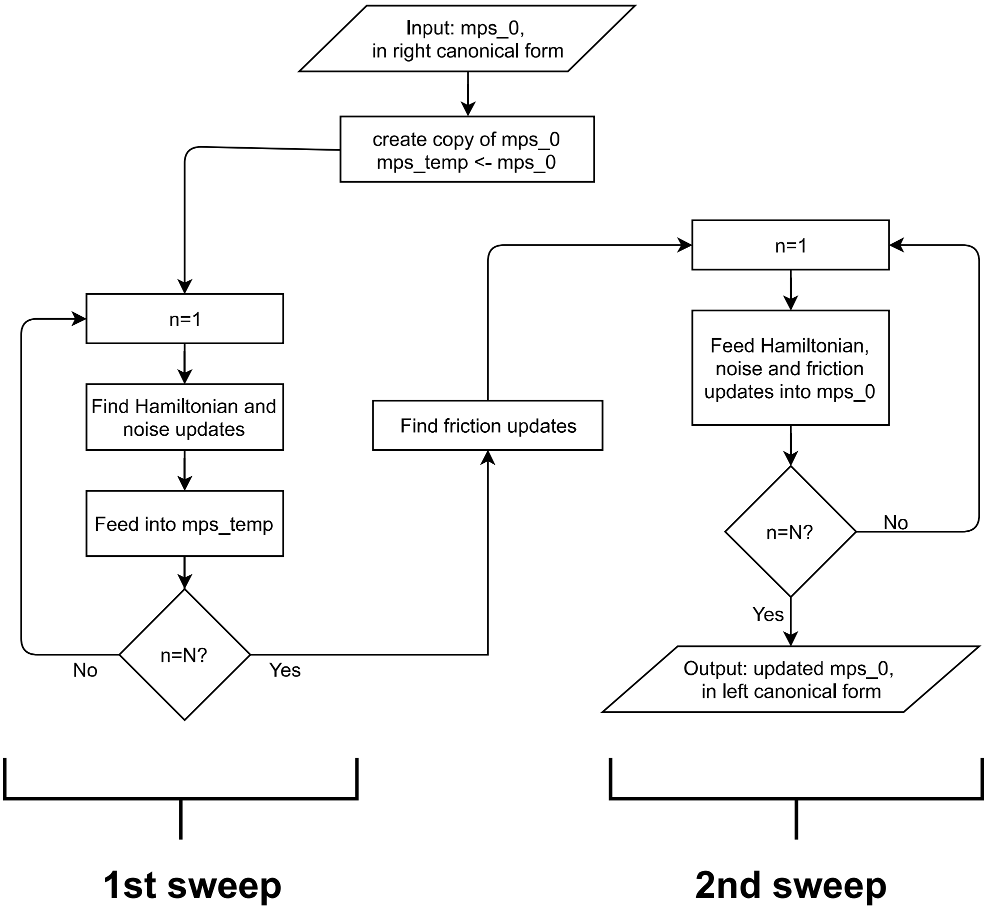

Figure 4.2: *Flowchart describing in-sweep update algorithm for matrix product state Langevin equation, starting in right canonical form.* The update takes the form of two sweeps, the first used to calculate the frictionless updates. After this the frictional updates are found, as descibed in the main text. Finally a new sweep is performed, on a new copy of the input state, feeding in the frictional updates.

a gauge-transforming sweep through the matrix product state, updating each site in the central gauge, and avoiding the inversion of Schmidt coefficients [64]. Friction however couples the updates on different sites, as discussed above. Here I describe a sweep-based algorithm for updating a matrix product state according to the Langevin equation.

Starting with Eq 4.62, the first step is to sweep through the system finding the components $\vec{h}$ and $\{\vec{q}^{[k]}\}$ of the frictionless update. For this algorithm to be consistent, the state is updated with just the Hamiltonian and noise terms during this sweep. The resulting state is then thrown away, while $\vec{h}$ and $\{q^{[k]}\}$ are used to form the frictionless updates ΔX_0 and the matrix $\mathbb{P}$. Next, the frictional updates are found by numerically solving the linear problem $\mathbb{P}\Delta\mathcal{X} = \Delta\mathcal{X}_0$ for $\Delta\mathcal{X}$. This can be done using any numerical linear solver; here I used the built-in MATLAB functions. Finally, the sweep starts again with the original state, this time simply feeding in the updates $\Delta\mathcal{X}$. This algorithm is summarized in flowchart form in Fig 4.2.

The code written for this research follows this algorithm to find the frictional

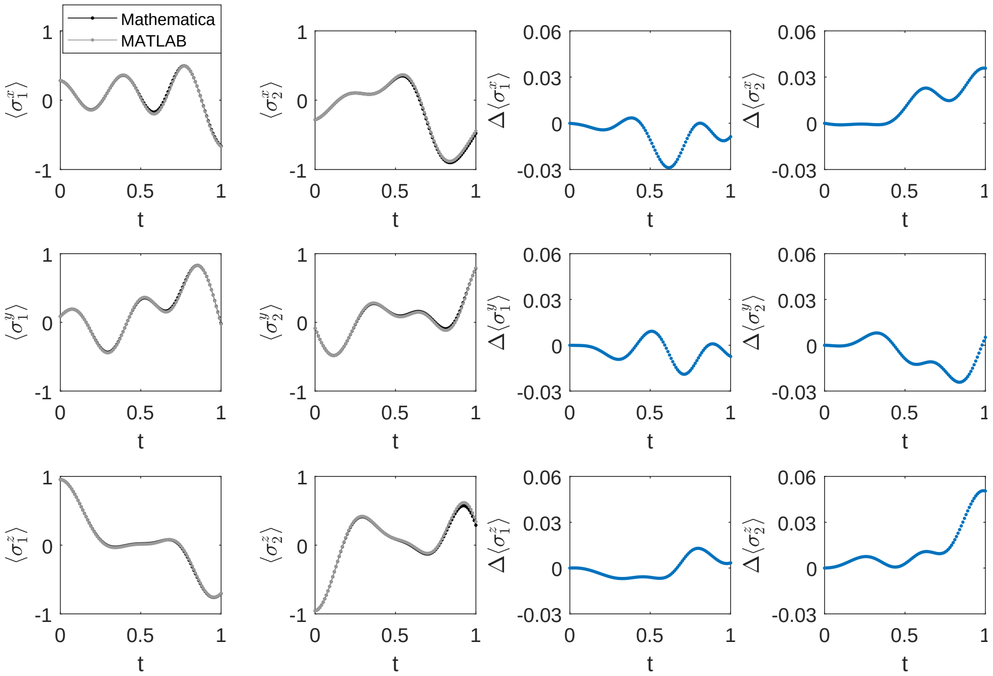

Figure 4.3: *Verifying friction update for matrix product states against independent implementation in Mathematica.* Left two columns: expectations of Pauli operators for first and second spin for both MATLAB and Mathematica results. Right two columns: differences between these expectations are small, providing a check of the MATLAB code.

update. This was verified by comparing it with a separate implementation, for a particular two-spin problem that can be manipulated into a closed form, and is integrated using Wolfram Mathematica. The details of the model and the Mathematica implementation are found in Appendix B. Fig. 4.3 shows the results of this check, showing that the quite different matrix product state implementation of the Langevin equation matches the alternative formulation. Checks of larger systems can be made by embedding the two interacting systems, and doing this shows agreement also.

3.2.3 Imposing locality

The numerical difficulty in evaluating the friction term comes from the fact that it couples each site's update to every other site. This arises from factors like $d\langle\hat{F}\rangle/dt = \langle\psi|\hat{F}|\partial_t\psi\rangle + c.c.$ appearing in the update of a single site. The state derivative $|\partial_t\psi\rangle = \sum_i |\partial_{X_j}\delta\psi\rangle\dot{X}_j$ depends on updates on all of the sites. However if the entanglement in the state is local, then the inter-site frictional coupling is less important. Essentially this long-range coupling arises because the tensors A of the matrix product state encode long-range entanglement in general. However when entanglement is small, the coupling will be short-ranged.

This can be seen by considering the off-diagonal parts of the quadrants of $\mathbb{P}$. These contain terms in $\vec{q}^\dagger\vec{q}$, $\vec{q}^\dagger\vec{q}^*$ and the complex conjugates thereof. Assume that the coupling operators are local, so that $\hat{F}^{[k]}$ acts only on the site n_k corresponding to k. Assume also that the elements of $\vec{X}$ are organized so that the updates relating to the first site come first, then the second, and so on. Then the off-diagonals of the quadrants of $\mathbb{P}$ are proportional to those elements of $\vec{q}^{[j]}$ that determine the update on sites $\neq n_j$ due to the coupling on site n_j. For example, elements in the top-left quadrant of $\mathbb{P}$ are given by

$$\mathbb{P}_{j,l}^{(top\text{-}left)} = \delta_{j,l} - \sum_k \gamma^{[k]} \langle \partial_{X_j^*} \delta\psi | \hat{F}^{[k]} | \psi \rangle \langle \psi | \hat{F}^{[k]} | \partial_{X_l} \delta\psi \rangle, \tag{4.63}$$

where k indexes coupling operators, and $\delta_{j,l}$ is the Kronecker delta. These elements couple sites n_j and n_l. The distance of such an element from the diagonal of the quadrant it sits in reflects the distance between sites: $|n_j - n_k|$.

Working in the left-gauge tangent basis, the contribution is zero unless $n_k > \min(n_j, n_l)$. Therefore the terms in 4.63 involve coupling sites a distance $n_j - n_k$ away (for the first factor) and sites a distance $n_l - n_k$ away (second factor). Each term involves at least one factor coupling sites a distance $|n_j - n_l|$ apart. A similar analysis holds for each of the other quadrants of $\mathbb{P}$. Furthermore, it is a property of matrix product states[1] that any correlations decay exponentially with distance between sites[62]. Therefore, the distance of an element of $\mathbb{P}$ from its quadrant's diagonal is equal to the (minimum) coupling distance that element represents. For a finitely correlated state such terms decay with coupling distance. So we can reduce the number of non-zero elements of $\mathbb{P}$ by assuming a degree of locality in the matrix product state.

In practice this can be achieved by deciding on a maximum friction correlation width w_F - so that $-i\langle \partial_{X_j^*} \delta\psi | \hat{F}^{[k]} | \psi \rangle$ is taken to be zero if $|n_j - n_l| \leq w_F$. This produces a $\mathbb{P}$ with fewer non-zero elements, which can be stored as a sparse matrix with a higher degree of sparsity. Numerical techniques that are optimized for sparse matrices can then be used for solving the linear system of equations $\mathbb{P}\Delta\mathcal{X} = \Delta\mathcal{X}_0$. In MATLAB the `mldivide` function is pre-optimized for this.

The effects of limiting w_F are explored further in Chapter 5. This truncation dramatically reduces the number of elements of $\mathbb{P}$ that need to be calculated and realizes an assumption of locality in the frictional cooling.

Having shown how the Langevin equation for matrix product states can be evaluated numerically, we now proceed to a summary discussion of the usefulness and limitations of this approach, and how it compares with other techniques.

---

[1] Strictly this is the case for matrix product states describing infinite systems, however finite matrix product states behave in a similar fashion. For example if a state is separable at any cut, the parts of the system either side of the cut are not correlated with one another.

4 Discussion

In this chapter I have presented a Langevin equation for matrix product states in thermal contact with oscillator baths. This has been derived using a Keldysh path integral formulation, following the approach in [119], and constructed over matrix product states following the formalism of [65]. The resulting equation adds two sorts of terms to the time-dependent variational principle equations for Hamiltonian dynamics, corresponding to dissipative friction and noisy fluctuations. These are related by a temperature-dependent fluctuation dissipation relation through the second moments of the noise fields underlying the fluctuating terms. For this research code was written in MATLAB to integrate the Langevin equation forwards. I have explained how I have extended the algorithms in the literature for the time-dependent variational principle to handle the friction and noise terms. The code has been tested for strong convergence of noisy trajectories, and the frictional part has been checked against an separate implementation for a particular problem.

The matrix product state Langevin equation combines the features of both Langevin equations and matrix product state parameterizations. Langevin methods are advantageous because they give prescriptions for finding stochastic trajectories of pure states, and separate the frictional drift and noisy fluctuation effects of the environment in a tunable way. Matrix product states can describe spin chains/multi-qubit systems to varying degrees of approximation, by tuning the bond dimension of the parameterization. In effect this provides three degrees of freedom to explore open quantum system effects with: the temperature of the baths, the coupling strength (via the friction prefactors γ), and the bond dimension of the matrix product state. This allows larger systems of fixed bond dimension entanglement to be investigated, and invites study into when the environment might restrict the system to a manifold of fixed bond dimension matrix product states.

Chapter 5

Applications of Langevin equation for MPS

A Langevin equation over matrix product states may be used to study a variety of physics. In this chapter I present three studies.

First I discuss using the frictional effect to drive a system to its ground states, and applications to numerical ground state finding.

Next is a study of sampling the thermal distribution of a system and bath in equilibrium. While a quantum Langevin equation will find incorrect thermal averages - it gives a classical thermal distribution over the restricted state space - this error decreases with increasing system size. The matrix product state Langevin equation may therefore be used as a tool for sampling such distributions in systems where this error is expected to be small and exact analysis is impossible.

Finally I investigate how the environmental interaction restricts the entanglement in a system. I study the process of generating entanglement in an initially unentangled state using a static Hamiltonian, and how noise and friction impede this.

The work in this chapter is original and in preparation for publication.

1 Real-time frictional cooling to the ground state

An important limit of the long-time equilibriation with a thermal bath occurs when the bath is at zero temperature. In this case, the system will equilibriate with its environment by settling near to its ground state. In the Langevin formulation, we can go further and completely turn off the noise term.

1.1 Ground state finding for quantum spin chains

Numerical techniques for ground state finding are a key tool in studying the physics of interacting many-body quantum systems [36]. In strongly correlated condensed matter systems, knowledge of the low-energy eigenstates can be used to study static and dynamical properties [152], even at finite temperatures [153]. Sophisticated experimental techniques can simulate the Hamiltonians of such systems with highly tuneable interactions [154] and readout of individual particles [155], make for a rich testbed for joint experimental and theoretical development, in which ground state finding plays a key role.

Matrix product states are well-suited to numerical ground state finding when these states have a degree of locality. In this case they can be well-described with matrix product states of fixed bond dimension. It can be proven that local Hamiltonians of one-dimensional systems that have a gap between their ground state and first excited states exhibit area-law entanglement in their low energy states[62].

The most established matrix product state methods for ground state finding in strongly correlated quantum spin chains are the density-matrix renormalization group (DMRG) techniques, developed by White in 1992 [53]. An alternative method for ground state finding with matrix product states is imaginary-time evolved block decimation (iTEBD). This adapts real-time evolution in the TEBD algorithm. TEBD works for a Hamiltonian with only local and nearest-neighbour terms by splitting the time-evolution operator $e^{-\hat{H}t}$ via a Suzuki-Trotter decomposition. By grouping the terms that act on alternating pairs of sites, the time update can be made locally, resulting in an efficient evolution algorithm [156, 64].

Here I present a complementary scheme for ground state finding with matrix product states. By taking the friction-only limit of the Langevin equation, a real-time evolution that drives the system to its ground state can be found. This mimics the physical process of cooling the system with a zero-temperature bath, while neglecting zero-point fluctuations entirely.

1.2 Langevin cooling to ground state with MPS

The ground state of a system described by matrix product states can be found using the Langevin equation discussed in the previous chapter. Taking the temperature of the system's environment to zero, the Langevin equation reads:

$$i \sum_{\beta} \langle \partial_{\bar{A}^{\alpha}} \psi | \partial_{A^{\beta}} \psi \rangle \dot{A}^{\beta} = \langle \partial_{\bar{A}^{\alpha}} \psi | \hat{\mathcal{H}} | \psi \rangle + \sum_{k} \gamma_k \frac{d \langle \hat{F}_k \rangle}{dt} \langle \partial_{\bar{A}^{\alpha}} \psi | \hat{F}_k | \psi \rangle. \tag{5.1}$$

This can be integrated numerically using the methods described in chapter 4.

Fig 5.1 shows this in action for a system of 6 spins with an Ising Hamiltonian

$$\hat{H} = -J \left(\sum_{n=1}^{5} \hat{S}_z^n \hat{S}_z^{n+1} + \sum_{n=1}^{6} g \hat{S}_x^n \right), \tag{5.2}$$

where $\hat{S}_x^n$ and $\hat{S}_z^n$ are the x- and z- spin operators on the nth spin, $J = 1$ and $g = 0.5$. Initially the spins are all aligned in the $z-$direction, $|\psi_{\text{init}}\rangle = |\uparrow_z\rangle^{\otimes 6}$. The system is modelled by the matrix product state Langevin equation, in which the spins are each coupled isotropically to environments, ie. the coupling operators are $\{\hat{F}\} = \{\hat{S}_x^n, \hat{S}_y^n, \hat{S}_z^n\}$. The temperature of the environment is taken to be zero, and the friction rate $\gamma > 0$. The system is sufficiently small that in this case exact diagonalization can be used to find the ground state of the Hamiltonian.

The first interesting thing to note is that higher friction rates don't necessarily perform better. As shown in the top two plots of Fig 5.1, values of γ that are too low or too high exhibit under- and over-damping behaviours respectively. For these results a near-critical value of $\gamma = 2$ was found by running for a short time at a range of values γ and identifying which friction rates led to most rapid decrease in energy.

The entanglement between the left and right halves of the chain is shown at the top of Fig 5.1. This is the contiguous bipartitioning with the maximum potential for entanglement entropy, with a maximum value of $\log_2 2^3 = 3$. It is thus a good indication of how far the bond dimension of the matrix product state may be truncated before errors are significant. In this case the ground state has fairly low entanglement, and the initial state is entirely separable. This guides the critically damped and overdamped simulations towards states of low entanglement. However the underdamped simulation sees a significant ramping up of entanglement. These results suggest provided the initial and ground states are sufficiently low in entanglement, and a near-critical value of friction γ is used, low bond dimension matrix product states may provide an efficient route to finding the ground state.

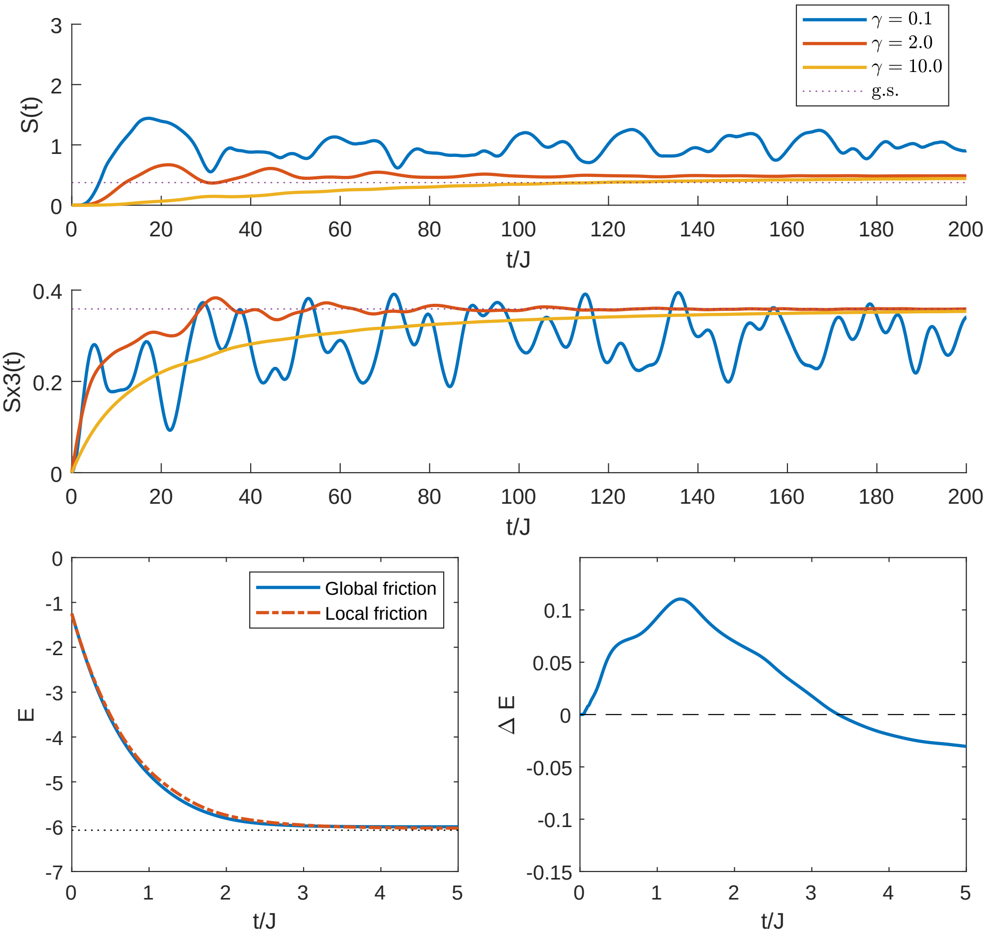

Figure 5.1: *Frictional cooling to the ground state for a 6-spin Ising chain.* Top and middle: evolution of entropy $S(t)$ and a local operator $\langle \hat{S}_x^{[3]} \rangle$ during cooling with low $\gamma = 0.1$, near-critical $\gamma = 2$ and high $\gamma = 10$ friction strengths. These reveal underdamping, critical damping and overdamping characteristics in the cooling. Bottom: the effect of imposing locality on the simulated Langevin cooling at $\gamma = 2$ for untruncated 'global' friction, and restriction to on-site friction effects only. The right plot shows $\Delta E = E_{\text{Local}} - E_{\text{Global}}$.

1.2.1 Imposing locality

One issue with applying the matrix product state Langevin equation to find ground states via frictional cooling is the non-locality of the friction term. Using the methods described in chapter 4 requires solving a system of equations relating all of the tensors to one another. However this can be made more efficient if we impose a locality condition on the friction. This can be justified by noting that the terms coupling different spins are proportional to the transfer matrix between those spins - if two spins aren't very entangled, they won't feel one another's frictional effects so much. However if our goal is simply to find the ground state then we need no justification, as long as the method is successful.

The bottom row of plots in Fig 5.1 shows the effect of imposing locality on the ground state energy of the 6-spin Ising chain. Shown are results for completely local frictional coupling, in which each spin only sees its own contribution to the friction, and an untruncated global coupling. The truncation to local friction has a remarkably small effect on the reduction in energy. At later times, it even drives the system to lower energies than the globally coupled case.

In this section we have discussed friction dominated dynamics, where the temperature of the environment is negligible. The real-time evolution to the ground state from the Langevin equation may provide a complementary technique for ground-state finding. While the frictional term in the Langevin equation is problematic in general, the preliminary results presented here suggest that truncating the length scale of the frictional effect on one spin due to another can work well.

This technique – working in the friction dominated limit as a tool for finding ground states – could be developed further to increase its usefulness. In particular, it would be interesting to explore how well the method could be extended to the time-dependent variational principle for infinite spin chains, in the case of entirely local friction. This could be achieved by replacing the $d\langle\hat{F}\rangle/dt$ factor by $N\langle\psi|\hat{F}|\partial_{\bar{A}}\psi\rangle\dot{A} +$ *c.c.*, where N is the length of the chain and cancels out as explained in chapter 4, and A defines the matrix product states. The resulting linear system $\dot{A} = \dot{A}(A, \dot{A})$ can be straightforwardly solved at each timestep. The result would be an approximation for frictional cooling of the system, and may prove to be a useful numerical tool for ground state calculations.

2 Sampling of the thermal distribution

In this section we use Langevin dynamics to sample matrix product states from a thermal distribution, by allowing the system to equilibriate with the bath in the long-time limit. For small systems, Langevin dynamics will find incorrect thermal values, however the error gets smaller with increasing system size. For a single spin-1/2 there are two energy eigenstates and a Langevin average will sample continuously over the Bloch sphere. However for N spins there are 2^N states, and sampling continuously over a matrix product state manifold is a better approximation. We study this thermalization and the resulting distribution by comparing observables to those found in true thermodynamic equilibrium, and in the Langevin limit.

2.1 Techniques for sampling thermal distributions

Many aspects of many body quantum systems can be revealed by studying thermal distributions of their states. Thermal properties such as heat capacities, correlation functions, and susceptibilities can be extracted from the partition function; a trace over the Gibbs thermal state of the system. Sampling thermal distributions are envisioned to be an application of quantum computers [157].

The full Gibbs state $\hat{\rho} = \exp(-\beta \hat{H})$ for inverse temperature β is intractable for all but the smallest systems or the most simple Hamiltonians. Thermal expectations can however be approximated with stochastic trajectories. The most common approach is to use Monte-Carlo methods.

It is also possible to sample the thermal distribution using Langevin equations. After a sufficiently long period of time, a system in thermal contact with a bath at temperature T will reach thermal equilibrium. This scenario is naturally modelled by the Langevin equation: thermal equilibrium will be reached by a balance between the dissipative and fluctuating effects. However care must be taken in the sampling, as a uniformly sampled time average will not always correspond to the canonical average [158].

2.2 Results

Here we demonstrate thermal sampling using the matrix product state Langevin equation, as a proof-of-concept. First we look at a single spin under a Hamiltonian $\hat{H} = \hat{S}_z$, isotropically coupled to an environment with temperature $T = 0.1$ with friction strength $\gamma = 0.5$. The system starts in the excited state $|\psi_{\text{init}}\rangle = |\uparrow_z\rangle$.

The resulting distributions of energies are shown in Fig 5.2. We expect a systematic difference between the correct quantum average (shown in magenta) and that obtained by the coherent state Langevin modelling. These two different averages can be analyzed in this case as follows. The true thermal average of $\hat{\sigma_z} = 2\hat{\sigma}_z$ is

$$\begin{aligned}\langle \sigma^z \rangle &= \sum_\sigma \sigma e^{-\beta h \sigma} \Big/ \sum_\sigma e^{-\beta h \sigma} \qquad (5.3)\\ &= \tanh(\beta h).\end{aligned}$$

The Langevin average however results from averaging uniformly over the surface of the Bloch sphere, by integrating over the vector $\underline{n} = (\langle \sigma_x \rangle, \langle \sigma_y \rangle, \langle \sigma_z \rangle)^\intercal$:

$$\begin{aligned}\langle \sigma^z \rangle &= \int d\underline{n} \delta(\underline{n}^2 - 1) n^z e^{-\beta h n^z} \Big/ \int d\underline{n}\ \delta(\underline{n}^2 - 1) e^{-\beta h n^z} \qquad (5.4)\\ &= \frac{\int d\theta d\phi \sin\theta \cos\theta e^{-\beta h \cos\theta}}{\int d\theta d\phi \sin\theta e^{-\beta h \cos\theta}}\\ &= -\left(\coth(\beta h) - \frac{1}{\beta h}\right).\end{aligned}$$

We can interpolate between the two cases by including an even function of n_z in the integrals in Eq 5.4. These three thermal averages are plotted in Fig 5.3.

A justification for this biasing of integration can be made by returning to the path integral. The integration measure in the resolution of the identity – $\mathbb{1} = \int \mathcal{D}\underline{n} |\underline{n}\rangle\langle\underline{n}|$ for coherent states – is usually chosen to be an unbiased measure (uniform over the Bloch sphere for coherent states or Haar uniform for matrix product states). However, the resolution of the identity can be made using a biased measure. For a single spin, this bias can be chosen to be the energy eigenbasis. For many-body systems this requires knowledge *a priori* of the eigenbasis. This is clearly not possible.

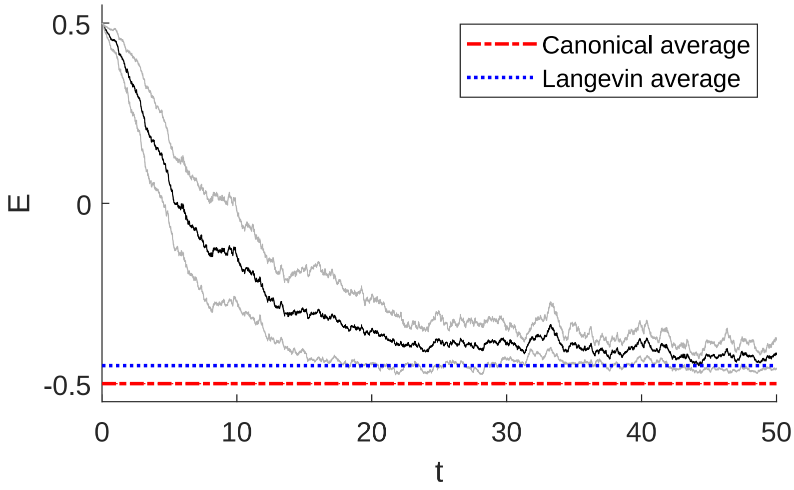

Figure 5.2: *Thermal sampling of a single spin in a magnetic field* $\hat{\mathcal{H}} = -B\hat{S}_z$*.* The spin thermalizes with its environment from initially being in the excited state $|\uparrow_z\rangle$, with $B = -1$. Modelled by the matrix product state Langevin equation, energy decays under noise and dissipation for temperature $= 0.1$ and $\gamma = 0.5$. Shown is the average over 20 trajectories (solid, black), as well as half a standard deviation either side of this (solid, gray). Horizontal lines indicate the equilibium energy in the true thermal average (dot-dashed, red) and in the Langevin average (dotted, blue) respectively.

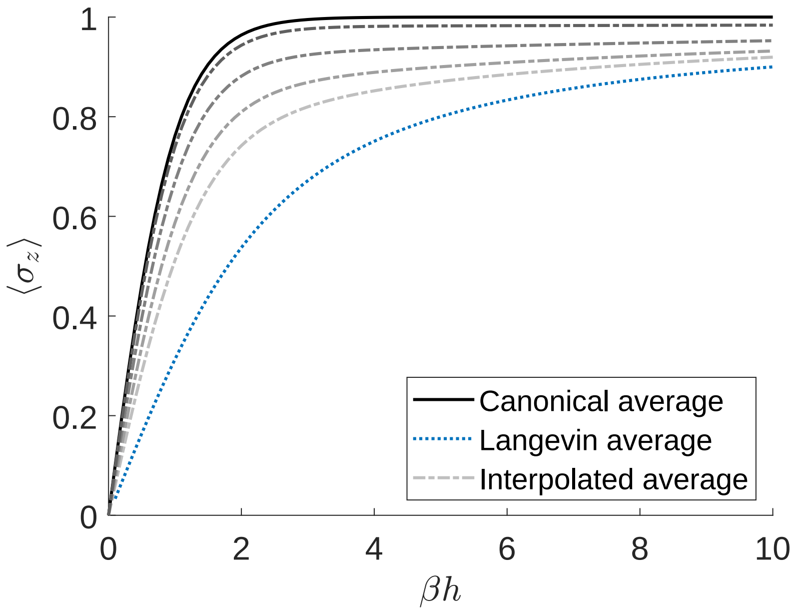

Figure 5.3: *Discrepancy between Langevin averaging and correct thermal averaging for a single spin.* Averages are shown as a function of inverse temperature β and field strength h. The canonical average over energy eigenstates is shown in the solid black line, and the Langevin average over the Bloch sphere is shown in the blue dotted line. Interpolated averages, where even powers n_z^p have been included in the integrals in Eq 5.3, are shown in gray dot-dashed lines. The values of p shown, from lightest to darkest, are $2, 4, 10$ and 50.

3 Restriction of entanglement by noise

Coupling to the environment restricts the growth of entanglement in a system by dephasing and ultimately leads to the emergence of classicality [159, 160, 161]. Growing entanglement requires a growing bond order for a faithful description. Our results show that increasing dephasing increases the time up to which a given bond-order provides a good description of the system. When friction is added, we this effect is even more pronounced.

3.1 Environmental degradation of entanglement generation

Entanglement, and entangled states, are a key resource in many quantum information processing tasks. The ability to generate entangled states is therefore important. One barrier to generating entangled states is dealing with unwanted interactions with the system's environment. While entanglement in a many body system – say a collection of qubits – is hard to quantify in general, matrix product states can prove to be a useful tool in elucidating the entanglement structure in such a system. This can be achieved by looking at the smallest bond dimension required to give a faithful description of the systems state.

A system initially in a separable state, and evolving under a quasi-local Hamiltonian, will become more entangled as time goes on. This corresponds to successively higher bond dimensions being required for a faithful matrix product state description [145]. Here we study such a process for generating quantum entanglement, in the presence of an environment as modelled by the matrix product state Langevin equation.

3.1.1 Choosing a Hamiltonian

The system consists of N spin-1/2s, or qubits. The Hamiltonian used consists of a uniform transverse field in the x-direction, and an anisotropic Heisenberg-type coupling between nearest neighbours:

$$\hat{H} = J \sum_{n=1}^{N-1} \left(\hat{S}_x^{[n]} \hat{S}_x^{[n+1]} - 1.5 \hat{S}_y^{[n]} \hat{S}_y^{[n+1]} + 0.3 \hat{S}_z^{[n]} \hat{S}_z^{[n+1]} \right) + \Delta \sum_{n=1}^{N} \hat{S}_x^{[n]}, \tag{5.5}$$

where $\hat{S}^{[n]}_{x,y,z}$ are the x, y, z spin operators for the nth site. J was taken to be -3.2 and Δ equal to 1. This Hamiltonian and these parameters were chosen as they give a dynamics that rapidly grows the entanglement in the system, while still containing only nearest-neighbour interactions.

3.1.2 Approach

The results presented in this section were generated using the code library written for this project, for a system of $N = 15$ spins/qubits. The environment was modelled using the matrix product state Langevin equation described in chapter 4. Each spin/qubit is coupled isotropically to oscillator baths, of temperature T and friction strength γ taken as uniform across the entire system. The system is initialized in a product state of positive eigenstate of $\hat{S}_z$: $|\psi_{\text{init}}\rangle = |\uparrow_z\rangle^N$.

3.2 Results

In this subsection I show i. how the closed system gradually increases in effective bond dimension, ii. the effect of the environment in a noise-only dephasing limit, and iii. the effect of increasing friction. I find dephasing noise restricts the entanglement growth rate. Friction takes the system towards its ground state and so reduces entanglement. In combination there is a limit where friction wins, limiting the amount of entanglement that can be generated.

3.2.1 Closed system dynamics

We start by examining the closed system dynamics, ie temperature $T = \gamma = 0$ for each site. Since the Hamiltonian of Eq 5.5 generates entanglement in the system, the trajectory of the system state will move away the manifold of product states. We can get a measure of this by running first at a high bond dimension, and then at successively smaller bond dimensions. By comparing the truncated trajectories it is clear when the system moves into manifolds corresponding to higher bond dimension matrix product states.

Fig 5.4 shows this for the closed system at bond dimensions $D =$ 2,4,6,8,16,32,64,128. Here $D = 128$ is sufficient to describe any state in the Hilbert space, ie. for no truncation to take place, and is used as the reference case. The trajectories are compared in two ways, i. by fidelity, $\mathcal{F} = |\langle\psi_{128}|\psi_D\rangle|$, and ii. by comparing entropy at the middle cut via $\Delta S = S_{128} - S_D$. Each of the truncated trajectories can be seen to agree well with the full description, until a certain time where the errors quickly become significant.

As expected, higher bond dimensions provide good descriptions for longer time. A simple way to characterize this is by looking for the first time that the error exceeds some threshold. In this way a time $t^*(D)$ at which the state requires a higher bond dimension can be found. This is shown for a fidelity threshold of $\mathcal{F}_{\text{thresh}} = 0.9$ and an entropy difference threshold of $\Delta S_{\text{thresh}} = 0.1$. Both curves $t^*(D)$ line up rather well, and show a monotonic increase in t^* with bond dimension, with a decreasing slope. For higher bond dimensions $64 < D < 128$ we would expect a more rapid increase in $t^*(D)$ towards $D = 128$: since a $D = 128$ matrix product state can describe a generic state, by definition $t^*(D = 128) = \infty$. If the Hamiltonian happened to keep the system in a manifold of matrix product states at some reduced bond dimension D', then we would have $t^*(D \geq D') = \infty$.

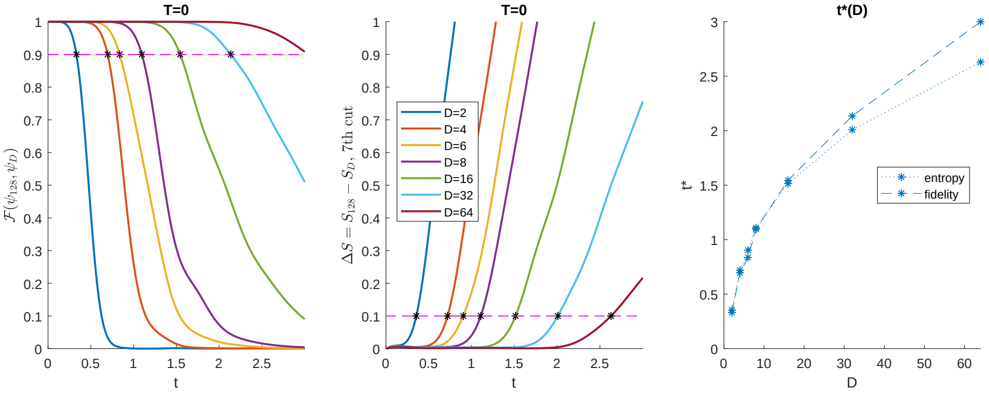

Figure 5.4: *Effective increase in bond dimension of the system state with time.* The evolution from initial state $|\uparrow_z\rangle^N$ via the Hamiltonian given in Eq 5.5 is simulated using bond dimensions $D = 2, 4, 6, 8, 16, 32, 64, 128$. Left: Fidelity $\mathcal{F} = |\langle\psi_{D=128}|\psi_D\rangle|$ as a function of time for each of the D values below the maximum of 128. Shown in the magenta dashed line is a cutoff of 0.9 fidelity agreement. Middle: Comparing entropy at the 7th cut, ie between the sites $1-7$ and $8-15$. A cutoff of 0.1 discrepancy is shown by the magenta dashed line. Right: times at which thresholds are crossed t^* as a function of bond dimension D, measured by fidelity (dashed) and entropy (dotted). This charts out the trajectories' journey into successively higher bond dimension as the Hamiltonian generates more entanglement in the system.

3.2.2 Open system dynamics

Now we have benchmarked the closed Hamiltonian dynamics, we can investigate the dephasing limit. We can do this by taking the Langevin equation in the noise-only limit: negligible friction $\gamma = 0$ but a finite value of γT. This corresponds to an infinitesimally weak coupling to a bath of very large temperature T.

Simulating noisy trajectories throws up a few practical challenges. Firstly, stochastic trajectories converge at a worse rate than their deterministic counterparts[1]. This means that smaller timesteps and hence more computational effort is required. Secondly, while a trajectory may have converged for a particular noise realization, to draw meaningful conclusions it is necessary to compare many such trajectories at a given noise strength. Fortunately the task of repeated runs of different noise realizations is straightforward to parallelize. Finally, when repeating runs at different bond dimensions, it is important to ensure that the same noise realizations are used for

---

[1] Notwithstanding higher-order numerical methods. As discussed in Chapter 4 such methods are highly non-trivial for matrix product states and not used here

each coupling - in this case three Wiener processes for each of the 15 sites.

Dephasing slows entanglement growth but does not stop it

To study the dephasing limit $T = 0, \gamma T \to$ const., trajectories were generated at a variety of bond dimensions up to 24 at values of $\gamma T = 0, 0.2, 0.5$, and 1, for 8 noise realizations each. The entropy across the central cut of the system was then calculated for each trajectory, and then averaged across trajectories of the same noise value. Fidelities with the higher bond dimension[2] calculated, and $t^*(D)$ extracted from these fidelity time series.

Fig 5.5 shows the results of this analysis. The left plot shows the entanglement $S(t)$ for bond dimension $D = 16$. The closed system $\gamma T = 0$ case shows an increase in entanglement until near the maximum value allowed by the bond dimension, $S_{\text{max}} = \log_2 16 = 4$. As the strength of dephasing is increased, the rate of entanglement growth is decreased. This effect is more pronounced for higher dephasing strengths. This is reflected in the plots of $t^*(D)$ at the different dephasing strengths: when there is more dephasing, lower bond dimension matrix product states are a better approximation for longer.

The overall effect of dephasing appears to be a general frustration of the Hamiltonian's tendency to generate entanglement in the system. However, this doesn't appear to have a significant effect on the maximum amount of entanglement that can ultimately be generated in the system. This behaviour might be expected: here the fluctuations due to the system's coupling to its environment have been modelled, however the related dissipative effect has been ignored. In effect the environment is being allowed to heat the system, eventually to an arbitrarily high temperature. The trajectories of the system state would then be expected to become ergodic ie. statistically biased towards higher entangled states. To properly account for a flow of energy back from the system to the environment, friction needs to be added.

Friction and noise above a threshold prevent entanglement growth

To study the effect of both friction and noise, bond dimension $D = 16$ trajectories were simulated at $\gamma = 10$ with noise strengths $\gamma T = 0, 0.05, 0.1, 0.2$, and 0.4. The friction was approximated as acting locally, using the methods described in chapter 4. The entropy across the 7th cut was then calculated.

Fig 5.6 shows the results of this for individual trajectories. At zero noise $\gamma T = 0$ the dissipation severely restricts the growth of entanglement, eventually decreasing

---

[2] For $\gamma T = 0$ a reference bond dimension $D = 128$ was used. For finite noises at $\gamma T = 0.2, 0.5, 1$ the reference bond dimensions were 16, 24, and 16 respectively

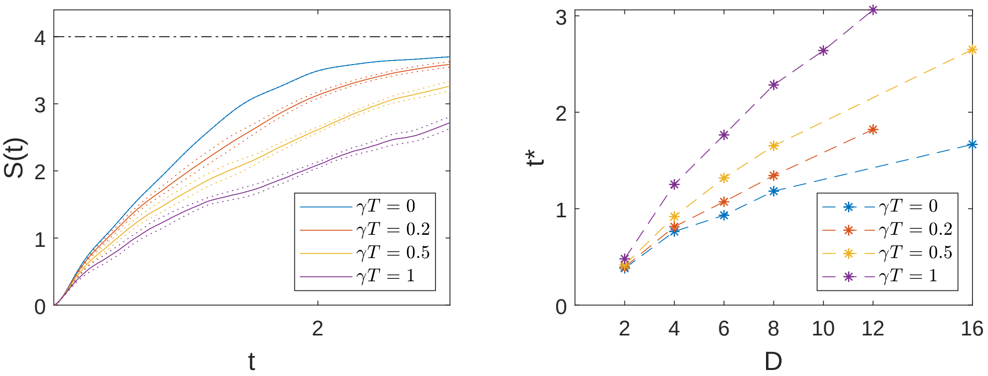

Figure 5.5: *Restriction of the growth of entanglement in the dephasing limit.* Left: Entanglement growth along the middle of the chain (7th cut) at varying values of noise strength γT at bond dimension $D = 16$. For non-zero noise the mean over 8 different noise realizations is shown, with ± half a standard deviation shown in dotted lines. The higher the noise strength, the more the growth of $S(t)$ is restricted. Right: Time $t^*(D)$ at which truncated bond dimension runs deviate from higher bond dimension reference trajectories. $t^*(D)$ is larger for higher noise strengths.

it after an initial period of growth to $S(t) \simeq 1$. This prevention of entanglement growth is also seen for the case of $\gamma T = 0.05$, where the system has trouble increasing $S(t)$ much further than about 1.2. Notably, friction in this case reverses the effect of increasing noise on entanglement growth – when there is more noise entanglement grows to larger values – suggesting that the dephasing effect of the noise frustrates the ability of dissipation to drive the system to its ground state and hence restrict the entanglement growth.

These results suggest that friction above a noise-dependent threshold prevents entanglement growth. The consequences of this would be a restriction to manifolds of MPS of lower bond dimension for longer, as the system is limited to fluctuations around a low bond dimension ground state. These results further suggest that noise frustrates the tendency of friction to drive the system to its ground state, as well as the tendency of the Hamiltonian to generate entanglement in the system.

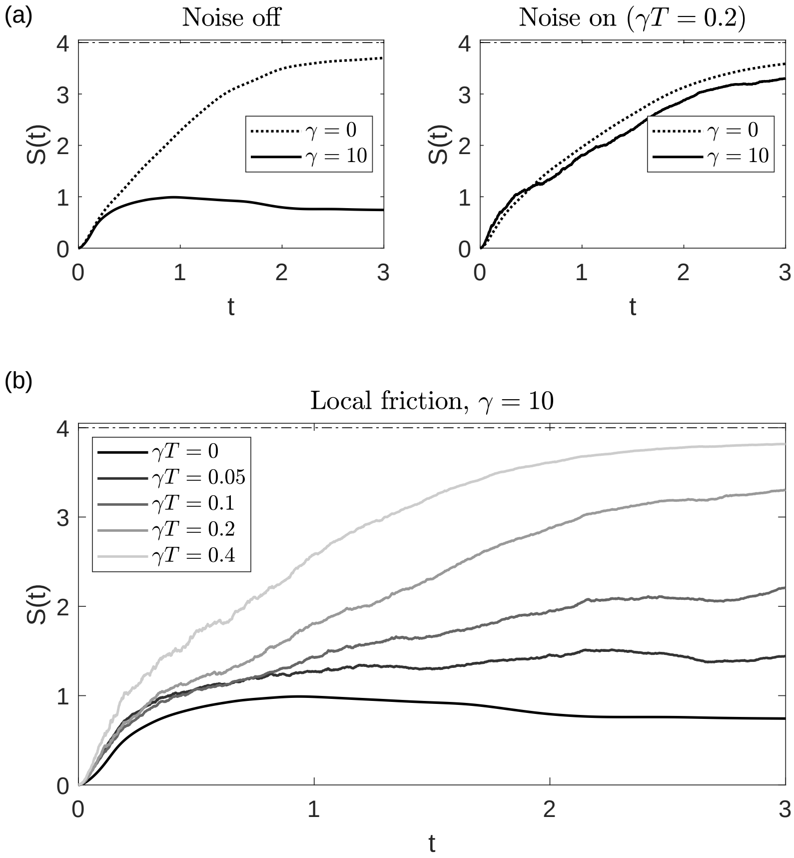

Figure 5.6: *Effect of local friction and noise on entanglement growth.* (a) Comparison of entropy growth with and without friction, in the case of zero noise, and finite noise with $\gamma T = 0.2$. The effect is much more pronounced at zero noise. The $\gamma = 10$ plots show individual trajectories with no noise averaging. (b) Frictional restriction of entanglement growth for a fixed friction strength $\gamma = 10$ and varying values of noise. Friction will act to take the system towards its ground state, decreasing its entanglement in the process. This is strongest for smaller values of noise, and for $\gamma T = 0, 0.05$ the competing effects of the Hamiltonian, noise, and dissipation balance out and entropy growth is prevented entirely.

4 Discussion

In this chapter I have presented three studies of using the matrix product state Langevin equation derived in chapter 4 to study the dynamics of many body quantum systems under the influence of noise and dissipation from their environment. If the environment is at temperature T and the strength of dissipation is γ then the associated fluctuation-dissipation relation puts the variance of the noise at γT.

The first application is to work in the dissipation-only limit $\gamma T = 0$, where the environment acts to take energy from the system and drives it to its ground state. This provides a real-time evolution to the ground state, which may prove complementary to other methods of numerical ground state finding, such as DMRG [36] or iTEBD [156, 64]. A second application is to use the noise and dissipative effects to drive the system to thermal equilibrium with its environment, so that thermal distributions of the system can be sampled. Finally, the dynamical process of generating entanglement in a spin chain was studied. The results of this suggest that in the noise-only limit, the growth of entanglement in the system is slowed down but not prevented. When dissipation is present the environment is able to draw energy from the system which therefore decreases in entanglement as it is driven towards its ground state.

These studies demonstrate the usefulness of the matrix product state Langevin equation for studying noise and dissipation in spin chains, especially when efficient matrix product states of restricted bond dimension are accurate. As well as providing new methods for ground state finding and thermal sampling, it allows finite-temperature, real-time studies of quantum dynamics.

This research is in preparation for publication. Next steps will include further work on Section 3: by simulating more frictional trajectories it will be possible to explore the effect of friction more thoroughly, in particular the effect on $t^*(D)$, shown in Fig 5.5 for the frictionless case.

Chapter 6

Hybrid approaches to quantum searching

In this chapter I present a comparative study of adiabatic and quantum walk algorithms for solving the unstructured search problem, both of which provide the optimal quantum performance. I show how an interpolation of these two approaches yields a family of hybrid search algorithms. The robustness of the hybrid algorithms to environmental effects is studied, both in the limit of an infinite temperature bath and with a Langevin equation over matrix product states.

Early parts of this work were previously submitted for a degree at University College London. The new work in this thesis consists of demonstrating quadratic speedup (section 2), extending the infinite-temperature bath analysis to a larger system, and in applying the matrix product state Langevin equation to the problem (section 3).

This work was carried out in collaboration with Nicholas Chancellor, Viv Kendon, and Sougato Bose, and is published here [162]. My contribution to the work was the study of the hybrid search algorithms as part of multiple-run search algorithms, and in the presence of both high and low-temperature baths, as well as involvement in the analysis of the scaling properties of the algorithms.

1 Quantum speedup in unstructured searching

Manipulating a smoothly-varying, time-dependent Hamiltonian in order to solve computational problems is an approach without classical analogue. However such continuous-time quantum computing schemes are a practical and realistic route to achieving a useful quantum speedup. The unstructured search problem, as studied by in a quantum context by Grover [163], is a good case study where more than one continuous-time quantum algorithm can achieve speedup over classical approaches. In this section I will discuss how the unstructured search problem may be encoded into the states of qubits. Then I will show how quadratic speedup can be achieved using the techniques of quantum walks and adiabatic quantum computation. The particular case of hypercube connectivity is considered instead of the complete graph because it is more physically realistic.

1.1 Encoding search into quantum states

The search problem can be framed in terms of the $N = 2^n$ computational basis states of an n-qubit system $\{|j\rangle\} = \{|0\rangle, |1\rangle\}^{\otimes n}$, where $\{|0\rangle, |1\rangle\}$ is the computational basis of a single qubit. We are given that one of the basis states behaves differently from the others and denote this 'marked' state by $|m\rangle$, where m is an n-digit bit string identifying one of the basis states. Because of the difference in behaviour, we can easily verify whether a given state is the marked states. One way to implement this is to offset the energy of the marked state from all the others, which can be achieved using a bias term in the Hamiltonian like $\hat{1} - |m\rangle\langle m|$. In terms of Pauli operators this can be realized by mapping jth bit of m to $q_j \in \{-1, 1\}$ according to the rule $1 \to 0$ and $-1 \to 1$ and writing

$$\hat{H}_p = \hat{\mathbb{1}} - |m\rangle\langle m| = \hat{\mathbb{1}} - \frac{1}{2^n} \prod_{k=1}^{n} (q_k \hat{\sigma}_k^z + \hat{\mathbb{1}}). \tag{6.1}$$

The search problem is then to determine which of the basis labels j corresponds to the marked state label m, given that *a priori* we have no knowledge of m, apart from it being a basis state. We can represent this ignorance of the marked state by starting with the system in a uniform superposition of all the basis states,

$$|\psi_{\text{init}}\rangle = \frac{1}{\sqrt{N}} \sum_{j=0}^{N-1} |j\rangle. \tag{6.2}$$

The search algorithms discussed here then proceed by evolving the system into a state with large overlap with the marked state, so that a measurement can be made to return the marked state label m with high probability. This is achieved by applying a (generally time-dependent) Hamiltonian to evolve the system from $|\psi_{\text{init}}\rangle$ to $|\psi_{\text{final}}\rangle$. Performing a measurement of this state in the basis $\{|j\rangle\}$ will yield the marked state label with probability $|\langle\psi_{\text{final}}|m\rangle|^2$. If $|\langle\psi_{\text{final}}|m\rangle|^2 = 1$ then the search is perfect and the problem solved. If the search is imperfect then the problem can be solved by searching multiple times: Since the result of each search is checked independently, a single successful search is sufficient. As long as $|\langle\psi_{\text{final}}|m\rangle|^2$ is greater than $1/\text{poly}(n)$ this form of amplitude amplification will be efficient. Multiple runs however will have a cost, eg. of repeated measurement and (re)initialization.

The search problem as stated here has a full permutation symmetry, up to local rotations, and as such is considered to be a toy problem from a practical point of view. A naïve implementation of Eq 6.1 requires exponentially many single-qubit terms in the Hamiltonian. However, it has recently been shown [164] that the spectrum of permutation-symmetric terms can be reproduced at the cost of n extra qubits and $\sim n^2$ extra two-qubit terms, moreover that these models may be realized perturbatively [165, 166]. While single and two-qubit terms are closer to what can be realized experimentally, an implementation would still be highly non-trivial. However the general insights gained from studying the search problem may still be applied to realistic problems of practical interest.

1.2 Quantum searching by quantum walk

A continuous-time quantum walk can be defined by considering the labels j of the n-qubit basis states $\{|j\rangle\}$ to be the labels of vertices of an undirected graph G. The edges of G can be defined through its adjacency matrix A, whose elements satisfy $A_{jk} = 1$ if an edge in G connects vertices j and k and $A_{jk} = 0$ otherwise. Since G is undirected, A is symmetric, hence it can be used to define a Hamiltonian. Although we can use the adjacency matrix A directly, it is in general more convenient mathematically to define the Hamiltonian of the quantum walk using the Laplacian $L = A - D$, where D is a diagonal matrix with entries $D_{jj} = d_j$ the degree of vertex j in the graph. We follow this convention here, but note that in this work we use regular graphs for which the degree $d_j = d$ is the same for all vertices, so that $D = d\mathbb{1}$, where $\mathbb{1}$ is the identity matrix of the same dimension as A.

The quantum walk Hamiltonian is defined as $\hat{H}_{\text{QW}} = -\gamma\hat{L}$, where $\hat{L}$ is the Laplacian operator, and γ is the hopping rate of the quantum walk. For any regular graph of degree d we thus have

$$\hat{H}_{\rm QW} = \gamma \left(d\hat{\mathbb{1}} - \sum_{jj'} A_{jj'} |j\rangle\langle j'| \right) \equiv \gamma(d\hat{\mathbb{1}} - \hat{A}). \tag{6.3}$$

The effect of $\hat{H}_{\rm QW}$ is to move amplitude between connected vertices, as specified by the non-zero entries in A. During a quantum walk, a pure state $|\psi(0)\rangle$ evolves according to the Schrödinger equation to give

$$|\psi(t)\rangle = \exp(-i\hat{H}_{\rm QW}t)|\psi(0)\rangle \tag{6.4}$$

after a time t, where units are chosen so that $\hbar = 1$.

Quantum walk dynamics can be used to solve the seach problem by lowering the energy of the marked state via $\hat{H}_p$ as given in Eq 6.1:

$$\hat{H}_{\rm QWS} = \gamma(d\hat{\mathbb{1}} - \hat{A}) + (\hat{\mathbb{1}} - |m\rangle\langle m|). \tag{6.5}$$

The net effect is to offset the energy of the marked state $|m\rangle$ against the other basis states $|j \neq m\rangle$. Applying $\hat{H}_{\rm QWS}$ to the initial state $|\psi_{\rm init}\rangle$ in Eq 6.2 induces a periodic dynamics where the overlap with the marked state oscillates. The frequency and amplitude of these oscillations depends on the hopping rate γ. Therefore γ, and the time of measurement t_f, must be chosen carefully in order to maximize the final success probability $\mathsf{P} = |\langle\psi(t_f)|m\rangle|^2$, where $|\psi(t_f)\rangle = \exp(-i\hat{H}_{\rm QWS}t_f)|\psi_{\rm init}\rangle$ is the state at time t_f.

Clearly the graph G underlying the quantum walk Hamiltonian affects how the quantum walk search performs. Most choices of graph will work, as long as the connectivity isn't too sparse of low-dimensional [167, 168]. A convenient choice, both mathematically and physically, is to use a hypercube graph. Quantum walks on a hypercube are analytically solvable [169, 170, 171], and a hypercube graph is easily implemented on a system of qubits as local bitflips.

For our system of n qubits with computational basis $\{|j\rangle\}$, the associated hypercube graph is n-dimensional, and takes these basis states as its vertices. The adjacency matrix elements $A_{jj'} = 1$ if and only if the corresponding bitstrings j and j' have a Hamming distance of one, ie are only one bitflip apart. The adjacency operator for the graph can be conveniently expressed as a uniform transverse field

$$\hat{A}^{(h)} = \sum_{k=1}^{n} \hat{\sigma}_x^{(k)}, \tag{6.6}$$

where $\hat{\sigma}_x^{(k)}$ is the Pauli-X operator applied to the kth qubit[1].

Including a factor 1/2 in γ to match Refs [167, 172, 173] and to facilitate a mapping to a symmetric subspace, a Hamiltonian for a quantum walk search on the hypercube is given by

$$\hat{H}^{(h)}_{\text{QWS}} = \frac{\gamma}{2}\left(n\hat{\mathbb{1}} - \sum_{k=1}^{n} \hat{\sigma}_x^{(k)}\right) + (\hat{\mathbb{1}} - |m\rangle\langle m|). \tag{6.7}$$

Solving the search problem using quantum walks was studied by Childs and Goldstone[167] for both the fully-connected and hypercube graphs. For each graph they found optimal values of hopping rate γ to match the quadratic quantum speedup provided by the Grover search algorithm. These optimal values are found by considering the low energy spectrum of $\hat{H}_{\text{QWS}}$. The $\gamma/2$ term has $|\psi_{\text{init}}\rangle$ as a ground state, and remaining term $(\hat{\mathbb{1}} - |m\rangle\langle m|)$ has the marked state $|m\rangle$ as a ground state. If γ is tuned so that both the ground state $|E_0\rangle$ and the first excited state $|E_1\rangle$ of the search Hamiltonian have significant overlap with $|\psi_{\text{init}}\rangle$ and $|m\rangle$, transitions between these states are induced. The greater the mutual overlaps, the higher the success probability P. The optimal point occurs near to where the gap $g = E_1 - E_0$ is smallest, and the period of the oscillations is proportional to $1/g_{\text{min}}$. The optimal value for the hypercube graph is

$$\gamma_o^{(h)} = \frac{1}{N}\sum_{r=1}^{n}\binom{n}{r}\frac{1}{r} \equiv R_1, \tag{6.8}$$

where $\binom{n}{r} = n!/(r!(n-r)!)$ is the usual binomial coefficient, and we abbreviate this quantity as R_1. We also define a related quantity R_2 as

$$R_2 \equiv \frac{1}{N}\sum_{r=1}^{n}\binom{n}{r}\frac{1}{r^2}. \tag{6.9}$$

The time taken to reach the first maximum in $|\langle\psi(t)|m\rangle|^2$ is $t_o^{(h)} \simeq (\pi/2)\sqrt{N}$, matching the quadratic speedup of Grover's original search algorithm.

1.3 Quantum searching by adiabatic dynamics

Adiabatic quantum computing (AQC), first introduced by Farhi et al. [172], works as follows. The problem of interest is encoded into an n-qubit 'problem' Hamiltonian $\hat{H}_p$ in such a way that the solution can be derived from the ground state of $\hat{H}_p$. The system is initialized in the ground state of a different Hamiltonian $\hat{H}_0$, for which this initialization is easy. The computation then proceeds by implementing a time-dependent Hamiltonian that is transformed slowly from $\hat{H}_0$ to $\hat{H}_p$. In general this adiabatic 'sweep' Hamiltonian can be parameterized in terms of a time-dependent

---

[1] ie $\hat{\sigma}_x^{(k)} = \left(\bigotimes_{r=1}^{k-1}\hat{\mathbb{1}}_2\right)\otimes\hat{\sigma}_x\otimes\left(\bigotimes_{r=k+1}^{n}\hat{\mathbb{1}}_2\right)$.

schedule function $s \in [0,1]$ as

$$\hat{H}_{\mathrm{AQC}}(s) = (1-s)\hat{H}_0 + s\hat{H}_p, \tag{6.10}$$

with $s \equiv s(t)$ such that $s(t=0) = 0$ and at the final time t_f we have $s(t = t_f) = 1$. It is useful to define a reduced time $\tau = t/t_f$, with $0 \leq \tau \leq 1$. Whereas τ is linear in t, the schedule function $s(\tau)$ - written as a function of t or τ - can be nonlinear in order to obtain a quantum speedup.

The adiabatic theorem of quantum mechanics [174] says that the system will stay in the instantaneous ground state of the time-dependent Hamiltonian $\hat{H}_{\mathrm{AQC}}(s)$ provided the following two conditions are satisfied: (i) there is at all times an energy gap $g(s) > 0$ between the instantaneous ground and first excited states, and (ii) the Hamiltonian is changed sufficiently slowly. Provided these are both true the system will be in the desired ground state of $\hat{H}_p$ at the end of the computation, thus solving the problem encoded in $\hat{H}_p$. In practice, the duration of this adiabatic sweep would be prohibitively long, so a realistic sweep will incur some probability of error. A comprehensive overview of AQC, is given by Albash and Lidar [175].

Roland and Cerf [176] describe how adiabatic quantum computing can be used to solve the search problem with a quadratic quantum speed up. Define the problem Hamiltonian as

$$\hat{H}_{\mathrm{P}} = \hat{\mathbb{1}} - |m\rangle\langle m|, \tag{6.11}$$

whose non-degenerate ground state is equal to the marked state $|m\rangle$ with eigenvalue zero. We then need to choose our easy Hamiltonian $\hat{H}_0$ such that it has $|\psi_{\mathrm{init}}\rangle$ as its non-degenerate ground state. There are many possible choices, Roland and Cerf use $\hat{H}_0 = \hat{\mathbb{1}} - |\psi_{\mathrm{init}}\rangle\langle\psi_{\mathrm{init}}|$. With the system initialized in $|\psi_{\mathrm{init}}\rangle$, the algorithm proceeds by implementing the time-dependent Hamiltonian in Eq 6.10, with a suitable schedule function $s(\tau)$, so that after a time t_f the final state of the system is close to the marked state $|m\rangle$. In this case it is necessary to use a nonlinear $s(\tau)$, whose rate of change is in proportion to the size of the gap $g(s)$ at that point in the schedule, in order to produce the quadratic speed up of Grover's search algorithm.

It is easy to show that $\hat{H}_0 = \hat{\mathbb{1}} - |\psi_{\mathrm{init}}\rangle\langle\psi_{\mathrm{init}}|$ is proportional to the adjacency operator of the fully-connected graph with $N = 2^n$ vertices. Here the hypercube graph is used, since this also has $|\psi_{\mathrm{init}}\rangle$ as its non-degenerate ground state, with Hamiltonian (in its Laplacian form) given by

$$\hat{H}_0^{(h)} = \frac{1}{2}\left(n\hat{\mathbb{1}} - \sum_{j=1}^{n}\hat{\sigma}_x^{(j)}\right) \tag{6.12}$$

where we have again included a factor of a half for mathematical convenience. This is realized by a transverse field applied to the qubit, and is a common choice for quantum annealing hardware [177]. Combining Eqs. (6.11) and (6.12), we have the adiabatic quantum computing Hamiltonian for search on a hypercube,

$$\hat{H}_{\mathrm{AQC}}^{(h)} = (1-s)\frac{1}{2}\left(n\hat{\mathbb{1}} - \sum_{j=1}^{n}\hat{\sigma}_x^{(j)}\right) + s\left(\mathbb{1} - |m\rangle\langle m|\right). \tag{6.13}$$

We note that $\hat{H}_{\mathrm{AQC}}^{(h)}$ contains the same terms as $\hat{H}_{\mathrm{QWS}}^{(h)}$ in Eq 6.7, only in different, time-varying proportions. It remains to specify the function $s(\tau)$ for the optimal performance of this Hamiltonian for searching.

1.4 Optimizing adiabatic search schedules

We have seen that QW and AQC searching may be achieved with Hamiltonians that have the same terms but different, time-varying, coefficients. Next we would like to interpolate these coefficients to generate hybrid search algorithms. However, we must first determine an optimal schedule $s(\tau)$ for the AQC search. In fact this is not entirely straightforward: it is possible to find more than one optimal schedule. In this section the method for deriving a schedule from the adiabatic condition is discussed, followed by a comparison of two such schedules, derived by analytical and a numerical approaches.

Adiabatic condition and method

A more quantitative statement of the adiabatic theorem [176, 172, 178, 179, 175] proceeds as follows: Consider a time-dependent Hamiltonian of the form in Eq 6.10, with initial and final Hamiltonians $\hat{H}_0$, $\hat{H}_\mathrm{p}$ respectively, and parameterized by the schedule function $s(\tau)$ that sweeps from $s(0) = 0$ to $s(1) = 1$ over a time t_f, the runtime of the sweep. Denote by $|E_j(t)\rangle$ the jth energy eigenstate of the Hamiltonian at time t and its energy by $E_j(t)$, where $j = 0, 1$ denotes the ground and first excited states respectively. Provided that $E_1(t) > E_0(t)$ for $t \in [0, t_f]$ and transitions to higher energy eigenstates can be ignored, the final state obeys

$$|\langle\psi(t_f)|E_0(t_f)\rangle|^2 \;\geq\; 1-\epsilon^2, \tag{6.14}$$

for small parameter $\epsilon \ll 1$, provided that at all times

$$\frac{\left|\left\langle \frac{d\hat{H}}{dt}\right\rangle_{0,1}\right|}{g^2(t)} \leq \epsilon \ll 1, \tag{6.15}$$

where the matrix element $\langle d\hat{H}/dt\rangle_{0,1}$ is given by

$$\left\langle \frac{d\hat{H}}{dt} \right\rangle_{0,1} = \left\langle E_0(t) \right| \frac{d\hat{H}}{dt} \left| E_1(t) \right\rangle \tag{6.16}$$

and the gap $g(t)$ is given by

$$g(t) = E_1(t) - E_0(t). \tag{6.17}$$

However, adiabatic protocols derived from Eq 6.15 are not always optimal. This equation accounts for probability amplitude leaking from the ground state into a nearly empty first excited state. Thus it will break down in situations where transitions to higher excited states are important, or where the population of the first excited state is significant. Eq 6.15 is therefore a two-level approximation. In the context of the search algorithms studied here, such an approximation turns out to be good for all but the smallest values of n, becoming more accurate for larger search spaces.

Equation (6.15) also does not take into account the return of probability amplitude which has already entered the excited state. Such effects can become the most relevant to the dynamics under two circumstances. If the first excited state is populated significantly, then non-adiabatic dynamics can occur such that this amplitude returns and interferes with the ground state amplitude. This is the regime which we primarily study in this work. Quantum walk dynamics are an extreme example of such behaviour as they can be viewed as time independent coherent evolution bracketed by instantaneous quenches, which are the ultimate non-adiabatic transitions. The second and more subtle case is deep in the adiabatic regime, where the Hamiltonian sweep rate is so slow that the rate of excitation formation is very low during the middle of the anneal. In these cases, boundary effects become important, which depend in a complicated way on both the nature of the annealing schedule and the total runtime [180, 181, 182][2].

Roland and Cerf [176] derive a schedule $s(\tau)$ for searching on the fully connected graph by optimizing Eq 6.15. This is done by matching the instantaneous rate of change of the schedule function $s(t)$ to the size of the gap at that time. Using

$$\left\langle \frac{d\hat{H}}{dt} \right\rangle_{0,1} = \frac{ds}{dt} \left\langle \frac{d\hat{H}}{ds} \right\rangle_{0,1} \tag{6.18}$$

---

[2] While this regime is very interesting, it is outside of the scope of this study, and not relevant for practical implementation of algorithms. For this reason, we limit our numerical studies to a maximum runtime of $\sim 5\pi/g_{\min}$, about ten times the typical runtime derived from the minimum gap. With runtimes $t_f \lesssim 5\pi/g_{\min}$, we do not observe any appreciable boundary effects in our numerical results.

in the adiabatic condition of Eq 6.15 gives

$$\left|\frac{ds}{dt}\right| \leq \epsilon \frac{g^2(t)}{\left|\left\langle \frac{d\hat{H}}{ds} \right\rangle_{0,1}\right|}. \tag{6.19}$$

The instantaneous gap $g(t)$ and $\langle d\hat{H}/ds \rangle_{0,1}$ can be calculated from the eigensystem of the Hamiltonian, which is analytically tractable for the complete graph.

Two hypercube schedules

For this study, the adiabatic condition was solved in two ways to yield two schedules: by expanding the gap around its minimum point following Roland and Cerf [176], a 'calculated' schedule $s^{(c)}$ is derived; alternatively the gap can be numerically calculated throughout the sweep to find a 'numerical' schedule $s^{(n)}$. Here I give a brief account of these two approaches. Further details can be found in Appendix C.

We are interested in the hypercube AQC search Hamiltonian given by Eq 6.13. The eigensystem of this Hamiltonian has been solved in Refs. [172, 173, 167] by mapping it to the symmetric subspace. From here the position and size of the minimum gap can be found exactly, and the eigenvalue equations expanded about this point. This is combined with the saturation of Eq 6.19 at the minimum gap point, where the RHS takes its minimum value. From the resulting expressions it is possible to derive an analytical expression for the schedule $s(t)$. The full calculation is outlined in Appendix C. The resulting optimal schedule is

$$s^{(c)}(t) = \frac{2\sqrt{R_2}}{\sqrt{N}(1+R_1)^2} \tan\left\{ \frac{8\epsilon\sqrt{R_2}R_1^2 t}{n\sqrt{N}R_2^2} - c \right\} + \frac{1}{1+R_1}, \tag{6.20}$$

where terms up to $O(1/N)$ have been dropped,

$$c = \arctan\left\{ \frac{(1+R_1)\sqrt{N}}{2\sqrt{R_2}} \right\}, \tag{6.21}$$

the constant R_1 is defined in Eq 6.8 and R_2 by

$$R_2 \equiv \frac{1}{N}\sum_{r=1}^{n} \binom{n}{r} \frac{1}{r^2}. \tag{6.22}$$

This analytical schedule is guaranteed to satisfy Eq 6.19 only in the region of the minimum gap, however it is here that transitions to unwanted higher energy levels are most rapid, so the net effect is that this schedule still manages to produce optimal

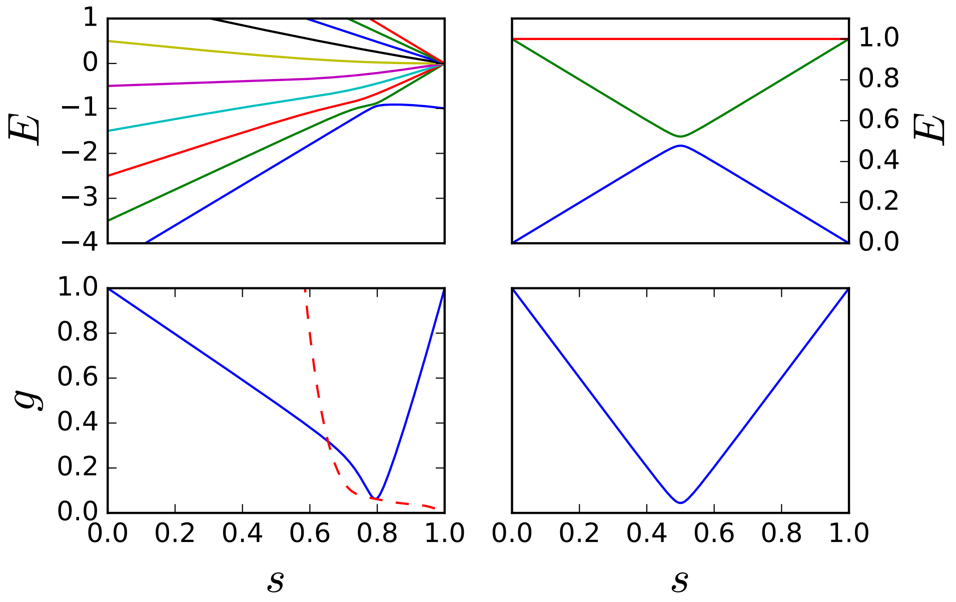

Figure 6.1: *Energy eigenstates of hypercube search Hamiltonian.* (Top) Energy levels and (bottom) gap for a hypercube of size $n = 9$ (left) and complete graph (right). Both the true gap (blue, solid) and the approximate, analytical, gap (red, dashed) are shown for the hypercube (bottom left). The analytical gap is only accurate near the true minimum gap, however it is here that transitions to higher energy levels are most rapid, so the resulting analytical schedule still yields optimal quantum speedup. Energy units defined by Eq 6.13.

quantum speedup. For $N \gg 1$, the runtime is given by

$$\epsilon\, t_f^{(c)} \simeq \frac{\pi\sqrt{N}}{4}, \tag{6.23}$$

where the approximation of the arctans by $\pi/2$ becomes exact as $N \to \infty$. Note that choosing a value for ϵ – the accuracy with which the system stays in the ground state, see Eq 6.14 – determines the corresponding runtime t_f, and vice versa. For our numerical calculations we have chosen to specify t_f, since this enables direct comparisons with QW searching to be made. The energy levels of $\hat{H}^{(h)}_{\mathrm{AQC}}$ are shown in Fig. 6.1 (top left) for $n = 9$, and for comparison the energy levels of the search Hamiltonian for the complete graph (which is the same for any size) are shown top right.

We also solve Eq 6.15 numerically to obtain $s^{(n)}$ using an explicit numerical calculation of the gap $g(t)$, and using the maximum value of $\langle d\hat{H}^{(h)}_{\mathrm{AQC}}/dt\rangle_{0,1}$, which is shown in Appendix C to be $n/4$. Our numerical algorithm is also described in Appendix C. While it does not provide a closed form solution, results using $s^{(n)}$ do provide insight on the accuracy of $s^{(c)}$. Provided the numerics are performed to a sufficient accuracy, $s^{(n)}$ will always provide an optimal $\sqrt{N}$ speed up. The analytically and numerically calculated gaps are plotted in the bottom left of Fig. 6.1 for $n = 9$, and the corresponding gap for the complete graph is shown bottom right. For the hypercube, the analytical and numerical gaps are strikingly different, yet both produce schedules that obtain a quantum speed up. As we will see, this is because for the quantum search problem only the position and size of the gap are important. Elsewhere, the transition probabilities are so small it does not matter how fast the schedule proceeds.

Both of these schedules assume a two-level approximation, as they start from Eq 6.15. While for small system sizes the higher energy levels do affect the performance, for large N this is a good approximation.

2 Hybrid adiabatic and quantum walk searching

Having seen the similarities between quantum walk and adiabatic searching on the hypercube, in this section we show how they may be interpolated to find hybrid approaches to searching. Then we see how the hybrid searches may be shown to provide the full quadratic quantum speedup. Finally their performance is compared, in terms of single searches and also multiple search protocols. The latter is important in cases where possible solutions can be checked quickly, and the results depend on the time taken for initialization and readout.

2.1 Hybrid searching

We have already noted that QW and AQC search algorithms both use the same terms in the Hamiltonian, differing only in the time dependence. With appropriate choice of parameters, both provide a quadratic quantum speed up: a search time proportional to $\sqrt{N}$ for a search space of size N. This suggests the question of whether we can map smoothly between QW and AQC searching, while maintaining the quantum speed up.

To construct the mapping, we generalize the AQC Hamiltonian of Eq 6.10 by defining a time-dependent Hamiltonian

$$\hat{H}(\tau) = A(\tau)\hat{H}_0 + B(\tau)\hat{H}_p \tag{6.24}$$

as a function of the reduced time $\tau = t/t_f$, where the annealing schedules $A(\tau)$, $B(\tau)$ satisfy $A(0) \gg B(0)$ and $B(1) \gg A(1)$. The AQC algorithm as described by Eq 6.10 is obtained by setting

$$A_{\mathrm{AQC}}(\tau) = 1 - s(\tau), \qquad B_{\mathrm{AQC}}(\tau) = s(\tau). \tag{6.25}$$

The QW search Hamiltonian with hopping rate γ, described by Eq (6.5), can also be obtained by setting

$$A_{\mathrm{QW}}^{(\gamma)}(\tau) = \begin{cases} \gamma & \tau < 1 \\ 0 & \tau = 1 \end{cases}, \qquad B_{\mathrm{QW}}^{(\gamma)}(\tau) = \begin{cases} 1 & \tau > 0 \\ 0 & \tau = 0. \end{cases} \tag{6.26}$$

We can make this even closer to the AQC form by defining $\beta = 1/(1+\gamma)$ and setting

$$A_{\mathrm{QW}}(\tau) = \begin{cases} 1-\beta & \tau < 1 \\ 0 & \tau = 1 \end{cases}, \qquad B_{\mathrm{QW}}(\tau) = \begin{cases} \beta & \tau > 0 \\ 0 & \tau = 0. \end{cases} \tag{6.27}$$

For QW search on the hypercube, using Eq 6.8 for $\gamma_o^{(h)}$, to achieve optimal $\sqrt{N}$ scaling we must set β equal to

$$\beta_o^{(h)} = \frac{1}{1 + R_1}. \tag{6.28}$$

For $0 < \tau < 1$, the re-parameterization of Eq 6.26 in Eq 6.27 maintains the ratio of $A_{\mathrm{QW}}(\tau)/B_{\mathrm{QW}}(\tau) = \gamma$. However, it also introduces a global energy rescaling $A_{\mathrm{QW}}(\tau) = \beta A_{\mathrm{QW}}^{(\gamma)}(\tau)$ and $B_{\mathrm{QW}}(\tau) = \beta B_{\mathrm{QW}}^{(\gamma)}(\tau)$[3].

In the way we have parameterized them above, the AQC and QW protocols differ only in the annealing schedules $A(\tau)$ and $B(\tau)$. Hence, we can use the QW and AQC schedules as end-points of a smooth interpolation between these two search algorithms to define a continuum of hybrid protocols. Using a parameter $\alpha \in [0, 1]$, where $\alpha = 0$ corresponds to QW and $\alpha = 1$ corresponds to AQC, we can define

$$A(\alpha, \beta, \tau) = \frac{1 - s(\tau)}{\alpha + (1 - \alpha)\frac{(1 - s(\tau))}{(1 - \beta)}}, \qquad B(\alpha, \beta, \tau) \quad = \frac{s(\tau)}{\alpha + (1 - \alpha)\frac{s(\tau)}{\beta}}. \tag{6.29}$$

giving a family of hybrid quantum algorithms defined by the Hamiltonian

$$\hat{H}_{\mathrm{AB}} = A(\alpha, \beta, \tau)\hat{H}_0 + B(\alpha, \beta, \tau)\hat{H}_p. \tag{6.30}$$

This interpolation is quite general, for well-behaved $\hat{H}_0$ and $\hat{H}_p$, with the caveat about the extra dependence of the energy scale on the QW hopping rate through β mentioned above. The nature of this interpolation functions is illustrated in Fig. 6.2 for a search over a 5- qubit hypercube graphs.

Note that, although it is plausible, it doesn't follow *a priori* from the construction that these interpolated AQC-QW schedules will yield a quantum speed up at all for searching, let alone an optimal $\sqrt{N}$ scaling. This is because the different mechanisms in QW and AQC could be incompatible in combination. We return to this important question in Sec. 2.2, where we show that properly specified interpolations can indeed achieve the theoretical optimum $\sqrt{N}$ scaling.

Small system examples

To gain intuition for how our interpolated schedules behave, we can look at a small systems of five qubits. These have been simulated using the full Hamiltonian on the hypercube; for numerical methods, see Appendix D. Fig. 6.2 shows how the final success probability varies with the search duration t_f for QW, AQC and an intermediate

---

[3] Note that the since the optimal $\gamma_o^{(h)}$ is dependent on the size of the system, this re-parameterization introduces a weak dependence of the global energy scale on system size $N = 2^n$. However, since $\beta_o^{(h)} \to 1$ in the large N limit, this weak dependence cannot affect the leading order term in the asymptotic scaling, and the re-parameterized quantum walk search algorithm still provides optimal $\sqrt{N}$ scaling.

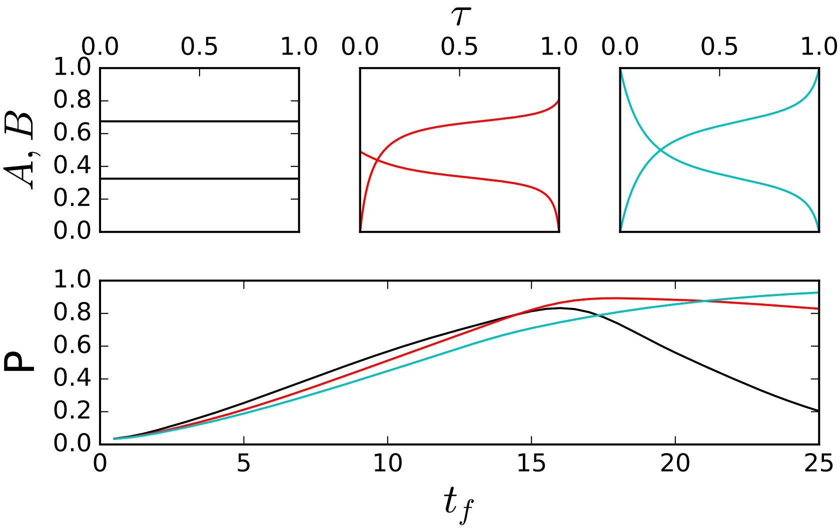

Figure 6.2: *Comparison of QW, AQC and hybrid search dynamics.* (Top) Numerically calculated hybrid schedules A and B against runtime τ for quantum search on a 5-qubit hypercube graph for $\alpha = 0$ QW, (black, top left), $\alpha = 0.5$ (red, mid gray in print, top middle), and $\alpha = 1$ AQC, (cyan, light gray in print, top right). (Bottom) Success probability of the corresponding searches (indicated by matching colour/shade of gray in print) against total search time t_f, in units given by Eq 6.24. Note that this does not show time evolution against t or τ.

$\alpha = 0.5$ search over the 5-qubit hypercube graph. Note that, because the schedules A and B are in general nonlinear functions of time, in all plots against t_f each point represents a separate run of the quantum search algorithm for that value of t_f; the plots do not also represent the time evolution $0 \leq t \leq t_f$, except for $\alpha = 0$ when the schedule functions are constant. Also plotted in Fig. 6.2 are the annealing schedules A and B as a function of the reduced time τ, illustrating how the shape of the functions $A(\alpha, \tau)$ and $B(\alpha, \tau)$ changes for different values of α, from flat for a quantum walk to a curving AQC annealing schedule for $\alpha = 1$.

We see that the qualitative behaviour of adiabatic evolution is fundamentally different from that of the quantum walk search. For the optimal AQC schedule the success probability increases monotonically to a value very close to one. In contrast, QW shows oscillatory behaviour, and although the success probability does not approach one, it does show a faster initial increase than for AQC. The intermediate schedule shows a mix of both behaviours, with a locally oscillating but globally increasing success probability that shows an initial increase rate between that of QW and AQC.

2.2 Demonstrating quadratic speedup with single runs

Our strategy for analyzing the scaling of the hybrid quantum search algorithms is to show that the performance is dominated by a single, low energy, avoided crossing (as seen in Fig 6.1), which is present at the same position in all our hybrid algorithms. We then show that the essential features of the behaviour are captured by a simple, two-state single avoided crossing model which all the hybrid algorithms map to in the large size limit. For this simple avoided crossing model we can easily show that the hybrid algorithms all provide an optimal quantum speed up. It then follows that our full-size hybrid algorithms have the same asymptotic scaling.

Dominance of a single avoided crossing is the method used to solve analytically for all Hamiltonian-based quantum search algorithms treated to date, including the complete graph [176] and Cartesian lattices (which provide a quantum speed up for $d \geq 4$ dimensions) [167]. It is also the typical behaviour for a broad class of random search graphs [168].

2.2.1 Reduction to single avoided crossing model

We first consider the end points of the interpolation, QW and AQC search. For AQC search, the optimal schedule $s^{(c)}(\tau)$ or $s^{(n)}(\tau)$ is derived directly from the functional form of lowest energy gap, ensuring that the Hamiltonian is changed slowly enough to avoid transitions to higher energy levels. We only need to show that the low energy structure of the Hamiltonian is dominated by a single avoided crossing throughout the process. This is shown numerically in Fig. 6.3. The width $w(n)$ of the avoided crossing decreases rapidly with n. Even for a modest size of $n = 50$ qubits, the switch from 95% overlap with the hypercube Hamiltonian ground state to 95% overlap with the marked state occurs in less than 10^{-6} of the total dynamic range of the protocol, which runs from $s(\tau) = 0$ to $s(\tau) = 1$[4]. In contrast, for QW search, transitions to higher energy levels are a necessary part of the evolution to the marked state, so we need to determine the scaling of several related quantities to show that a single avoided crossing dominates in determining the behaviour.

For QW search, to show numerically that the lowest avoided crossing is the only relevant feature in the large N limit, we must demonstrate two things. First, that the minimum gap $g_{\min} = (E_1 - E_0)$ between the ground state and the first excited state becomes much smaller than the minimum gap between the ground state and the second excited state. Second, that the lowest avoided level crossing, where $g(\tau) =$

---

[4] While the dynamical range $w(n) = \Delta s(\tau)$ in which the state rotates between the two nearly-orthogonal states $|\psi_{\text{init}}\rangle$ and $|m\rangle$ becomes exponentially small, the total runtime $t_f \sim \sqrt{N} = \exp(n/2)$ grows even more quickly so that the time taken $w(n)/t_f$ increases with n.

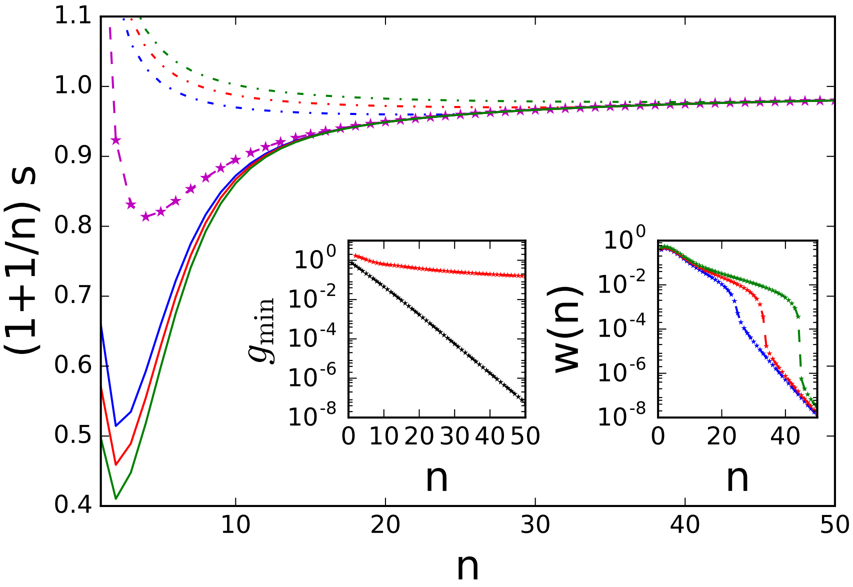

Figure 6.3: *Scaling of QW Hamiltonian properties tuned by* $s(\tau)$*.* Main figure: $s(\tau)$ scaled by $(1+1/n)$ against number of qubits n for 90% (blue, dark gray in print), 93% (red, light gray in print), 95% (green, mid gray in print) overlap of $|\psi(t)\rangle$ with $|m\rangle$ (solid) and with $|\psi_{\rm init}\rangle$ (dot-dashed). Magenta stars are the transition point, the value of $s(\tau)$ when the minimum gap $g_{\rm min}$ occurs. Left inset: $g_{\rm min} = \min(E_1 - E_0)$ (lower black stars) and $\min(E_2 - E_0)$ (upper red stars, light gray in print). Energy units given by Eq 6.24. Right inset: width of the transition $w(n) = \Delta s(\tau)$, the difference between solid and dot-dashed curves of the same color in the main figure. Calculated using the AQC search hypercube Hamiltonian mapped to the line, see Appendix D.

$g_{\rm min}$, dominates the transition between the ground state of the hypercube Hamiltonian $\hat{H}_0^{(h)}$ and the ground state of the marked state Hamiltonian $\hat{H}_{\rm P}$, and becomes more dominant as system size increases. Noting that around the minimum gap, where all the schedules cross, we have $(1 - s(\tau)) \simeq \gamma_o^{(h)}$, Figure 6.3 shows that both of these do, in fact, occur. The left inset shows that at the avoided crossing, the gap between the ground state and first excited state shrinks exponentially faster in n than the gap between the ground state and second excited state. The main figure and right inset of Fig. 6.3 show how the transition between the two ground states becomes dominated by the dynamics at $g_{\rm min}$ as n increases.

The hybrid algorithms on the full hypercube map onto the hybrid single avoided crossing model algorithms for large n. This follows from the solution methods for the end points, QW and AQC searching, which all use the two-level approximation to prove the quadratic speed up. Since the full hypercube hybrid algorithms are defined from these in the same way as the single avoided crossing model hybrid algorithms are defined, the hybrid algorithms also map to the corresponding single avoided crossing hybrid algorithm.

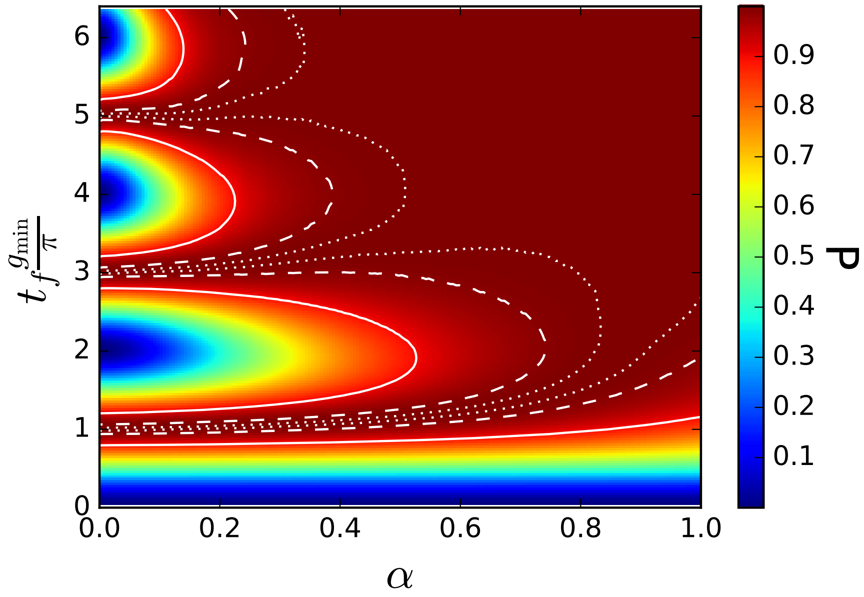

Figure 6.4: *Single avoided crossing search.* Probability P of finding the marked state versus runtime t_f and interpolation parameter α for the single avoided crossing model. White contours show solid=0.9, dashed=0.99, dotted=0.999 success probability P.

2.2.2 Analyzing the single avoided crossing model

We have shown that a single avoided crossing dominates for large N for both QW and AQC search algorithms on the hypercube. In Appendix E we describe how the hybrid searches can be mapped to a simple, two state, single avoided crossing model. By analyzing this model it can be demonstrated that the hybrid searches provide optimal quadratic quantum speedup. This model also allows us to see how the hybrid searches perform in the large size limit.

Fig 6.4 shows the final success probability of the single avoided crossing model of hybrid searching, in terms of α and runtime. Runtime is given in units of $\pi/g_{\min}$, which is the timescale required to obtain quadratic speedup since $g_{\min} \propto 1/\sqrt{N}$. Fig 6.4 demonstrates clearly that that all of the hybrid searches reach high success probability in this quadratic runtime. The white contours highlight the difference between the pure QW search, which succeeds with certainty, and the AQC and hybrid algorithms, which always have a probability of error ϵ^2 that can be traded against the runtime t_f. The shallow upward curve of these contours towards the AQC end of the hybrid protocols shows in what sense the QW search is better than AQC in the large size limit.

2.3 Performance in multiple search protocols

In the previous sections we derived hybrid search Hamiltonians for the hypercube, and studied their dynamics. However this doesn't yet give us a full picture of the relative usefulness of the different dynamics. In this section we study the relative performance of the different searches when we allow for the possibility of multiple searches.

Motivation

In a realistic setting of the search problem we can easily check whether the result of a search is the correct answer or not. Hence, we must consider not only single run strategies, but also multi-run strategies, where the success probability is defined as the probability of succeeding in at least one of several runs. In the context of quantum search on the hypercube, we measure which site of the hypercube our state is on, and then determine the energy of this state with respect to the search Hamiltonian. If this energy is zero, then we have found the state we are looking for, otherwise, we should re-initialize and run the search again. However, we also need to account for a non-zero 'initialization' time t_{init} associated with each run of the search. Such an initialization time is mathematically as well as physically necessary. The fidelity between the initial state and marked state $|\langle\psi_{\mathrm{init}}|m\rangle|^2 = \frac{1}{N}$ is non-zero. An arbitrarily short run is equivalent to making a random guess. Therefore, without an additional penalty per run, it would be possible to guess an arbitrarily large number of times for free, thus finding the marked state in a total arbitrarily short time. Any physical device will take a significant amount of time both to setup the initial state and to measure the final state. For the purposes of our study, the effects on the total search time of initialization and readout times are the same, therefore the quantity we call t_{init} should be taken to include all of the time associated with a single run other than the actual runtime of the algorithm t_f, i.e., as including both initialization and measurement.

Multiple run searching

As examples, we consider $n = 12$ and $n = 14$ qubits using the numerically calculated optimal strategy $s^{(n)}$. It turns out that $n = 12$ still shows finite size effects, while $n = 14$ is just into the smoothly scaling regime. We find for chosen success probabilities in the range $0.95-0.99$, the optimal strategy depends on both t_{init} and $\mathsf{P}_{\mathrm{target}}$ as shown in Fig. 6.5. For the range of t_{init} we examine, both sizes show a transition from a single run able to reach the required success probability to a region requiring two runs. The single runs are hybrid, becoming progressively more AQC-like as the required

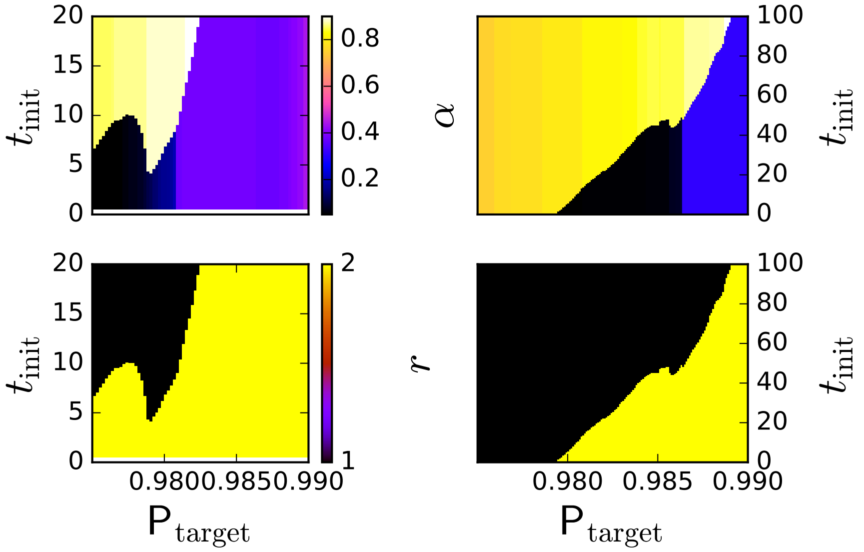

Figure 6.5: *Multiple run searching on finite systems.* Optimal number of runs r (bottom) and optimal α (top) for the numerically optimized strategy $s^{(n)}$ with $n = 12$ (left) and $n = 14$ (right) qubits versus t_{init} and search success probability P. t_{init} is in inverse energy units, given by Eq 6.24.

probability increases. At the point where two runs can do better than one AQC run, the two run strategy is much closer to quantum walk, but becomes progressively more hybrid as target success probability increases further. Finite size effects are visible for $n = 12$ in the non-monotonic shape of the boundary between one run and two runs in Fig. 6.5 (left). For smaller $n < 12$, these effects become more complicated, there is no single "best strategy" for a small search space. Indeed, we also found that the optimal strategy changes significantly when any of the parameters are varied. The complexity in the optimal search strategy for small n is because the two-level approximation does not hold well in this regime, and interactions with higher excited states have a non-negligible effect. This suggests that a similarly complex situation will likely be present in more sophisticated optimization Hamiltonians, whenever a two-level approximation is not valid.

In this section we introduced continuous-time search algorithms that combine the features of quantum walk and adiabatic dynamics, and assessed their performance in a closed setting. However a full picture of their performance must take into account the robustness to decoherence by the environment.

3 Noisy searching

An important practical consideration when comparing continuous-time quantum algorithms is how the performance depends on interactions with the environment. In this section we explore this in two limits, first when the system is in contact with an infinite temperature bath, and second using the matrix product state Langevin equation to model the interaction.

3.1 Infinite temperature bath

Another realistic situation where multiple runs can be helpful is when there is a significant level of unwanted decoherence or other forms of noise acting on the quantum hardware. In this case, shorter runs that end before decoherence effects are too strong, but consequently have lower success probabilities and hence need more repeats, may be able to maintain a quantum speed up. Decoherence in QW dynamics has been studied in [183, 184], and the effects of noise in AQC search have been studied in [185, 186]. Here we focus on hybrid algorithms, and the extra options these provide for optimizing the search.

3.1.1 Model

We choose a simple model of decoherence by adding a Lindblad term to the von-Neumann equation for the system density operator $\hat{\rho}(t)$,

$$\frac{\partial \hat{\rho}(t)}{\partial t} = -\frac{i}{\hbar}[\hat{H}(t), \hat{\rho}(t)] + \kappa \mathbb{P}[\hat{\rho}(t)], \tag{6.31}$$

where $\hat{H}(t)$ is the search Hamiltonian and $\kappa \mathbb{P}[\rho(t)]$ is a decoherence term tuned by a rate κ. We choose a form for $\mathbb{P}$ that uniformly reduces the coherences between states corresponding to vertices of the hypercube (the computational basis). This type of decoherence has been well-studied in the context of quantum walks [183, 187, 188] and, for high decoherence rate $\kappa \gg \gamma$, can be thought of as continuous measurement in the search space resulting in a quantum Zeno effect [189]. It is equivalent to coupling with an infinite temperature bath.

We begin by looking at how the instantaneous success probability $\mathsf{P}(t) = \langle m|\rho(t)|m\rangle$ evolves during a search, where m denotes the marked site. Figure 6.6 shows the evolution of $\mathsf{P}(t)$ during a search over an 8-qubit hypercube graph. The broad effect of the decoherence is to reduce the instantaneous success probability towards a value of $1/N$, equivalent to classical guessing. The QW, AQC and hybrid search algorithms retain their characteristics up to an overall decoherence damping, which is indepen-

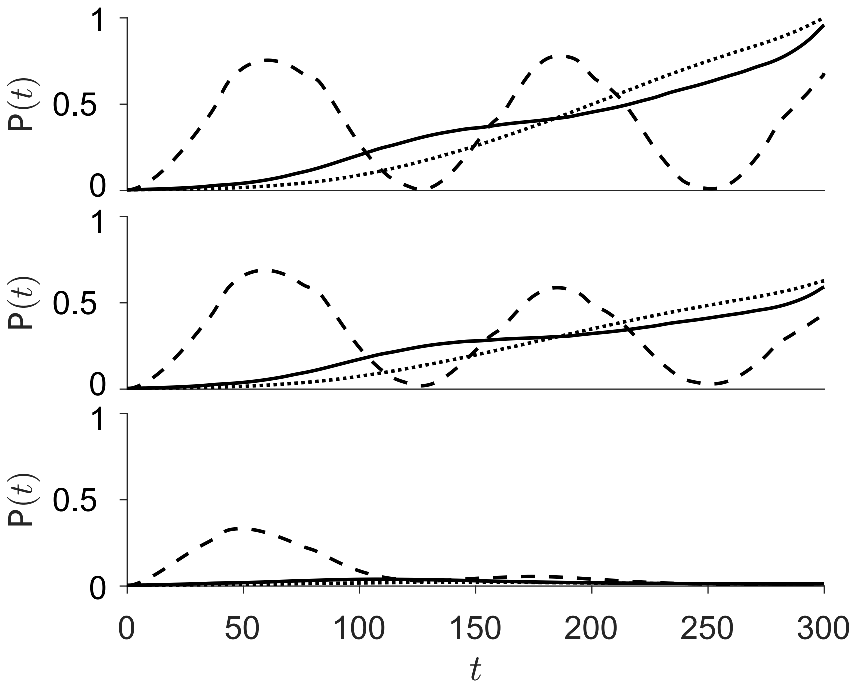

Figure 6.6: *Decohered searching.* Evolution of success probability $\mathsf{P}(t) = \langle m|\rho(t)|m\rangle$ during a single search over the $n = 8$ hypercube, dashed line is QW ($\alpha = 0$), dotted line is AQC ($\alpha = 1$), solid line is a hybrid search ($\alpha = 0.5$), with decoherence rate κ increasing from zero to 0.002 to 0.02 from the top to the middle to the bottom plot. Analytic expression (6.20) used for AQC schedule. Time units given by Eq 6.24.

dent of α. This suggests that the QW search, which spreads out more quickly over the search space, makes hybrid searches with more QW character better under decoherence. Indeed, for the higher decoherence rate in Fig. 6.6, QW run for a short time can obtain a reasonably high success probability, whereas longer hybrid or AQC runs fail entirely. The AQC search example in this figure relies on coherence sustained for longer times to reach high values of P. However, the results in Fig. 6.6 do not preclude the possibility that running AQC for a shorter period of time with lower success probability may still provide better performance than QW. As Fig. 6.7 shows, this does indeed happen over the range of parameters we examine.

3.1.2 Single search

Since we now have three parameters to optimize over for a given search size n, (t_f, α, and r for a decoherence rate κ), we first consider single run searches by calculating $\mathsf{P}(t_f, \alpha, \kappa)$. This is the final success probability of a hybrid search specified by α of duration t_f in the decoherence model of Eq 6.31 with decoherence rate κ. We simulate the searches for durations $0 \leq t_f \leq 200$, and define the search duration t_o that maximizes P for a particular choice of α and κ. We also define α_o as the value of α which maximizes $\mathsf{P}(t_o, \kappa, \alpha)$, this corresponds to the search that reaches highest suc-

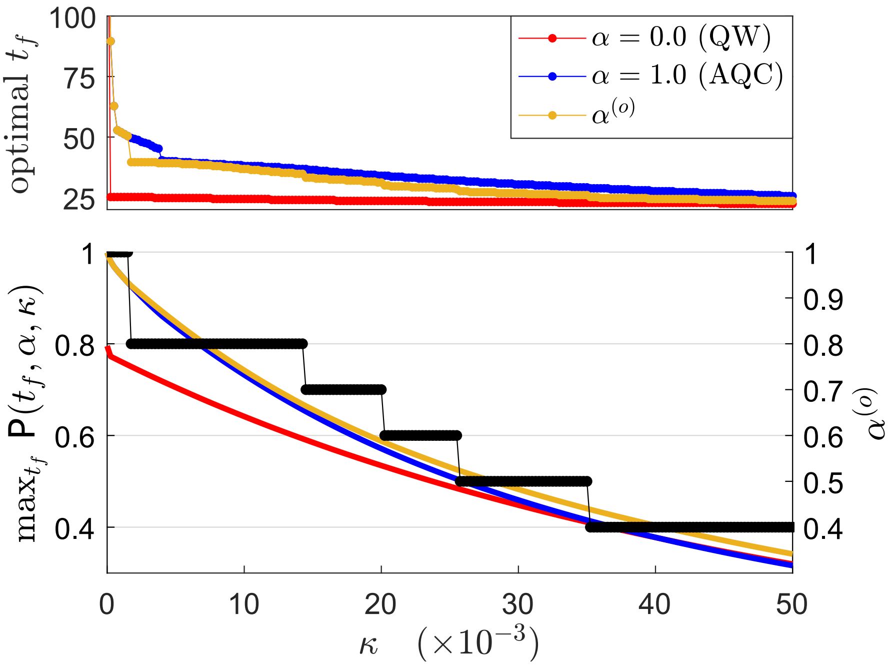

Figure 6.7: *Single noisy run analysis.* Quantum searching on the $n = 7$ hypercube for QW (red, mid gray in print)), AQC (blue, dark gray in print), and the hybrid search which yields the maximum P (orange, light gray in print) given by α_o. Top: search time t_o which maximizes P versus κ. The first data point (not shown) for the AQC and α_o series exceeds $t_f = 200$, the upper limit of search times sampled. Bottom: search probability $\mathsf{P}(t_f, \alpha, \kappa)$ versus decoherence rate κ maximized over search times $0 \leq t_f \leq 200$ (left axis). α_o as κ varies (black, right axis label). The α values sampled are $0.0, 0.1, \ldots, 1.0$. Analytic expression (6.20) used for AQC schedule. Time and rate units given by Eq 6.24.

cess probability for a given decoherence rate κ. Note that, for computational reasons, we limited α to the values $0.0, 0.1, 0.2 \ldots 0.9, 1.0$ when performing the maximizations; intermediate values are of course possible.

Figure 6.7 (bottom) shows the results of simulating this for searches over a $n = 7$ dimensional hypercube graph. As the decoherence rate is increased, the hybrid searches which combine QW and AQC characteristics are able to reach slightly higher success probabilities P. The optimal hybrid schedule given by α_o reduces as the decoherence rate κ increases, confirming our hypothesis that QW is more useful for high decoherence rates, due to its faster spreading. Our simulations find that, for small values of κ, we have $\alpha_o = 1$, i.e., AQC gives the highest peak success probability, because for $n = 7$ QW has a success probability significantly below one. As κ is increased, the highest-scoring search changes and α_o decreases monotonically, indicating hybrid searches perform the best overall for intermediate levels of decoherence. In the limit of very high decoherence we are in a quantum Zeno effect regime which keeps the search in the initial superposition over all possible states. This means all searches will succeed with the same probability $\mathsf{P} = |\langle\psi_{\text{init}}|m\rangle|^2 = 1/N$, equivalent to classical guessing. The usefulness of a search is also determined by how quickly it can be performed. The results for t_f in Fig. 6.7 (top) show that, while QW never has the highest success probability in the range we examine, it can be substantially quicker. This means that as the decoherence rate is increased, hybrid schedules take on more QW character and soon begin to achieve higher success probabilities than AQC in shorter search times.

3.1.3 Multiple searches

Having characterized the effects of decoherence on a single run, we now consider multiple-run search strategies where each search is of the same duration t_f. We define the optimal annealing schedule as that which minimizes the time taken to reach a given success probability, optimized over all equal duration multiple-run hybrid search strategies, with durations of individual searches in the range $0 < t_f \leq 200$. There are three variables to examine: the success probability P, the initialization time between searches t_{init}, and the decoherence rate κ. We denote the number of runs by r, so the combined search time is rt_f, the combined initialization time is rt_{init}, and the total time taken is $r(t_f + t_{\text{init}})$. By tuning r, α, and t_f, the multiple-search algorithm can be optimized.

To make this multiple parameter optimization tractable, we considered a discrete set of values for $\alpha = 0, 0.1, \ldots, 1.0$, and then minimized the total time $r(t_f + t_{\text{init}})$ while varying P, t_{init} and κ. The results for a 7-dimensional hypercube are shown in Fig. 6.8. The optimal hybrid schedule α and number of runs r taken by the best performing multiple-run hybrid search are shown as a function of κ, t_{init}, and P.

There is a small threshold initialization time below which the best strategy is to take multiple measurements of the system state as soon as it is prepared at a small cost rt_{init}, indicating that our device can do no better than classical random guessing. Other than this threshold, there is little dependence on initialization time. There is a broad tendency towards AQC-like searches as P is increased, however for larger values of κ an AQC search ceases to ever be optimal and hybrid or QW searches are preferred. As κ is increased, there is a localized trend for more AQC-like searches to be optimal, however this is punctuated with discontinuous changes to a more QW-like search. The reason for these discontinuous changes can be seen in the right plots of Fig. 6.8. The boundaries where another run is required correspond exactly to the regions where the optimal value of α suddenly drops. This transition arises when the decoherence rate κ and/or target success probability P have increased such that the best performing strategy with r searches drops below P, and another run is required. In this case the target can be reached by $r + 1$ lower quality searches. This drop in the quality required of the single search means a faster, more QW-like search can be

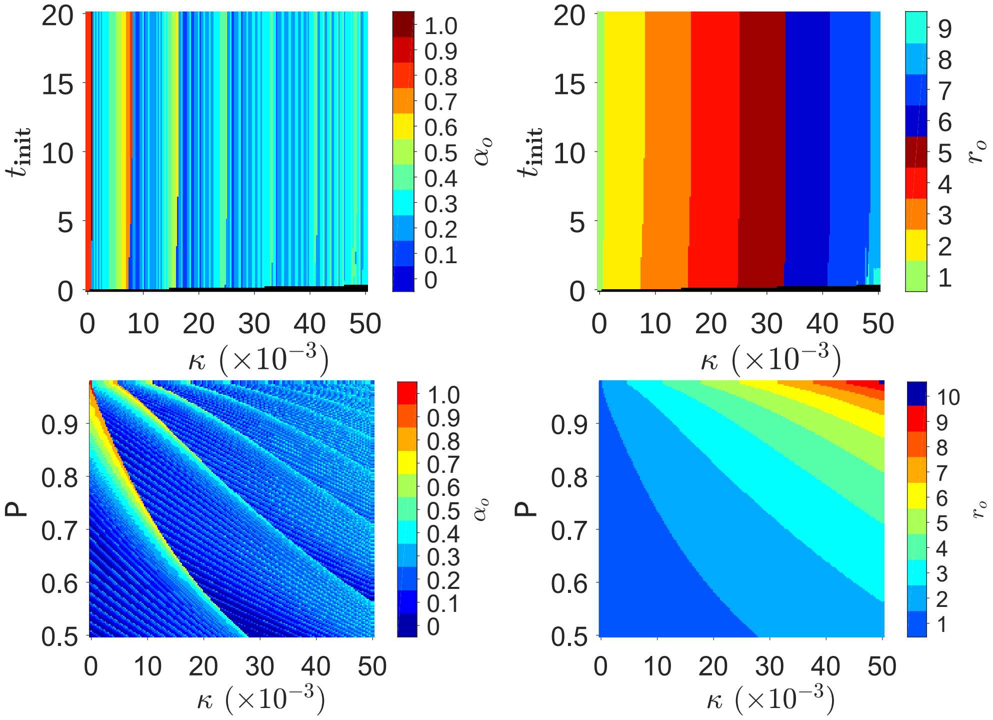

Figure 6.8: *Multiple noisy runs.* Optimal hybrid search parameter α_o and number of runs r_o for multiple-run searching on an $n = 7$ hypercube. The optimal search is that which achieves the target success probability P in the shortest total time $r(t_{\text{init}} + t_f)$, where t_{init} and t_f are the initialization and run times respectively. Top row: dependence on t_{init} and decoherence rate κ when P is fixed to 0.95. Black indicates the region of instantaneous measuring with $t_f = 0$, where $r = 382$. Bottom row: dependence on P and κ when t_{init} is fixed to 10. LHS plots show α_o, RHS plots show r_o. Analytic expression (6.20) used for AQC schedule. Time and rate units given by Eq 6.24.

used to succeed, and therefore the optimal value of α drops.

3.2 Finite temperature bath

3.2.1 Model and approach

Hybrid quantum searching using a system in contact with a finite temperature environment can be modelled using the matrix product state Langevin equation derived in chapter 4. Here we model the effects of friction and dissipation on the hybrid searches. An isotropic coupling is assumed, where each qubits is coupled through $\hat{\sigma}_x, \hat{\sigma}_y$ and $\hat{\sigma}_z$. In the Langevin description these coupling are accounted for by a friction term $\gamma_{F,i}\partial_t\langle\hat{\sigma}_i\rangle\langle\partial_{\bar{X}_j}\psi|\hat{\sigma}_i|\psi\rangle$, and a noise term $\eta_i(t)\langle\partial_{\bar{X}_j}\psi|\hat{\sigma}_i|\psi\rangle$ in the equation of motion for the matrix product state description of the system in terms of X_j. Here i denotes the coupling operator, and $\gamma_{F,i}$ denotes frictional coupling strength, and the friction and noise effects obey a fluctuation dissipation relation $\langle\eta_i(t)\eta_i(t')\rangle = 2\gamma_{F,i}T_i$ where T_i is the temperature of the corresponding bath. In these simulations no local approximation was made for the friction term.

The search problem as formulated here is not well suited to being efficiently simulated for large systems with matrix product states. This is because the marked state term $-|m\rangle\langle m|$ is highly non-local. However we can still apply the technique of the matrix product state Langevin equation introduced in chapter 4 to get some insight into how the hybrid searches fare under noise and dissipation. While the results of the previous subsection are valid at the limit of high-temperature, the Langevin equation lets us look at lower temperatures.

3.2.2 Frictional searching

We have seen already the effect of dephasing on the hybrid quantum searches – overall the fidelity with the marked state $\mathsf{P}(t)$ is adversely affected, with QW dynamics being more robust to this. At cooler temperatures, noise from the environment will no longer dominate over dissipation, and so dissipation will be more important.

We can explore this by simulating quantum searches in the friction-only limit, $T = 0$. The effect of the environment will then be to draw energy out of the system by driving it to its ground state. Fig 6.9 shows the effect of this for a 3-qubit search in the case of QW ($\alpha = 0$), hybrid ($\alpha = 0.5$) and AQC ($\alpha = 1$) searches, for search durations either side of and equal to the optimal QW measuring time. By looking at the overlap with the marked site in the ground state we can see that the dissipative effect of the environment is sometimes helpful, and sometimes detrimental. For $t < 4$ the friction improves the performance of the QW search, and the short-time $\alpha = 0.5, 1$

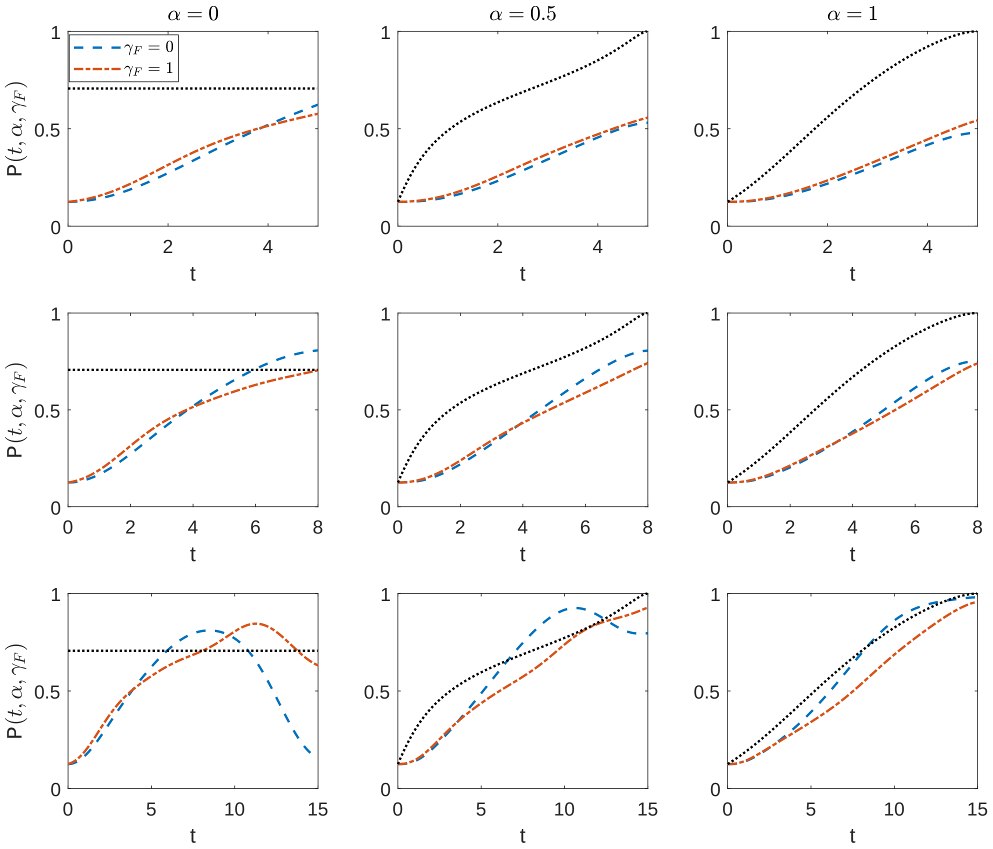

Figure 6.9: *Frictional hybrid quantum searching.* Evolution of marked state probability P for $\alpha = 0$ (left), $\alpha = 0.5$ (centre), and $\alpha = 1$ (right), both without friction (dashed) and with friction (dot-dashed). Evolution times less than (top row), equal to (middle row) and greater than (bottom row) tha optimal QW measuring time are used. Shown in a dotted line is the marked state probability of the instantaneous ground state. The effect of friction is to drive the system towards its ground state, which can prove useful – eg for a short-time QW search – or detrimental, as in the case of the longer-time hybrid and AQC searches. Time units given in units defined by Eq 6.24

hybrid and AQC searches. Moreover, at later times the friction delays the first QW peak and increases its amplitude slightly. On the other hand, for the hybrid and AQC searches where adiabatic dynamics are used to follow the ground state, the effect of friction is seen to hamper this process for the two longer search times.

These results give an insight into how dissipation affects the quantum search algorithms presented in this chapter. Friction affecting the system will drive it towards its ground state, which is quite different for the QW and AQC searches. The QW search relies on coherent oscillations between eigenstates to rotate the system close to the marked state. Friction will act to dampen these oscillations towards the ground state. In the regime of critical or overdamping this will be detrimental as the ground state will be farther from the marked state than the system can achieve without friction. However in the underdamped regime the friction can accelerate the initial motion, and lead to an overshooting of the ground state that can outperform the closed system dynamics. This initial acceleration is seen in Fig 6.9 for $\alpha = 0$ at smaller times, and the overshooting can be seen in frictional peak in the bottom-left plot.

On the other hand, the adiabatic dynamics relies on following the system ground state. Fig 6.9 shows that friction can either help or hinder this depending on timescales involved. At shorter times – ie. faster sweeps far from the adiabatic regime – friction helps the system follow the ground-state more closely. At longer times the friction hampers the system's ability to follow the instantaneous ground state.

4 Discussion

This chapter has provided a detailed study of the scaling of continuous-time quantum search algorithms on a hypercube graph. This work is published here [162]. A family of hybrid search algorithms, that interpolate between quench-like dynamics of a quantum walk (QW) and adiabatically following a slowly-changing Hamiltonian (AQC), are defined. By demonstrating that in the limit of large systems the dynamics are dominated by a two-level model we are able to show that the whole family achieve the optimal $\sqrt{N}$ speedup in the large N limit. This provides an ideal scenario to studying the optimization of a realistic quantum computer – far from the large N limit, and with imperfect control and isolation from the environment – by tuning the relative strengths of QW and AQC dynamics.

Our hybrid QW-AQC schedules are an example of the advantages we gain by treating both QW and AQC as part of the same method of continuous-time quantum computing [190]. We find that hybrid strategies intermediate between QW and AQC provide the best quantum search algorithm under a range of realistic conditions. This work has focussed on the simple case of quantum searching on a hypercube graph, where optimal AQC schedules[5] and QW hopping rates can be derived. The techniques we used here could easily be extended to hybrid quantum search on other graphs, and to other quantum walk or adiabatic quantum computing algorithms. For example, more general 'fixed point' searches, where more than one state is marked, have been studied in the context of both QW [191] and AQC [192], so a similar hybridization of QW and AQC effects should be straightforward. The single avoided crossing arguments used here are similar to those used in [168] for random graphs, suggesting that study of QW-AQC hybridization may be possible here too.

The physical implementations of the hybrid search algorithms studied here can be thought of as quantum control for optimization and search, with slowly varying control fields corresponding to the schedules A and B. The result that optimal quantum speedup is yielded by hybrid schedules, part QW and part AQC, suggests a promising flexibility in continuous-time quantum computing algorithms. For example, the Quantum Approximate Optimization Algorithm [193, 194], in which the controls are rapidly switched between extreme values [195], can be shown to provide optimal quantum speedup for searching [196]. While such a scheme is unfeasible in practice, the success of hybrid QW-AQC searches suggest that a time-smoothed approximation may still provide speedup.

---

[5] The derivation for searching on the hypercube graph can be found in Appendix C.

As well as problem size, the performance of a quantum search in a realistic setting will depend on many other factors. By performing a fairly general and multi-faceted analysis of such factors, we uncover a landscape where no single protocol dominates. In asymptotically large systems with perfectly specified problems, a straightforward QW approach is best. However, this limit is approached slowly, since the success probability for QW scales only as n, i.e., logarithmically in problem size N. A rich structure exists for computationally interesting, non-asymptotic sizes. On the other hand, for asymptotically large systems with some degree of problem misspecification, interpolated protocols can outperform the QW approach[6].

Another important aspect of a realistic setting is the impact of open system effects. Two regimes were considered: a high-temperature dephasing bath, and a low-temperature dissipative bath that drives the system towards its ground state. This reveals a rich structure in the optimal level of hybridization, depending on factors such as the initialization and readout time, the coupling strength and temperature of the system's environment.

This work is motivated by the premise that quantum computing protocols must in the end take place in physical systems. Protocols involving continuously changing the Hamiltonian are easier to control than those involving discretely applied logic gates, and quantum computers implementing such protocols on large numbers of qubits already exist [197, 198, 199]. The methods and results of this research will enable better optimization of realistic machines.

---

[6] This analysis can be found in the related paper [162]

Chapter 7

Discussion

In this final chapter I summarize the work of this thesis and describe how its different aspects relate to the evolution of entanglement structure in open quantum systems. Suggestions for future developments of this work are given.

Key to developing new quantum technologies is the ability to manipulate entangled states of many-body quantum systems. Quantum entanglement has been shown to be a resource for quantum computing [5], and appears in important bounds in quantum communication [200]. However for many-body systems entanglement is a structured concept: many bipartitions of the system can be chosen, and even partitionings into more than two parts.

In this thesis I have presented research into the both the physics of such systems and their potential use for quantum technologies. The main techniques used relate to matrix product state parameterizations of the many-body Hilbert space, which provide a natural encoding of entanglement structure. In Chapter 3 it was shown how accurate long-time simulation of matrix product states can be used to study thermalization of many-body quantum systems in terms of dynamical chaos. This provides a bridge between quantum and classical accounts of thermalization in many body quantum systems and gives a complementary account of quantum thermalization and integrability. Chapters 4 and 5 describe the development and application of a Langevin open systems model that uses matrix product state trajectories to account for a thermal coupling between the system and its environment. Proof-of-concept studies into using this for real-time ground state finding and sampling thermal distributions of state variables are presented, as well as a study into how noise and dissipation affect the generation of entanglement in a spin chain. Chapter 6 focusses on the practical problem of using continuous-time quantum computing algorithms on realistic near-term hardware: of intermediate size and subject to unwanted environmental effects. The nature of two different physical processes that can be used to achieve the same quantum speedup in the unstructured search problem is explored. The two schemes are hybridized, and the resulting family of algorithms are studied in the presence of high-temperature and low-temperature baths.

One of the major difficulties in studying many-body quantum systems is the exponentially growing size of the Hilbert space as more bodies are added. The advantage of using matrix product state based techniques is that for locally entangled states in one dimension, a finite bond dimension can be sufficient. The resulting manifolds of matrix product states of fixed bond dimension grows only polynomially with systems size. By extending matrix product state techniques to the study of chaotic diverging trajectories, and open systems effects, this advantage is built on to provide new methods for studying many-body quantum systems.

The main achievements of the research presented here are i. a new technique for studying quantum thermalization via extracting Lyapunov spectra for chaotic matrix product state trajectories, ii. a new technique, and publicly available code library[1], for matrix product state simulations of a Langevin open systems model, and iii. A detailed study into interpolating different physical mechanisms to gain advantage in quantum searching on realistic machines.

---

[1] Available at `github.com/JGMorley/mps_langevin`.

Chapter 8

Bibliography

[1] UK Research and Innovation. UK at the forefront of quantum technologies. `https://www.ukri.org/news/uk-at-the-forefront-of-quantum-technologies/`. Accessed July 2019.

[2] European Commission. Quantum technologies flagship. `https://ec.europa.eu/digital-single-market/en/quantum-technologies`. Accessed July 2019.

[3] The Economist. Quantum technology is beginning to come into its own. `https://www.economist.com/news/essays/21717782-quantum-technology-beginning-come-its-own`. Accessed July 2019.

[4] C L Degen, F Reinhard, and P Cappellaro. Quantum sensing. *Reviews of Modern Physics*, 89(3):035002, 2017.

[5] Nicolas Gisin, Grégoire Ribordy, Wolfgang Tittel, and Hugo Zbinden. Quantum cryptography. *Reviews of Modern Physics*, 74(1):145–195, 2002.

[6] T. D. Ladd, F. Jelezko, R. Laflamme, Y. Nakamura, C. Monroe, and J. L. O'Brien. Quantum computers. *Nature*, 464(7285):45–53, 2010.

[7] G. E. Coxson C. R. Hill J. C. Russo. Adiabatic quantum computing for finding low-peak-sidelobe codes, 2014. Presented at the 2014 IEEE High Performance Extreme Computing conference.

[8] Michael Marzec. *Portfolio Optimization: Applications in Quantum Computing*, pages 73–106. John Wiley & Sons, Inc., 2016.

[9] Zhaokai Li, Nikesh S. Dattani, Xi Chen, Xiaomei Liu, Hengyan Wang, Richard Tanburn, Hongwei Chen, Xinhua Peng, and Jiangfeng Du. High-fidelity adiabatic quantum computation using the intrinsic hamiltonian of a spin system: Application to the experimental factorization of 291311. Preprint at `https://arxiv.org/abs/1706.08061`, 2017.

[10] Zhengbing Bian, Fabian Chudak, William G. Macready, Lane Clark, and Frank Gaitan. Experimental determination of ramsey numbers. *Phys. Rev. Lett.*, 111:130505, 2013.

[11] Alejandro Perdomo-Ortiz, Neil Dickson, Marshall Drew-Brook, Geordie Rose, and Alan Aspuru-Guzik. Finding low-energy conformations of lattice protein models by quantum annealing. *Scientific Reports*, 2(571), 2012.

[12] L. Essen and J. V. L. Parry. An atomic standard of frequency and time interval: A cæsium resonator. *Nature*, 176:280–282, 1955.

[13] Richard Feynman. In *Feynman and Computation: exploring the limits of computers (edited by Hey, A. J. G.)*.

[14] D. Deutsch. Quantum theory, the Church-Turing principle and the universal quantum computer. *Proceedings of the Royal Society of London A*, 400(97), 1985.

[15] D. Deutsch and R. Jozsa. Rapid Solution of Problems by Quantum Computation. *Proceedings of the Royal Society A: Mathematical, Physical and Engineering Sciences*, 439, 2006.

[16] Peter W. Shor. Polynomial-Time Algorithms for Prime Factorization and Discrete Logarithms on a Quantum Computer. *SIAM Journal on Computing*, 25(5):1484–1509, 2003.

[17] David P. DiVincenzo and IBM. The Physical Implementation of Quantum Computation. *Fortschritte der Physik*, 48, 2000.

[18] R. Barends, J. Kelly, A. Megrant, A. Veitia, D. Sank, E. Jeffrey, T. C. White, J. Mutus, A. G. Fowler, B. Campbell, Y. Chen, Z. Chen, B. Chiaro, A. Dunsworth, C. Neill, P. O'Malley, P. Roushan, A. Vainsencher, J. Wenner, A. N. Korotkov, A. N. Cleland, and John M. Martinis. Superconducting quantum circuits at the surface code threshold for fault tolerance. *Nature*, 508:500, 2014.

[19] R. Barends, A. Shabani, L. Lamata, J. Kelly, A. Mezzacapo, U. Las Heras, R. Babbush, A. G. Fowler, B. Campbell, Yu Chen, Z. Chen, B. Chiaro, A. Dunsworth, E. Jeffrey, E. Lucero, A. Megrant, J. Y. Mutus, M. Neeley, C. Neill, P. J. J. O'Malley, C. Quintana, P. Roushan, D. Sank, A. Vainsencher, J. Wenner, T. C. White, E. Solano, H. Neven, and John M. Martinis. Digitized adiabatic quantum computing with a superconducting circuit. *Nature*, 534:222, 2016.

[20] J. Kelly, R. Barends, A. G. Fowler, A. Megrant, E. Jeffrey, T. C. White, D. Sank, J. Y. Mutus, B. Campbell, Yu Chen, Z. Chen, B. Chiaro, A. Dunsworth, I.-C. Hoi, C. Neill, P. J. J. O'Malley, C. Quintana, P. Roushan, A. Vainsencher, J. Wenner, A. N. Cleland, and John M. Martinis. State preservation by repetitive error detection in a superconducting quantum circuit. *Nature*, 519:66, 2015.

[21] Sergio Boixo, Sergei V. Isakov, Vadim N. Smelyanskiy, Ryan Babbush, Nan Ding, Zhang Jiang, Michael J. Bremner, John M. Martinis, and Hartmut Neven. Characterizing quantum supremacy in near-term devices. *Nature Physics*, 14:595–600, 2018.

[22] A Einstein. Letter to Max Born, 4th December 1926. Published in 1971, Irene Born (translator), *The Born-Einstein Letters*, Walker and Company, New York.

[23] John Stewart Bell. On the Einstein Podolsky Rosen paradox. *Physics*, 1(3):195–200, 1964.

[24] Annual semiconductor sales increase 21.6 percent, top $ 400 billions for first time. `https://www.semiconductors.org/annual-semiconductor-sales-increase-21-6-percent-top-400-billion-for-first-time`. Accessed: 21-08-2019.

[25] H. Müntinga, H. Ahlers, M. Krutzik, A. Wenzlawski, S. Arnold, D. Becker, K. Bongs, H. Dittus, H. Duncker, N. Gaaloul, C. Gherasim, E. Giese, C. Grzeschik, T. W. Hänsch, O. Hellmig, W. Herr, S. Herrmann, E. Kajari, S. Kleinert, C. Lämmerzahl, W. Lewoczko-Adamczyk, J. Malcolm, N. Meyer, R. Nolte, A. Peters, M. Popp, J. Reichel, A. Roura, J. Rudolph, M. Schiemangk, M. Schneider, S. T. Seidel, K. Sengstock, V. Tamma, T. Valenzuela, A. Vogel, R. Walser, T. Wendrich, P. Windpassinger, W. Zeller, T. van Zoest, W. Ertmer, W. P. Schleich, and E. M. Rasel. Interferometry with bose-einstein condensates in microgravity. *Phys. Rev. Lett.*, 110:093602, 2013.

[26] Ying Lia Li and P. F. Barker. Characterization and testing of a micro-g whispering gallery mode optomechanical accelerometer. *J. Lightwave Technol.*, 36(18):3919–3926, 2018.

[27] P. W. Shor. Algorithms for quantum computation: Discrete logarithms and factoring. In *Proceedings of the 35th Annual Symposium on Foundations of Computer Science*, SFCS '94, pages 124–134, Washington, DC, USA, 1994. IEEE Computer Society.

[28] John F. Clauser, Michael A. Horne, Abner Shimony, and Richard A. Holt. Proposed experiment to test local hidden-variable theories. *Phys. Rev. Lett.*, 23:880–884, 1969.

[29] E Schrödinger. Discussion of Probability Relations between Separated Systems. *Math. Proc. Cambridge Phil. Soc.*, 31(04):555–563, 1935.

[30] Michael A. Nielsen and Isaac L. Chuang. *Quantum Computation and Quantum Information.* Cambridge University Press, 2010.

[31] Vivien Kendon, Kae Nemoto, and William Munro. Typical entanglement in multiple-qubit systems. *Journal of Modern Optics*, 49(10):1709–1716, 2002.

[32] Vivien M Kendon and William J Munro. Entanglement and its role in shor's algorithm. *arXiv preprint quant-ph/0412140*, 2004.

[33] Max Born. Zur quantenmechanik der stoßvorgänge. *Zeitschrift für Physik*, 37(12):863–867, 1926.

[34] James Binney and David Skinner. *The Physics of Quantum Mechanics.* Oxford University Press, Oxford, 2013.

[35] Seth Lloyd. Computational capacity of the universe. *Phys. Rev. Lett.*, 88:237901, 2002.

[36] Ulrich Schollwöck. The density-matrix renormalization group in the age of matrix product states. *Ann. Phys.*, 326(1):96–192, 2011.

[37] J. M. Deutsch. Quantum statistical mechanics in a closed system. *Phys. Rev. A*, 43:2046–2049, 1991.

[38] Mark Srednicki. Chaos and quantum thermalization. *Phys. Rev. E*, 50:888–901, 1994.

[39] Marcos Rigol, Vanja Dunjko, and Maxim Olshanii. Thermalization and its mechanism for generic isolated quantum systems. *Nature*, 452:854, 2008.

[40] Stuart S. Szigeti, Andre R. R. Carvalho, James G. Morley, and Michael R. Hush. Ignorance is bliss: General and robust cancellation of decoherence via no-knowledge quantum feedback. *Phys. Rev. Lett.*, 113:020407, 2014.

[41] Robert Brown. XXVII. a brief account of microscopical observations made in the months of june, july and august 1827, on the particles contained in the pollen of plants; and on the general existence of active molecules in organic and inorganic bodies. *The Philosophical Magazine*, 4(21):161–173, 1828.

[42] Don S. Lemons and Anthony Gythiel. Paul Langevin's 1908 paper "On the Theory of Brownian Motion" ["Sur la Théorie du Mouvement Brownien," C. R. Acad. Sci. (Paris) 146, 530–533 (1908)]. *American Journal of Physics*, 65(11):1079–1081, 1997.

[43] Robert N. C. Pfeifer, Glen Evenbly, Sukhwinder Singh, and Guifre Vidal. NCON: A tensor network contractor for MATLAB. 2015. arXiv: `https://arxiv.org/abs/1402.0939`.

[44] A. Einstein, B. Podolsky, and N. Rosen. Can Quantum-Mechanical Description of Reality Be Considered Complete? *Physical Review*, 47:2–5, 1935.

[45] Jeffrey Bub. Quantum entanglement and information. In Edward N. Zalta, editor, *The Stanford Encyclopedia of Philosophy.* Metaphysics Research Lab, Stanford University, spring 2019 edition, 2019.

[46] Nicolas Laflorencie. Quantum entanglement in condensed matter systems. *Physics Reports*, 646:1–59, 2016.

[47] Rajibul Islam, Ruichao Ma, Philipp M. Preiss, M. Eric Tai, Alexander Lukin, Matthew Rispoli, and Markus Greiner. Measuring entanglement entropy in a quantum many-body system. *Nature*, 528(7580):77–83, 2015.

[48] Szilárd Szalay. Multipartite entanglement measures. *Physical Review A - Atomic, Molecular, and Optical Physics*, 92(4), 2015.

[49] John Preskill. Lecture notes for physics 229: Quantum information and computation. 1998. `http://www.theory.caltech.edu/~preskill/ph229/`, Accessed: 10-10-2019.

[50] Gene H Golub and Charles F Van Loan. *Matrix Computations.* Johns Hopkins University Press, 2013.

[51] J. Eisert, M. Cramer, and M. B. Plenio. Colloquium: Area laws for the entanglement entropy. *Rev. Mod. Phys.*, 82:277–306, 2010.

[52] Charles H. Bennett, Gilles Brassard, Claude Crépeau, Richard Jozsa, Asher Peres, and William K. Wootters. Teleporting an unknown quantum state via dual classical and Einstein-Podolsky-Rosen channels. *Physical Review Letters*, 70(13):1895–1899, 1993.

[53] Steven R. White. Density matrix formulation for quantum renormalization groups. *Physical Review Letters*, 69(19):2863–2866, 1992.

[54] Kenneth G. Wilson. Renormalization group methods. *Advances in Mathematics*, 16(2):170–186, 1975.

[55] J. Kondo. Resistance Minimum in Dilute Magnetic Alloys. *Progress of Theoretical Physics*, 32(1):37–49, 1964.

[56] Patrick A. Lee. Real-space scaling studies of localization. *Physical Review Letters*, 42(22):1492–1494, 1979.

[57] S. R. White and R. M. Noack. Real-space quantum renormalization groups. *Physical Review Letters*, 68(24):3487–3490, 1992.

[58] Ulrich Schollwöck. The density-matrix renormalization group in the age of matrix product states. *Annals of Physics*, 326(1):96–192, 2011.

[59] Jutho Haegeman, Tobias J Osborne, and Frank Verstraete. Post-matrix product state methods: To tangent space and beyond. *Physical Review B*, 88(075133), 2013.

[60] Jutho Haegeman, Michaël Mariën, Tobias J Osborne, Frank Verstraete, and Michä El Marï En. Geometry of matrix product states: Metric, parallel transport, and curvature. *Journal of Mathematical Physics*, 55(55):21902–42172, 2014.

[61] D. Perez-Garcia, F. Verstraete, M. M. Wolf, and J. I. Cirac. Matrix Product State Representations. *Quantum Inf. Comput.*, 7(5):401–430, 2007.

[62] Román Orús. A practical introduction to tensor networks: Matrix product states and projected entangled pair states. *Annals of Physics*, 349:117–158, 2014.

[63] Guifré Vidal. Efficient simulation of one-dimensional quantum many-body systems. *Physical Review Letters*, 93(4):040502–1, 2004.

[64] Jutho Haegeman, Christian Lubich, Ivan Oseledets, Bart Vandereycken, and Frank Verstraete. Unifying time evolution and optimization with matrix product states. *Phys. Rev. B*, 94(16):165116, 2016.

[65] A G Green, C A Hooley, J Keeling, and S H Simon. Feynman Path Integrals Over Entangled States. 2016. arXiv: `https://arxiv.org/abs/1607.01778`.

[66] F. Barratt, J. Dborin, V. Stojevic, and A. G. Green. In progress.

[67] P. A. M. Dirac. Note on Exchange Phenomena in the Thomas Atom. *Mathematical Proceedings of the Cambridge Philosophical Society*, 26(03):376, 1930.

[68] J Frenkel. *Wave Mechanics, Advanced General Theory.* Clarendon Press, Oxford, 1934.

[69] P. W. Langhoff, S. T. Epstein, and M. Karplus. Aspects of time-dependent perturbation theory. *Reviews of Modern Physics*, 44(3):602–644, 1972.

[70] Attila Szabo and Neil S Ostlund. *Modern Quantum Chemistry: Introduction to Advanced Electronic Structure Theory.* Number 1. Dover Publications, 1996.

[71] P Kramer and M Saraceno. *Geometry of the Time-Dependent Variational Principle in Quantum Mechanics.* Springer-Verlag Berlin Heidelberg, 1981.

[72] Jutho Haegeman, J Ignacio Cirac, Tobias J Osborne, Iztok Pižorn, Henri Verschelde, and Frank Verstraete. Time-Dependent Variational Principle for Quantum Lattices. *Physical Review Letters*, 107:070601, 2011.

[73] C. Karrasch and D. Schuricht. Dynamical phase transitions after quenches in non-integrable models. *Physical Review B - Condensed Matter and Materials Physics*, 87(19):195104, 2013.

[74] F. Andraschko and J. Sirker. Dynamical quantum phase transitions and the Loschmidt echo: A transfer matrix approach. *Physical Review B - Condensed Matter and Materials Physics*, 89(12):125120, 2014.

[75] A. Hallam, J. G. Morley, and A. G. Green. The Lyapunov spectra of quantum thermalisation. *Nature Communications*, 10(2708), 2019.

[76] Martin C. Gutzwiller. *Chaos in Classical and Quantum Mechanics.* Springer New York, 1990. In *Interdisciplinary Applied Mathematics.*

[77] Luca D'Alessio, Yariv Kafri, Anatoli Polkovnikov, and Marcos Rigol. From quantum chaos and eigenstate thermalization to statistical mechanics and thermodynamics. *Advances in Physics*, 65(3):239–362, 2016.

[78] Dieter Wintgen, Klaus Richter, and Gregor Tanner. The semiclassical helium atom. *Chaos: An Interdisciplinary Journal of Nonlinear Science*, 2(1):19–33, 1992.

[79] Dieter Weiss, Klaus Richter, A Menschig, R Bergmann, H Schweizer, Klaus von Klitzing, and G Weimann. Quantized periodic orbits in large antidot arrays. *Physical review letters*, 70(26):4118, 1993.

[80] Gregor Tanner, Klaus Richter, and Jan-Michael Rost. The theory of two-electron atoms: between ground state and complete fragmentation. *Reviews of Modern Physics*, 72(2):497, 2000.

[81] Martin Sieber and Klaus Richter. Correlations between periodic orbits and their rôle in spectral statistics. *Physica Scripta*, 2001(T90):128, 2001.

[82] Klaus Richter and Martin Sieber. Semiclassical theory of chaotic quantum transport. *Physical review letters*, 89(20):206801, 2002.

[83] Alexander Altland and Fritz Haake. Quantum chaos and effective thermalization. *Physical review letters*, 108(7):073601, 2012.

[84] Michael Victor Berry and Michael Tabor. Level clustering in the regular spectrum. *Proc. R. Soc. Lond. A*, 356(1686):375–394, 1977.

[85] Michael V Berry. Quantizing a classically ergodic system: Sinai's billiard and the kkr method. *Annals of Physics*, 131(1):163–216, 1981.

[86] Michael Berry. Quantum chaology, not quantum chaos. *Physica Scripta*, 40(3):335–336, 1989.

[87] Steven W McDonald and Allan N Kaufman. Spectrum and eigenfunctions for a hamiltonian with stochastic trajectories. *Physical Review Letters*, 42(18):1189, 1979.

[88] Oriol Bohigas, Marie-Joya Giannoni, and Charles Schmit. Characterization of chaotic quantum spectra and universality of level fluctuation laws. *Physical Review Letters*, 52(1):1, 1984.

[89] Thomas Guhr, Axel Müller-Groeling, and Hans A. Weidenmüller. Random-matrix theories in quantum physics: common concepts. *Physics Reports*, 299(4):189 – 425, 1998.

[90] C. W. J. Beenakker. Random-matrix theory of quantum transport. *Reviews of Modern Physics*, 69(3):731–808, 1997.

[91] Valery Iustinovich Oseledec. A multiplicative ergodic theorem. lyapunov characteristic number for dynamical systems. *Trans. Moscow Math. Soc.*, 19:197–231, 1968.

[92] David Ruelle. Ergodic theory of differentiable dynamical systems. *Publications Mathématiques de l'Institut des Hautes Études Scientifiques*, 50(1):27–58, 1979.

[93] J M Deutsch. Quantum statistical mechanics in a closed system. *Phys. Rev. A*, 43(4):2046–2049, 1991.

[94] Mark Srednicki. Chaos and quantum thermalization. *Phys. Rev. E*, 50(2):888–901, 1994.

[95] Marcos Rigol, Vanja Dunjko, and Maxim Olshanii. Thermalization and its mechanism for generic isolated quantum systems. *Nature*, 452:854, 2008.

[96] J. Haegeman, J. I. Cirac, T. J. Osborne, I. Pižorn, H. Verschelde, and F. Verstraete. Time-dependent variational principle for quantum lattices. *Phys. Rev. Lett.*, 107:070601, 2011.

[97] Eyal Leviatan, Frank Pollmann, Jens H Bardarson, and Ehud Altman. Quantum thermalization dynamics with matrix-product states. Preprint at https://arxiv.org/abs/1702.08894, 2017.

[98] Karlheinz Geist, Ulrich Parlitz, and Werner Lauterborn. Comparison of different methods for computing Lyapunov exponents. *Prog. Theor. Phys.*, 83(5):875–893, 1990.

[99] G. Benettin, L. Galgani, A. Giorgilli, and J.-M. Strelcyn. Lyapunov characteristic exponents for smooth dynamical systems and for Hamiltonian systems - A method for computing all of them. I - Theory. II - Numerical application. *Meccanica*, 15:9–30, 1980.

[100] J. P. Eckmann and D. Ruelle. Ergodic theory of chaos and strange attractors. *Rev. Mod. Phys.*, 57:617–656, 1985.

[101] Yasushi Takahasi and Hiroomi Umezawa. Thermo field dynamics. *Collect. Phenom.*, 2:55–80, 1974.

[102] Loïc Joubert-Doriol and Artur F Izmaylov. Problem-free time-dependent variational principle for open quantum systems. *The Journal of Chemical Physics*, 142(13):134107, 2015.

[103] Christopher David White, Michael Zaletel, Roger S. K. Mong, and Gil Refael. Quantum dynamics of thermalizing systems. *Phys. Rev. B*, 97:035127, 2018.

[104] J. Maldacena, S. H. Shenker, and D. Stanford. A bound on chaos. *J. High Energy Phys.*, 8:106, 2016.

[105] Yakov Borisovich Pesin. Characteristic lyapunov exponents and smooth ergodic theory. *Russian Mathematical Surveys*, 32(4):55–114, 1977.

[106] W. H. Zurek and J. P. Paz. Quantum chaos: a decoherent definition. *Physica D*, 83:300–308, 1995.

[107] Efim B Rozenbaum, Sriram Ganeshan, and Victor Galitski. Lyapunov exponent and out-of-time-ordered correlator's growth rate in a chaotic system. *Phys. Rev. Lett.*, 118(8):086801, 2017.

[108] Efim B Rozenbaum, Sriram Ganeshan, and Victor Galitski. Universal level statistics of the out-of-time-ordered operator. Preprint at `https://arxiv.org/abs/1801.10591`, 2018.

[109] Guy Gur-Ari, Masanori Hanada, and Stephen H Shenker. Chaos in classical D0-brane mechanics. *Journal of High Energy Physics*, 2016(2):91, 2016.

[110] M. Hanada, H. Shimada, and M. Tezuka. Universality in chaos: Lyapunov spectrum and random matrix theory. 97(2):022224, 2018.

[111] A. Bohrdt, C. B. Mendl, M. Endres, and M. Knap. Scrambling and thermalization in a diffusive quantum many-body system. *New Journal of Physics*, 19(6):063001, 2017.

[112] Tibor Rakovszky, Frank Pollmann, and CW von Keyserlingk. Diffusive hydrodynamics of out-of-time-ordered correlators with charge conservation. *Physical Review X*, 8(3):031058, 2018.

[113] C. W. von Keyserlingk, T. Rakovszky, F. Pollmann, and S. L. Sondhi. Operator Hydrodynamics, OTOCs, and Entanglement Growth in Systems without Conservation Laws. *Phys. Rev. X*, 8(2):021013, 2018.

[114] Xiao Chen, Tianci Zhou, David A Huse, and Eduardo Fradkin. Out-of-time-order correlations in many-body localized and thermal phases. *Annalen der Physik*, 529(7):1600332, 2017.

[115] Andrei E Tarkhov and Boris V Fine. Estimating ergodization time of a chaotic many-particle system from a time reversal of equilibrium noise. *New Journal of Physics*, 20(12):123021, 2018.

[116] G P Brandino, J.-S. Caux, and R M Konik. Glimmers of a quantum kam theorem: Insights from quantum quenches in one-dimensional bose gases. *Phys. Rev. X*, 5(4):041043, 2015.

[117] R Biele and R D'Agosta. A stochastic approach to open quantum systems. *Journal of Physics: Condensed Matter*, 24(27):273201, 2012.

[118] Mohammad Yaghoubi, M Ebrahim Foulaadvand, Antoine Bérut, and Jerzy Łuczka. Energetics of a driven brownian harmonic oscillator. *Journal of Statistical Mechanics: Theory and Experiment*, 2017(11):113206, 2017.

[119] Alex Kamenev. *Field theory of non-equilibrium systems.* Cambridge University Press, 2011.

[120] Alexander Altland and Ben D Simons. *Condensed matter field theory.* Cambridge University Press, 2010.

[121] J. B. Johnson. Thermal agitation of electricity in conductors. *Phys. Rev.*, 32:97–109, 1928.

[122] H. Nyquist. Thermal agitation of electric charge in conductors. *Phys. Rev.*, 32:110–113, 1928.

[123] G. Kirchhoff. Ueber das verhältniss zwischen dem emissionsvermögen und dem absorptionsvermögen der körper für wärme und licht. *Annalen der Physik*, 185(2):275–301, 1860.

[124] C. Gardiner, P. Zoller, and P. Zoller. *Quantum Noise: A Handbook of Markovian and Non-Markovian Quantum Stochastic Methods with Applications to Quantum Optics.* Springer Series in Synergetics. Springer, 2004.

[125] Inés de Vega and Daniel Alonso. Dynamics of non-Markovian open quantum systems. *Reviews of Modern Physics*, 89:015001, 2017.

[126] V. Vedral, M. B. Plenio, M. A. Rippin, and P. L. Knight. Quantifying Entanglement. *Physical Review Letters*, 78(12):2275–2279, 1997.

[127] Peter Zoller and C W Gardiner. Quantum Noise in Quantum Optics: the Stochastic Schrödinger Equation. 1997. arXiv: `http://arxiv.org/abs/quant-ph/9702030`.

[128] L. Diósi, N Gisin, and W T Strunz. Non-Markovian quantum state diffusion. *Physical Review A*, 58(3):1699–1712, 1998.

[129] Luc Bouten, Mădălin Guţă, and Hans Maassen. Stochastic Schrödinger equations. *Journal of Physics A: Mathematical and General*, 37(9):3189–3209, 2004.

[130] Emanuel Gull, Andrew J. Millis, Alexander I. Lichtenstein, Alexey N. Rubtsov, Matthias Troyer, and Philipp Werner. Continuous-time Monte Carlo methods for quantum impurity models. *Reviews of Modern Physics*, 83(2):349–404, 2011.

[131] Lode Pollet. Recent developments in quantum Monte Carlo simulations with applications for cold gases. *Reports on Progress in Physics*, 75(9):094501, 2012.

[132] S. J. Weber, A. Chantasri, J. Dressel, A. N. Jordan, K. W. Murch, and I. Siddiqi. Mapping the optimal route between two quantum states. *Nature*, 511(7511):570–573, 2014.

[133] A.O. Caldeira and A.J. Leggett. Path integral approach to quantum Brownian motion. *Physica A: Statistical Mechanics and its Applications*, 121(3):587–616, 1983.

[134] L. Ferialdi. Dissipation in the caldeira-leggett model. *Phys. Rev. A*, 95:052109, 2017.

[135] A. O. Caldeira and A. J. Leggett. Quantum tunnelling in a dissipative system. *Annals of Physics*, 149(2):374–456, 1983.

[136] A. J. Leggett. Quantum tunneling in the presence of an arbitrary linear dissipation mechanism. *Phys. Rev. B*, 30:1208–1218, 1984.

[137] M. D. Kostin. On the schrödinger-langevin equation. *The Journal of Chemical Physics*, 57(9):3589–3591, 1972.

[138] Göran Lindblad. Brownian motion of a quantum harmonic oscillator. *Reports on Mathematical Physics*, 10(3):393 – 406, 1976.

[139] Hajo Leschke and Manfred Schmutz. Operator orderings and functional formulations of quantum and stochastic dynamics. *Zeitschrift für Physik B Condensed Matter*, 27(1):85–94, 1977.

[140] Albert Schmid. On a quasiclassical langevin equation. *Journal of Low Temperature Physics*, 49(5):609–626, 1982.

[141] G. W. Ford, J. T. Lewis, and R. F. O'Connell. Quantum langevin equation. *Phys. Rev. A*, 37:4419–4428, 1988.

[142] Dhruba Banerjee, Bidhan Chandra Bag, Suman Kumar Banik, and Deb Shankar Ray. Solution of quantum langevin equation: Approximations, theoretical and numerical aspects. *The Journal of Chemical Physics*, 120(19):8960–8972, 2004.

[143] Alberto Barchielli and Bassano Vacchini. Quantum langevin equations for optomechanical systems. *New Journal of Physics*, 17(8):083004, 2015.

[144] S. V. Mousavi and S. Miret-Artés. Stochastic bohmian mechanics within the schrödinger-langevin framework: A trajectory analysis of wave-packet dynamics in a fluctuative-dissipative medium. *The European Physical Journal Plus*, 134(6):311, 2019.

[145] Andrew J. Daley. Quantum trajectories and open many-body quantum systems. *Advances in Physics*, 63(2):77–149, 2014.

[146] C-E Bardyn, M A Baranov, C V Kraus, E Rico, A İmamoğlu, P Zoller, and S Diehl. Topology by dissipation. *New Journal of Physics*, 15(8):085001, 2013.

[147] S. Diehl, M. Baranov, A. J. Daley, and P. Zoller. Quantum field theory for the three-body constrained lattice Bose gas. I. Formal developments. *Phys. Rev. B*, 82:064509, 2010.

[148] Philip J D Crowley and A G Green. An Anistropic Laundau-Lifschitz-Gilbert model of dissipation in qubits. *Physical Review A*, 94(6):16301114, 2015.

[149] P.E. Kloeden and E. Platen. *Numerical Solution of Stochastic Differential Equations*. Stochastic Modelling and Applied Probability. Springer Berlin Heidelberg, 2013.

[150] Eugene Wong and Moshe Zakai. On the convergence of ordinary integrals to stochastic integrals. *Ann. Math. Statist.*, 36(5):1560–1564, 1965.

[151] Wong Eugene and Zakai Moshe. On the relation between ordinary and stochastic differential equations. *International Journal of Engineering Science*, 3(2):213 – 229, 1965.

[152] U Schollwöck. The density-matrix renormalization group. *Rev. Mod. Phys.*, 77(1):259–315, 2005.

[153] Karen A. Hallberg. New trends in density matrix renormalization. *Advances in Physics*, 55(5-6):477–526, 2006.

[154] Immanuel Bloch, Jean Dalibard, and Wilhelm Zwerger. Many-body physics with ultracold gases. *Rev. Mod. Phys.*, 80:885–964, 2008.

[155] Waseem S. Bakr, Jonathon I. Gillen, Amy Peng, Simon Falling, and Markus Greiner. A quantum gas microscope for detecting single atoms in a hubbard-regime optical lattice. *Nature*, 462:74, 2009.

[156] G. Vidal. Classical simulation of infinite-size quantum lattice systems in one spatial dimension. *Phys. Rev. Lett.*, 98:070201, 2007.

[157] David Poulin and Pawel Wocjan. Sampling from the thermal quantum gibbs state and evaluating partition functions with a quantum computer. *Phys. Rev. Lett.*, 103:220502, 2009.

[158] Giovanni Bussi and Michele Parrinello. Accurate sampling using Langevin dynamics. *Phys. Rev. E*, 75:056707, 2007.

[159] Yaodong Li, Xiao Chen, and Matthew P. A. Fisher. Quantum zeno effect and the many-body entanglement transition. *Phys. Rev. B*, 98:205136, 2018.

[160] Amos Chan, Rahul M. Nandkishore, Michael Pretko, and Graeme Smith. Unitary-projective entanglement dynamics. *Phys. Rev. B*, 99:224307, 2019.

[161] Brian Skinner, Jonathan Ruhman, and Adam Nahum. Measurement-induced phase transitions in the dynamics of entanglement. *Phys. Rev. X*, 9:031009, 2019.

[162] James G. Morley, Nicholas Chancellor, Sougato Bose, and Viv Kendon. Quantum search with hybrid adiabatic–quantum-walk algorithms and realistic noise. *Phys. Rev. A*, 99:022339, 2019.

[163] Lov K Grover. A fast quantum mechanical algorithm for database search. In *Proceedings of the twenty-eighth annual ACM symposium on Theory of computing - STOC '96*, pages 212–219. ACM Press, 1996.

[164] N. Chancellor, S. Zohren, P. Warburton, S. Benjamin, and S. Roberts. A direct mapping of Max k-SAT and high order parity checks to a chimera graph. *Scientific Reports*, 6(37107), 2016.

[165] Nicholas Chancellor. Max-k-SAT, Multi-Body Frustration, & Multi-Body Sampling on a Two Local Ising System. AQC 2016. Available at: `https://www.youtube.com/watch?v=aC-6hg_h3EA`, 2016.

[166] Nicholas Chancellor, A. Ben Dodds, and Viv Kendon. Practical designs for permutation symmetric problem Hamiltonians on hypercubes, 2018. [In preparation].

[167] Andrew Childs and Jeffrey Goldstone. Spatial search by quantum walk. *Phys. Rev. A*, 70:022314, 2004.

[168] S. Chakraborty, L. Novo, A. Ambainis, and Y. Omar. Spatial search by quantum walk is optimal for almost all graphs. *Phys. Rev. Lett.*, 116(100501), 2016.

[169] Christopher Moore and Alexander Russell. Quantum walks on the hypercube. In J. D. P. Rolim and S. Vadhan, editors, *Proc. 6th Intl. Workshop on Randomization and Approximation Techniques in Computer Science (RANDOM '02)*, pages 164–178. Springer, 2002.

[170] Neil Shenvi, Julia Kempe, and K Birgitta Whaley. A quantum random walk search algorithm. *Phys. Rev. A*, 67:052307, 2003.

[171] Birgit Hein and Gregor Tanner. Quantum search algorithms on the hypercube. *J. Phys. A: Math. Theor.*, 42:085303, 2009.

[172] E. Farhi, J. Goldstone, S. Gutmann, and M. Sipser. Quantum computation by adiabatic evolution. 2000. arXiv: `http://arxiv.org/abs/quant-ph/0001106`.

[173] A. M. Childs, E. Deotto, E. Farhi, J. Goldstone, S. Gutmann, and A. J. Landahl. Quantum search by measurement. *Phys. Rev. A*, 66:032314, 2002.

[174] M. Born and V. Fock. Beweis des adiabatensatzes. *Z. Phys.*, 51(3-4):165–180, 1928.

[175] Tameem Albash and Daniel A. Lidar. Adiabatic quantum computing. *Rev. Mod. Phys.*, 90(015002), 2018.

[176] Jérémie Roland and Nicolas J. Cerf. Quantum search by local adiabatic evolution. *Phys. Rev. A*, 65:042308, 2002.

[177] Trevor Lanting. The D-Wave 2000Q Processor, 2017. Presented at AQC 2017.

[178] Daniel A. Lidar, Ali T. Rezakhani, and Alioscia Hamma. Adiabatic approximation with exponential accuracy for many-body systems and quantum computation. *Journal of Mathematical Physics*, 50:102106, 2009.

[179] A. T. Rezakhani, W.-J. Kuo, A. Hamma, D. A. Lidar, and P. Zanardi. Quantum adiabatic brachistochrone. *Phys. Rev. Lett.*, 103:080502, 2009.

[180] A. T. Rezakhani, A. K. Pimachev, and D. A. Lidar. Accuracy vs run time in adiabatic quantum search. *Phys. Rev. A*, 82:052305, 2010.

[181] Nathan Weibe and Nathan S Babcock. Improved error-scaling for adiabatic quantum evolutions. *New Journal of Physics*, 14(013024), 2012.

[182] Mária Kieferová and Nathan Wiebe. On the power of coherently controlled quantum adiabatic evolutions. *New Journal of Physics*, 16(12):123034, 2014.

[183] Gorjan Alagic and Alexander Russell. Decoherence in quantum walks on the hypercube. *Phys. Rev. A*, 72:062304, 2005.

[184] Viv Kendon. Decoherence in quantum walks – a review. *Mathematical Structures in Computer Science*, 17(6):1169–1220, 2007.

[185] Ines de Vega, Mari Carmen Bañuls, and A. Pérez. Effects of dissipation in an adiabatic quantum search algorithm. *New J. Phys.*, 12:123010, 2010.

[186] Dominik S. Wild, Sarang Gopalakrishnan, Michael Knap, Norman Y. Yao, and Mikhail D. Lukin. Adiabatic quantum search in open systems. *Phys. Rev. Lett.*, 117:150501, 2016.

[187] Peter C. Richter. Quantum speedup of classical mixing processes. *Phys. Rev. A*, 76:042306, 2007.

[188] Viv Kendon and Olivier Maloyer. Optimal computation with non-unitary quantum walks. *Theoretical Computer Science*, 394(3):187 – 196, 2008.

[189] B. Misra and E. C. G. Sudarshan. The Zeno's paradox in quantum theory. *Journal of Mathematical Physics*, 18(4):756–763, 1977.

[190] V.M. Kendon, N. Chancellor, S. Bose, and A. Daley. Developing continuous-time quantum computing, 2018. In preparation.

[191] Theodore J. Yoder, Guang Hao Low, and Isaac L. Chuang. Fixed-point quantum search with an optimal number of queries. *Phys. Rev. Lett.*, 113:210501, 2014.

[192] Alexander M. Dalzell, Theodore J. Yoder, and Isaac L. Chuang. Fixed-point adiabatic quantum search. *Phys. Rev. A*, 95:012311, 2017.

[193] Edward Farhi, Jeffrey Goldstone, and Sam Gutmann. A quantum approximate optimization algorithm, 2014. arXiv: `https://arxiv.org/abs/1411.4028`.

[194] Edward Farhi, Jeffrey Goldstone, and Sam Gutmann. A quantum approximate optimization algorithm applied to a bounded occurrence constraint problem, 2014. arXiv: `https://arxiv.org/abs/1412.6062`.

[195] Zhi-Cheng Yang, Armin Rahmani, Alireza Shabani, Hartmut Neven, and Claudio Chamon. Optimizing variational quantum algorithms using Pontryagin's minimum principle. *Phys. Rev. X*, 7:021027, 2017.

[196] Zhang Jiang, Eleanor G. Rieffel, and Zhihui Wang. Near-optimal quantum circuit for Grover's unstructured search using a transverse field. *Phys. Rev. A*, 95:062317, 2017.

[197] Hannes Bernien, Sylvain Schwartz, Alexander Keesling, Harry Levine, Ahmed Omran, Hannes Pichler, Soonwon Choi, Alexander S. Zibrov, Manuel Endres, Markus Greiner, Vladan Vuletić, and Mikhail D. Lukin. Probing many-body dynamics on a 51-atom quantum simulator. *Nature*, 551:579–584, 2017.

[198] J. Zhang, G. Pagano, P. W. Hess, A. Kyprianidis, P. Becker, H. Kaplan, A. V. Gorshkov, Z.-X. Gong, and C. Monroe. Observation of a many-body dynamical phase transition with a 53-qubit quantum simulator. *Nature*, 551:601–604, 2017.

[199] Andrew D. King, Juan Carrasquilla, Isil Ozfidan, Jack Raymond, Evgeny Andriyash, Andrew Berkley, Mauricio Reis, Trevor M. Lanting, Richard Harris, Gabriel Poulin-Lamarre, Anatoly Yu. Smirnov, Christopher Rich, Fabio Altomare, Paul Bunyk, Jed Whittaker, Loren Swenson, Emile Hoskinson, Yuki Sato, Mark Volkmann, Eric Ladizinsky, Mark Johnson, Jeremy Hilton, and Mohammad H. Amin. Observation of topological phenomena in a programmable lattice of 1,800 qubits. *Nature*, 560:455–460, 2018.

[200] P. J. D. Crowley, T. Duri, W. Vinci, P. A. Warburton, and A. G. Green. Quantum and classical dynamics in adiabatic computation. *Physical Review A - Atomic, Molecular, and Optical Physics*, 90(4):042317, 2014.

[201] Alan Wolf, Jack B. Swift, Harry L. Swinney, and John A. Vastano. Determining Lyapunov exponents from a time series. *Physica D*, 16(3):285 – 317, 1985.

[202] R. Brown, P. Bryant, and H. D. I. Abarbanel. Computing the Lyapunov spectrum of a dynamical system from an observed time series. *Physical Review A*, 43:2787–2806, 1991.

[203] H. Kantz. A robust method to estimate the maximal Lyapunov exponent of a time series. *Phys. Lett. A*, 185:77–87, 1994.

[204] J. P. Eckmann, S. Oliffson Kamphorst, D. Ruelle, and S. Ciliberto. Lyapunov exponents from time series. *Phys. Rev. A*, 34:4971–4979, 1986.

[205] Numpy 1.11.1, 2016. `http://www.numpy.org/`, accessed August 10th, 2016.

[206] Python 2.7 & Python 3.5, 2016. `https://www.python.org/`, accessed August 10th, 2016.

[207] Scipy 0.17.1, 2016. `https://www.scipy.org/`, accessed August 10th, 2016.

[208] Matplotlib 1.5.1, 2016. `http://matplotlib.org/`, accessed August 10th, 2016.

Appendices

Appendix A

Extracting the classical Lyapunov spectrum

Here we provide some additional details of how to extract Lyapunov spectra from linearised equations of motion, describing the evolution of the displacement between neighbouring trajectories $\mathbf{X}(t)$ and $\mathbf{X}(t)+d\mathbf{X}(t)$. The asymptotic rate at which these two trajectories diverge (or converge) is characterized with a Lyapunov exponent. If the solution for this equation is $d\mathbf{X}(t) = Y(\mathbf{X},t)d\mathbf{X}(0)$ then the Lyapunov exponent associated with these trajectories is[1]

$$\lambda = \lim_{t\to\infty} \frac{1}{t} \log \frac{|d\mathbf{X}(t)|}{|d\mathbf{X}(0)|} = \lim_{t\to\infty} \frac{1}{t} \log |Y(\mathbf{X},t)d\mathbf{X}(0)|. \tag{A.1}$$

For almost all trajectories $\mathbf{X}(t)$ and almost all tangent vectors $d\mathbf{X}(t)$ the limit in Eq.(A.1) converges to the largest Lyapunov exponent of the system [91, 92].

Using a similar approach it is possible to calculate the entire Lyapunov spectrum. Instead of a single trajectory, consider a d-dimensional parallelepiped defined by d vectors tangent to the manifold at point $\mathbf{X}(t)$, $\mathbf{U}(t) = \{d\mathbf{X}^1(t), d\mathbf{X}^2(t), ..., d\mathbf{X}^d(t)\}$. The volume of the parallelepiped will evolve over time in a manner determined by the d Lyapunov exponents

$$\sum_{i=1}^{d} \lambda_i = \lim_{t\to\infty} \frac{1}{t} \log \left(\mathrm{Vol}^d(Y(\mathbf{X},t)\mathbf{U}(0))\right). \tag{A.2}$$

Unfortunately, the Lyapunov spectrum cannot be easily extracted using this method. As $t \to \infty$ the different tangent vectors comprising the parallelepiped all begin to point in the direction of the largest Lyapunov exponent. Many methods have been

---

[1] Here the $d\mathbf{X}(0)$ in the denominator leads to zero contribution in the infinite time limit. The $d\mathbf{X}(0)$ in the numerator is left in for consistency with the vectorized expression.

used to circumvent this issue. We use an algorithm introduced by Bennetin et al. [99].

An orthonormal basis for the tangent space $\mathbf{V}(t) = \{d\hat{\mathbf{X}}^1(t), d\hat{\mathbf{X}}^2(t), ..., d\hat{\mathbf{X}}^d(t)\}$ is defined and then evolved for a short time:

$$\mathbf{U}(t + \delta t) = Y(\mathbf{X}, t)\mathbf{V}(t). \tag{A.3}$$

This evolution rotates and changes the length of each of the unit vectors in $\mathbf{V}(t)$. By performing a QR decomposition on $\mathbf{U}(t + \delta t)$ we can separate these two effects:

$$\mathbf{U}(t + \delta t) = \mathbf{Q}(t + \delta t)\mathbf{R}(t + \delta t). \tag{A.4}$$

$\mathbf{V}(t + \delta t) \equiv \mathbf{Q}(t + \delta t)$ is a new orthonormal basis for the tangent space, obtained by rotating the basis vectors from the previous time step. Since $\det[U(t + \delta t)] = \prod_i R_{ii}$ the diagonal elements of $\mathbf{R}(t + \delta t)$ capture the extent to which the volume of the parallelepiped at the previous time step has changed.

This process is repeated iteratively to obtain a sequence of matrices $\mathbf{R}(t)$ from which me may extract the Lyapunov spectrum using

$$\lambda_i = \lim_{N\to\infty} \frac{1}{N\delta t} \sum_{n=1}^{N} \log |R_{ii}(n\delta t)|. \tag{A.5}$$

When studying finite systems it may be more convenient to calculate Lyapunov exponents using a time-series approach [201, 202, 203, 204]. This would involve extracting exponents from the evolution of observables, it is currently unclear if exponents can be accurately calculated in the quantum context using this approach.

Appendix B

Testing frictional matrix product state update

In this appendix I give the background to the checks made of the matrix product state Langevin code, discussed in Chapter 4, for a dissipative system. This was done by deriving closed-form equations of motion for a system of two spin-1/2s evolving under a Heisenberg coupling with local fields:

$$\hat{H} = J\left(\hat{\sigma}_x^{(1)}\hat{\sigma}_x^{(2)} + \hat{\sigma}_y^{(1)}\hat{\sigma}_y^{(2)} + \hat{\sigma}_z^{(1)}\hat{\sigma}_z^{(2)}\right) + h_1\hat{\sigma}_z^{(1)} + h_2\hat{\sigma}_x^{(2)}, \tag{B.1}$$

where $\hat{\sigma}_{x,y,z}$ are the usual Pauli operators. Additionally the system is coupled isotoptrically to oscillator baths. These equations were evolved in Wolfram Mathematica and the resulting trajectories compared with the MATLAB implementation of the matrix product state Langevin equation discussed in chapter 4. This allows for a check of the MATLAB code under entangling and dissipative dynamics, using an entirely separate implementation.

System parameterization

A system of two spin-1/2s can be parameterized in terms of an orthogonal basis $\{|\mathbf{l}_1, \mathbf{l}_2\rangle, |-\mathbf{l}_1, -\mathbf{l}_2\rangle\}$ of joint coherent states, where $\mathbf{l}$ is an O(3) vector on the Bloch sphere. The resulting parameterization is a permanent Schmidt decomposition of the state partitioned into the individual spins:

$$|\psi\rangle = n_1|\mathbf{l}_1, \mathbf{l}_2\rangle + n_2|-\mathbf{l}_1, -\mathbf{l}_2\rangle, \tag{B.2}$$

where $(n1, n2)$ is a SU(2) spinor whose components give the Schmidt coefficients via $|n_1|^2$ and $|n_2|^2$. The spin coherent states $|\pm\mathbf{l}_i\rangle$ also permit an SU(2) description

$(l_{i,1}, l_{i,2})$ for spin index $i = 1, 2$. The spinor components of the n, l_1 and l_2 can be parameterized in terms of polar and azimuthal angles on the Bloch sphere:

$$\begin{pmatrix} n_1 \\ n_2 \end{pmatrix} = \begin{pmatrix} \cos(\psi/2) \\ \sin(\psi/2)e^{i\beta} \end{pmatrix}, \quad \begin{pmatrix} l_{i,1} \\ l_{i,2} \end{pmatrix} = \begin{pmatrix} \cos(\theta_i/2)e^{-i\phi_i/2} \\ \sin(\theta_i/2)e^{+i\phi_i/2} \end{pmatrix}. \tag{B.3}$$

Deriving equations of motion

We can now derived equations of motion for the two-spin system under the Langevin equation derived in Chapter 4, in the dissipation-only limit of zero temperature. The method is to start with the Euler-Lagrange equation of motion

$$\frac{d}{dt}\frac{\partial \mathcal{L}_0}{\partial \dot{q}} - \frac{\partial \mathcal{L}_0}{\partial q} + \gamma \sum_{i=1}^{2} \sum_{\alpha=x,y,z} \frac{d\langle \hat{\sigma}_\alpha^{(k)} \rangle}{dt} \frac{\partial \langle \hat{\sigma}_\alpha^{(k)} \rangle}{\partial q} = 0, \tag{B.4}$$

where the system parameters $q \in \{\psi, \beta, \theta_1, \phi_1, \theta_2, \phi_2\}$, γ is the frictional coupling rate, and the system-only Lagrangian $\mathcal{L}_0$ is given by

$$\mathcal{L}_0 = \langle \psi | \left(i\partial_t - \hat{H} \right) | \psi \rangle = i\langle \psi | \dot{\psi} \rangle - H, \tag{B.5}$$

using the abbreviation $H = \langle \psi | \hat{H} | \psi \rangle$. The resulting equations of motion for the system variables can be manipulated into a closed form, which is then integrated forwards using the `NDSolve` function in Mathematica.

Computing the Langrangian: The system Lagrangian $\mathcal{L}_0$ can be found to be equal to

$$\mathcal{L}_0 = \frac{n_z}{2} \left(\dot{\beta} + \sum_{k=1}^{2} l_k^z \dot{\phi}_k \right) - H, \tag{B.6}$$

where $n_z = \cos\psi$ and $l_k^z = \cos\theta_k$ are the $z-$components of the corresponding O(3) vectors.

Deriving Euler-Langrange equations: Choosing $q = n_z, \beta, l_k^z$ in Eq B.4 leads to the following respective equations of motion:

$$\dot{\beta} + \sum_{k=1}^{2} l_k^z \dot{\phi}_k - 2\partial_{n_z} H - 4\gamma \dot{n}_z = 0 \tag{B.7}$$

$$\dot{n}_z + 2\partial_\beta H = 0 \tag{B.8}$$

$$n_z l_k^\perp \dot{\phi} + 2\partial_{\theta_k} + 2\gamma n_z^2 \dot{\theta} = 0, \tag{B.9}$$

where $l_k^\perp = \sin\theta_k$ is the component of $\mathbf{l}$ perpendicular to the z-axis. A further equation can be derived by taking $q = \phi_k$ and using Eq B.8 to find

$$n_z \dot{l}_k^z - 2 l_k^z \partial_\beta H + 2\partial_{\phi_k} H + 2\gamma n_z^2 (l_k^\perp)^2 \dot{\phi}_k = 0. \tag{B.10}$$

Changing back to the angular variables $(\psi, \beta, \theta_1, \phi_1, \theta_2, \phi_2)$ and splitting into the Hamiltonian and dissipative contributions (so that $\dot{q} = \dot{q}_H + \dot{q}_{\text{diss}}$) we get for the Hamiltonian parts

$$\dot{\beta}_H = \sum_{k=1}^{2} \frac{2\cot\theta_k \partial_{\theta_k} H}{\cos\psi} - \frac{2\partial_\psi H}{\sin\psi}, \tag{B.11}$$

$$\dot{\psi}_H = \frac{2\partial_\beta H}{\sin\psi}, \tag{B.12}$$

$$\dot{\theta}_{k,H} = \frac{-2\cot\theta_k \partial_\beta H}{\cos\psi} + \frac{2\partial_{\phi_k} H}{\cos\psi \sin\theta_k}, \tag{B.13}$$

$$\dot{\phi}_{k,H} = \frac{-2\partial_{\theta_k} H}{\cos\psi \sin\theta_k}, \tag{B.14}$$

and for the dissipative parts

$$\dot{\beta}_{\text{diss}} = 2\gamma \cos\psi \sum_{k=1}^{2} \cot\theta_k \dot{\theta}^k - 4\gamma \sin_\psi \dot{\psi}, \tag{B.15}$$

$$\dot{\psi}_{\text{diss}} = 0, \tag{B.16}$$

$$\dot{\theta}_{k,\text{diss}} = 2\gamma \cos\psi \sin\theta_k \dot{\phi}_k, \tag{B.17}$$

$$\dot{\phi}_{k,\text{diss}} = \frac{-2\gamma\cos\psi}{\sin\theta_k} \dot{\theta}_k. \tag{B.18}$$

The structure of these equations is that each of the Hamiltonian terms depends on derivatives of the energy H, and each of the dissipative terms depends on a time-derivative of one of the system variables.

Final equations of motion: These coupled equations of motion can be written as a matrix equation. Letting $\mathbf{v} = (\psi, \beta, \theta_1, \phi_1, \theta_2, \phi_2)^\intercal$ and $\nabla = (\partial_\psi, \partial_\beta, \partial_{\theta_1}, \partial_{\phi_1}, \partial_{\theta_2}, \partial_{\phi_2})^\intercal$

the equations can be written as $\dot{\mathbf{v}} = M\nabla H + N\dot{\mathbf{v}}$ with

$$M = -2\begin{pmatrix} 0 & -\frac{1}{\sin_{\psi}} & 0 & 0 & 0 & 0 \\ \frac{1}{\sin\psi} & 0 & -\frac{\cos\theta_1}{\cos\psi\sin\theta_1} & 0 & -\frac{\cos\theta_2}{\cos\psi\sin\theta_2} & 0 \\ 0 & \frac{\cos\theta_1}{\cos\psi\sin\theta_1} & 0 & -\frac{1}{\cos\psi\sin\theta_1} & 0 & 0 \\ 0 & 0 & \frac{1}{\cos\psi\sin\theta_1} & 0 & 0 & 0 \\ 0 & \frac{\cos\theta_2}{\cos\psi\sin\theta_2} & 0 & 0 & 0 & -\frac{1}{\cos\psi\sin\theta_2} \\ 0 & 0 & 0 & 0 & \frac{1}{\cos\psi\sin\theta_2} & 0 \end{pmatrix}, \tag{B.19}$$

$$N = -\gamma\begin{pmatrix} 0 & 0 & 0 & 0 & 0 & 0 \\ 4\sin\psi & 0 & \frac{-2\cos\psi\cos\theta_1}{\sin\theta_1} & 0 & \frac{-2\cos\psi\cos\theta_2}{\sin\theta_2} & 0 \\ 0 & 0 & 0 & -2\cos\psi\sin\theta_1 & 0 & 0 \\ 0 & 0 & \frac{2\cos\psi}{\sin\theta_1} & 0 & 0 & 0 \\ 0 & 0 & 0 & 0 & 0 & -\cos\psi\sin\theta_2 \\ 0 & 0 & 0 & 0 & \frac{2\cos\psi}{\sin\theta_2} & 0 \end{pmatrix}. \tag{B.20}$$

The solution is $\dot{\mathbf{v}} = (1-N)^{-1}M\nabla H$, which can be evaluated by inverting $(1-N)$. It turns out an analytical expression can be found for this inversion:

$$(1-N)^{-1} = \begin{pmatrix} 1 & 0 & 0 & 0 & 0 & 0 \\ -2\gamma\sin\psi & 1 & \frac{\gamma\cos\psi\cot\theta_1}{\gamma^2\cos^2\psi+1} & \frac{\gamma^2\cos\theta_1\cos^2\psi}{\gamma^2\cos^2\psi+1} & \frac{\gamma\cos\psi\cot\theta_2}{\gamma^2\cos^2\psi+1} & \frac{\gamma^2\cos\theta_2\cos^2\psi}{\gamma^2\cos^2\psi+1} \\ 0 & 0 & \frac{1}{\gamma^2\cos^2\psi+1} & \frac{\gamma\cos\psi\sin\theta_1}{\gamma^2\cos^2\psi+1} & 0 & 0 \\ 0 & 0 & -\frac{\gamma\cos\psi\ \mathrm{cosec}\theta_1}{\gamma^2\cos^2\psi+1} & \frac{1}{\gamma^2\cos^2\psi+1} & 0 & 0 \\ 0 & 0 & 0 & 0 & \frac{1}{\gamma^2\cos^2\psi+1} & \frac{\gamma\cos\psi\sin\theta_2}{\gamma^2\cos^2\psi+1} \\ 0 & 0 & 0 & 0 & -\frac{\gamma\cos\psi\ \mathrm{cosec}\theta_2}{\gamma^2\cos^2\psi+1} & \frac{1}{\gamma^2\cos^2\psi+1} \end{pmatrix}. \tag{B.21}$$

giving a closed form expression for $\dot{\mathbf{v}}$ and hence the system state.

Using this to test MATLAB code

This closed system of equations was coded in Wolfram Mathematica and integrated forwards to find trajectories for the variables $q(t)$, from which expectation values for the local Pauli operators can be derived. This provided an invaluble tool in testing the MATLAB implementation of the matrix product state Langevin equation: by turning on and off the parameters J, h_1, h_2 in the Hamiltonian of Eq B.1, different parts of the dynamics could be probed. This was particularly useful in rooting out more subtle bugs in the MATLAB code. Fig 4.3 in Chapter 4 shows agreement between the MATLAB and Mathematica implementations when all of J, h_1, h_2 are non-zero. As a further tests of cases of the MATLAB when the system is larger than two spins, this 2-spin dynamics was embedded at various points in a larger spin chain.

Appendix C

Calculation of optimal schedule for hypercube search

In this appendix two different schedules for adiabatic search on the hypercube are presented, both based on a saturation of the adiabatic condition (Eq 6.15). First an analytical derivation, based on approximate expressions for the energy eigenvalues of the system. Second, using an exact numerical calculation of the gap. For large systems the difference between these schedules is small.

1 Analytical derivation of hypercube schedule

Starting from the Hamiltonian for the AQC search on a hypercube, Eq 6.13,

$$\hat{H}(s) = (1-s)\sum_{j=1}^{n}\frac{1}{2}(1-\hat{\sigma}_x^{(j)}) + s(\mathbb{1} - |m\rangle\langle m|),$$

we first assume, without loss of generality, that the marked state label m is all zeros. We then express the Hamiltonian in the symmetric subspace in terms of total spin operators

$$\hat{S}_a = \frac{1}{2}\sum_{j=1}^{n}\hat{\sigma}_a^{(j)} \tag{C.1}$$

for $a \in \{x, y, z\}$, which have eigenstates $|\frac{n}{2} - r\rangle_a$ for $r \in \{0, \ldots, n\}$. In this representation, the marked state is $|\frac{n}{2}\rangle_z$, and the AQC search Hamiltonian becomes

$$\hat{H}(s) = (1-s)(\tfrac{n}{2} - \hat{S}_x) + s(\mathbb{1} - |\tfrac{n}{2}\rangle_z\langle\tfrac{n}{2}|). \tag{C.2}$$

Following Farhi et al [172] to analyze the eigensystem, we obtain the eigenvalue equation

$$\frac{1-s}{s} = \frac{1}{N}\sum_{r=0}^{n}\binom{n}{r}\frac{1}{r-\lambda} \tag{C.3}$$

for the energy eigenvalues $E_k = s + (1-s)\lambda_k$. Farhi et al [172] solve this at the minimum gap, occuring at $s = s_m$:

$$\frac{1-s_m}{s_m} = \frac{1}{N}\sum_{r=1}^{n}\binom{n}{r}\frac{1}{r} \equiv R_1, \tag{C.4}$$

and show that $\lambda_{1,0}^{(\text{gmin})} \simeq \pm n/(2\sqrt{N})$ for the two lowest eigenvalues corresponding the the ground state E_0 and first excited state E_1.

To obtain the optimal schedule following the method in Roland and Cerf [176], we need an expression for the gap as a function of time, not just at its minimum. We expand the eigenvalue equation (Eq C.3) for $\lambda \ll 1$

$$\frac{1-s}{s} = \frac{-1}{N\lambda} + \frac{1}{N}\sum_{r=1}^{n}\binom{n}{r}\frac{1}{r}(1+\lambda/r) + O(\lambda^2). \tag{C.5}$$

Using R_1 and R_2 from Eqs 6.8, C.4, and 6.22 we obtain

$$\frac{1-s}{s} = \frac{-1}{N\lambda} + R_1 + \lambda R_2. \tag{C.6}$$

This quadratic equation in λ has roots

$$\lambda = \frac{1}{2R_2}\left\{\frac{1-s}{s} - R_1\right\} \pm \frac{1}{2}\left\{\frac{1}{R_2^2}\left(\frac{1-s}{s} - R_1\right)^2 + \frac{4}{NR_2}\right\}^{\frac{1}{2}} \tag{C.7}$$

and gives for the gap $g(s) = (1-s)(\lambda_1 - \lambda_0)$

$$g(s) = (1-s)\left\{\frac{1}{R_2^2}\left(\frac{1-s}{s} - R_1\right)^2 + \frac{4}{NR_2}\right\}^{\frac{1}{2}}. \tag{C.8}$$

To optimize the schedule, we need to solve Eq 6.15

$$\left|\frac{ds}{dt}\right| \leq \epsilon \frac{g^2(s)}{\left|\left\langle \frac{d\hat{H}}{ds}\right\rangle_{0,1}\right|}$$

using the expression for $g(s)$ in Eq C.8. To obtain a suitable approximate value for $\langle \frac{d\hat{H}}{ds}\rangle_{0,1}$, we first calculate $\frac{d\hat{H}}{ds}$ in the symmetric subspace representation of Eq C.2,

$$\frac{d\hat{H}}{ds} = -(\tfrac{n}{2} - \hat{S}_x) + (\mathbb{1} - |\tfrac{n}{2}\rangle_z\langle\tfrac{n}{2}|). \tag{C.9}$$

It is sufficient to use the maximum value of $\langle \frac{d\hat{H}}{ds}\rangle_{0,1}$, which occurs at s_m, where the eigenstates $|E_{1,0}\rangle \simeq (|\frac{n}{2}\rangle_x \pm |\frac{n}{2}\rangle_z)/\sqrt{2}$, giving $\langle\frac{d\hat{H}}{ds}\rangle_{0,1}^{(\max)} \leq \frac{n}{4}$. We then have the following equation to solve for $s(t)$

$$\frac{ds}{dt} = \frac{4\epsilon}{nR_2^2}(1-s)^2\left\{\left(\frac{1-s}{s} - R_1\right)^2 + \frac{4R_2}{N}\right\} \tag{C.10}$$

This can be integrated to obtain

$$\begin{aligned}\frac{4\epsilon t}{nR_2^2} + c = &\frac{R_1^2 - 4R_2/N}{2\sqrt{R_2/N}(R_1^2+4R_2/N)^2}\arctan\left\{\frac{((1+R_1)^2+4R_2/N)s-(1+R_1)}{2\sqrt{R_2/N}}\right\}\\ &+\frac{1}{(1-s)(R_1^2+4R_2/N)}\\ &+\frac{R_1}{(R_1^2+4R_2/N)^2}\ln\left\{\frac{(1-s-R_1s)^2+\frac{4R_2}{N}s^2}{(1-s)^2}\right\}\end{aligned} \tag{C.11}$$

where c is the constant of integration. To obtain the constant, set $s = t = 0$, giving

$$c' = \arctan\left\{\frac{(1+R_1)\sqrt{N}}{2\sqrt{R_2}}\right\} + \frac{R_1^2+4R_2/N}{R_1^2-4R_2/N}\frac{2\sqrt{R_2}}{\sqrt{N}} \tag{C.12}$$

where the factors in front of the arctan term have been rearranged to give a more convenient form for the constant. One can then in principle solve for $s(t)$. However, the terms on the RHS, apart from the arctan, are potentially problematic as $s \to 1$. Given that we started with the approximation $\lambda \ll 1$, which occurs at the position of the minimum gap, we can't necessarily expect that the solution will be valid for $s \to 1$. We first note that taking only the arctan term on the RHS gives a schedule that is valid for all $0 \leq s \leq 1$, and it provides a runtime proportional to $\sqrt{N}$. If we don't discard these extra terms, we can show that they can be neglected, provided we stop the anneal very slightly before $s = 1$, but still well past the minimum gap.

To solve for $s(t)$ retaining the full expression, invert the arctan to give

$$\begin{aligned}s(t) = &\frac{2\sqrt{R_2}}{\sqrt{N}\{(1+R_1)^2+4R_2/N\}}\tan\left\{\frac{8\epsilon t\sqrt{R_2}}{nR_2^2\sqrt{N}}\frac{R_1^2+4R_2/N}{R_1^2-4R_2/N} - c''\right\}\\ &+\frac{1+R_1}{(1+R_1)^2+4R_2/N},\end{aligned} \tag{C.13}$$

where c'' now contains the awkward extra terms,

$$\begin{aligned} c'' =& c' - \frac{1}{(1-s)} \frac{R_1^2 + 4R_2/N}{R_1^2 - 4R_2/N} \frac{2\sqrt{R_2}}{\sqrt{N}} \\ &- \frac{R_1}{R_1^2 - 4R_2/N} \frac{2\sqrt{R_2}}{\sqrt{N}} \ln\left\{ \frac{(1-s-R_1 s)^2 + \frac{4R_2}{N} s^2}{(1-s)^2} \right\} \\ =& \arctan\left\{ \frac{(1+R_1)\sqrt{N}}{2\sqrt{R_2}} \right\} + \frac{s}{(1-s)} \frac{R_1^2 + 4R_2/N}{R_1^2 - 4R_2/N} \frac{2\sqrt{R_2}}{\sqrt{N}} \\ &- \frac{R_1}{R_1^2 - 4R_2/N} \frac{2\sqrt{R_2}}{\sqrt{N}} \ln\left\{ \frac{(1-s-R_1 s)^2 + \frac{4R_2}{N} s^2}{(1-s)^2} \right\}. \end{aligned} \tag{C.14}$$

The arctan argument is large, so the arctan is close to $\pi/2$. We note that the extra terms are small for most values of s, and only become large as $s \to 1$. To check when these terms become $O(1)$, for the first extra term we solve

$$\frac{s}{(1-s)} \frac{R_1^2 + 4R_2/N}{R_1^2 - 4R_2/N} \frac{2\sqrt{R_2}}{\sqrt{N}} \simeq 1 \tag{C.15}$$

to obtain

$$s \simeq \frac{1}{1 + 2\sqrt{R_2/N}} \simeq \frac{1}{1 + 4/(n\sqrt{N})}. \tag{C.16}$$

This is well past the minimum gap, which occurs at $s = 1/(1+R_1) \simeq 1/(1+2/n)$. Applying the same procedure to the second extra term gives to leading order

$$s \simeq 1 - e^{-\sqrt{N}/4}, \tag{C.17}$$

which is even closer to $s = 1$ and further from the minimum gap. Since the transition probabilities are only significant close to the minimum gap, and hence all the important slowing down of the schedule occurs around the gap, what happens this close to $s = 1$ has essentially no effect on the success or runtime of the algorithm.

Dropping the extra terms from the solution provides an expression for $s(t)$

$$s(t) = \frac{2\sqrt{R_2}}{\sqrt{N}(1+R_1)^2} \tan\left\{ \frac{8\epsilon\sqrt{R_2} R_1^2 t}{n\sqrt{N} R_2^2} - c''' \right\} + \frac{1}{1+R_1} \tag{C.18}$$

where we have also dropped terms $O(1/N)$, and

$$c''' = \arctan\left\{ \frac{(1+R_1)\sqrt{N}}{2\sqrt{R_2}} \right\}. \tag{C.19}$$

Strictly speaking, this is valid for $s \lesssim \frac{1}{1+4/(n\sqrt{N})}$, although in fact it is well-behaved right up to and including $s = 1$. From this we can obtain the runtime

$$\epsilon\, t_f \simeq \frac{\pi\sqrt{N}}{4}, \tag{C.20}$$

where the two arctan terms have each been approximated by $\pi/2$, since their arguments are large, $O(\sqrt{N})$.

2 Numerical derivation of hypercube schedule

The above approach is based on an approximate analytical expression for the gap, in the large-size limit and expanded around the minimum gap. An alternative is to calculate the gap exactly at all points $s(t)$ using numerical methods. We do this using the iterative eigensolving modules in Numpy [205], which enables us to iteratively solve $\left|\frac{ds}{dt}\right| = \epsilon 4 g^2(s)/n$.

We first define a normalized function

$$F(s) = \int_0^s ds' \frac{1}{\epsilon g^2(s')} \times \left[\int_0^1 ds' \frac{1}{\epsilon g^2(s')}\right]^{-1}, \tag{C.21}$$

where s is a function of the reduced time τ. To obtain $s(\tau)$, we need to invert this function, $s(\tau) = F^{-1}(\tau)$. This can be accomplished by the following method.

First define $\tau\textsc{List}$ to be a linearly spaced list of points between $\tau = 0$ and $\tau = 1$, and $s\textsc{List}$ to be a list of the corresponding values of $s(\tau)$, obtained by applying $F^{-1}(\tau)$ to each element of $\tau\textsc{List}$. Defining $j(s)$ equal to the number of elements in $s\textsc{List}$ which are strictly less than s, we approximate $F(s)$ numerically by $\tilde{F}(s)$, where we replace the integral by a finite sum plus linear interpolation. Writing $\tilde{s_j} = \frac{1}{2}(s\textsc{List}(j(s)) + s\textsc{List}(j(s)+1))$

$$\begin{aligned}\tilde{F}(s) = &\sum_{j'=1}^{j(s)} \frac{s\textsc{List}(j'+1) - s\textsc{List}(j')}{\mathcal{N}\, g^2\left(\tilde{s_{j'}}\right)} \\ &+ \frac{s - s\textsc{List}(j(s))}{\mathcal{N}\, g^2\left(\tilde{s_j}\right)},\end{aligned} \tag{C.22}$$

where $\mathcal{N}$ is a normalization factor which is included to ensure that $\hat{F}(s = 1) = 1$. It is straightforward to numerically invert $\hat{F}(s)$. This can be accomplished by first finding $j_{\max}(s)$, the largest value of $j(s)$ for which $\hat{F}(s) < \tau$, and then solving

$$\hat{F}(s)|_{j(s)=j_{\max}(s)} = \tau \tag{C.23}$$

for s. Based on this numerical function inversion, we define an iterative method of converging on the solution for $s^{(n)}(\tau)$,

1. Set a linearly spaced $s\textsc{List} \in [0, 1]$ and $\tau\textsc{List} \in [0, 1]$ each with the same number of elements.

2. Using the values of s in sList, apply $\hat{F}^{-1}(\tau)$ to each corresponding element in τList to generate a new sList.
3. Repeat step 2. with the new sList as input, until it has converged.

The advantage of this iterative method is that, at each iteration, more points in sList will concentrate in areas where $1/g^2$ is larger, for instance near the dominant avoided crossing. By using the previously calculated sList as a mesh in the current iteration, the protocol can continuously improve the quality of the numerical inverse with a fixed number of points in sList.

Appendix D

Numerical methods for Chapter 6

Our numerical calculations were carried out using the Python programming language (both Python 2.7 and Python 3.5), making considerable use of the NumPy, SciPy and Matplotlib packages [206, 205, 207, 208]. High performance computing resources were not used in this study, although some of the simulations took several days to run on standard desktop workstations. Most of the simulations consisted of solving the time evolution of the quantum search algorithm by numerically integrating the Schrödinger equation using the appropriate Hamiltonian. This was done by diagonalising the Hamiltonian and exponentiating it in the diagonal basis, before applying it to the wave function. This process was iterated for time dependent Hamiltonians, rotating from one instantaneous diagonal basis to the next at small time intervals. For the high-temperature dephasing studies in Chapter 6, the same process was applied to the density matrix, with dephasing operators also applied along with the unitary time evolution.

For larger simulations, we can take advantage of the symmetry in the hypercube to map the dynamics to a search on the line with appropriately weighted edges, as given by Eq. (C.2) in appendix C. Provided the initial state is also invariant with respect this symmetry, the evolution will be restricted to this symmetric subspace. This allows us to perform simulations for much larger numbers of qubits $n \lesssim 100$, and hence extract reliable information about the scaling with n from numerics alone. This provides important checks of the validity of the two-level approximations made to facilitate the analytical calculations.

Appendix E

Single avoided crossing model for quantum search

There are several ways to parameterize a two-state single avoided crossing model. If we designate the marked state to be the $|0\rangle$ state of a qubit, this will be the end point of the schedule. The initial state needs to be orthogonal to $|0\rangle$, i.e., it has to be $|1\rangle$. These two states are the lowest energy eigenstates of $\frac{1}{2}(\mathbb{1} + \hat{\sigma}_z)$ and $\frac{1}{2}(\mathbb{1} - \hat{\sigma}_z)$ respectively, where the factor of $\frac{1}{2}$ makes the eigenenergies zero and one in our units. We also need a hopping Hamiltonian term $\hat{\sigma}_x$, to drive transitions between $|1\rangle$ and $|0\rangle$. The relative strength of the hopping Hamiltonian is g_{min}, the minimum gap at the avoided crossing. The single avoided crossing AQC search Hamiltonian is

$$\begin{aligned}\hat{H}^{(\text{AC})}(s) &= (1-s)\hat{H}_0^{(\text{AC})} + s\hat{H}_p^{(\text{AC})} \\ &= (1-s)\left\{\frac{1}{2}(\mathbb{1} + \hat{\sigma}_z) - g_{\text{min}}\hat{\sigma}_x\right\} + s\frac{1}{2}(\mathbb{1} - \hat{\sigma}_z). \qquad \text{(E.1)}\end{aligned}$$

The initial state $|1\rangle$ is only an approximate eigenstate of $\hat{H}_0^{(\text{AC})}$ but the approximation improves as g_{min} decreases. Solving the eigensystem for this Hamiltonian gives

$$g^{(\text{AC})}(s) = \{(1-2s)^2 + 4g_{\text{min}}^2(1-s)^2\}^{\frac{1}{2}} \qquad \text{(E.2)}$$

for the gap between the two energy levels. In the limit of small g_{min} the minimum gap is g_{min} and occurs for $s = \frac{1}{2}$. We can then apply the method of [176] to find the optimal schedule $s(t)$ for this system. Calculating $d\hat{H}/ds$ we find

$$\frac{d\hat{H}}{ds}^{(\text{AC})} = -\hat{\sigma}_z + g_{\text{min}}\hat{\sigma}_x \qquad \text{(E.3)}$$

giving a maximum value of one[1] for $|\langle\frac{d\hat{H}^{(\mathrm{AC})}}{ds}\rangle_{0,1}|$ in the large-size limit. Using Eq. (6.19) to find the optimal schedule, we need to solve

$$\frac{ds}{dt} = \frac{\epsilon[g^{(\mathrm{AC})}(s)]^2}{|\langle\frac{d\hat{H}_{\mathrm{AC}}}{ds}\rangle_{0,1}|} = \epsilon\{(1-2s)^2 + 4g_{\mathrm{min}}^2(1-s)^2\}, \tag{E.4}$$

where the maximum value is used for $|\langle\frac{d\hat{H}^{(\mathrm{AC})}}{ds}\rangle_{0,1}|$. This can be integrated straightforwardly to give

$$\arctan\left\{2g_{\mathrm{min}}(s-1) + \frac{2s-1}{g_{\mathrm{min}}}\right\} = 2g_{\mathrm{min}}\epsilon t + c \tag{E.5}$$

with

$$c = -\arctan\left\{2g_{\mathrm{min}} + \frac{1}{g_{\mathrm{min}}}\right\}. \tag{E.6}$$

From this we find for $s = 1$ that the runtime $t_f^{(AC)}$ is given by

$$\epsilon\, t_f^{(AC)} = \frac{\frac{\pi}{2} - \arctan(g_{\mathrm{min}})}{g_{\mathrm{min}}} \simeq \frac{\pi}{2\, g_{\mathrm{min}}} - 1, \tag{E.7}$$

where the approximate expression uses $\arctan(1/g_{\mathrm{min}}) \simeq \frac{\pi}{2} - g_{\mathrm{min}}$ for $g_{\mathrm{min}} \ll 1$ and terms of order g_{min}^2 have been dropped. The runtime of the optimal schedule thus depends inversely on the size of the minimum gap, as expected. Solving for $s(t)$ and dropping terms of order g_{min}^2 gives

$$s(t) \simeq \frac{1}{2}\left\{1 - g_{\mathrm{min}}\cot\left[g_{\mathrm{min}}(2\epsilon t + 1)\right]\right\}. \tag{E.8}$$

In this limit where $g_{\mathrm{min}} \ll 1$, an equivalent way to parameterize $\hat{H}^{(\mathrm{AC})}$ is

$$\hat{H}^{(\mathrm{AC})} = \frac{g_{\mathrm{min}}}{2}\left[f(t)\hat{\sigma}_z - \hat{\sigma}_x\right], \tag{E.9}$$

where $-\infty < f(t) < \infty$. This form is obtained by taking $(1-2s(t))/g_{\mathrm{min}} \to f(t)$ and shifting the zero point of the energy scale to the middle of the avoided crossing. As $f(t)$ changes from $-\infty$ to ∞ it passes through zero as the sign of the $\hat{\sigma}_z$ term changes, when the $\hat{\sigma}_x$ term drives the transition from $|1\rangle$ to $|0\rangle$. Although the $\hat{\sigma}_x$ term is no longer turned off at the end of the schedule, it becomes negligible in comparison to the $\hat{\sigma}_z$ term and does not significantly alter the dynamics. This can be intuitively thought of as scaling all features of $\hat{H}^{(\mathrm{AC})}$ other than the avoided crossing to $\pm\infty$.

The QW form of the single avoided crossing search Hamiltonian is also simple to analyze. We deduce the optimal value of $\gamma_o = 1$ from the value of $s = \frac{1}{2}$ at the

---

[1] Strictly the maximum value is $\sqrt{1 + g_{\mathrm{min}}^2} = 1 + \mathcal{O}(g_{\mathrm{min}}^2)$, however this correction simply modifies ϵ in what follows, and disappears altogether when terms of order g_{min}^2 are dropped.

avoided crossing. We then use Eqns. (6.27) in which $\beta_o = 1/(1+\gamma_o) = \frac{1}{2}$, whence

$$\begin{aligned}\hat{H}^{\mathrm{AC}}_{(\mathrm{QWS})} &= (1-\beta_o)\hat{H}_0^{(\mathrm{AC})} + \beta_o \hat{H}_p^{(\mathrm{AC})} \\ &= \frac{1}{2}\left\{\frac{1}{2}(\mathbb{1}+\hat{\sigma}_z) - g_{\min}\hat{\sigma}_x + \frac{1}{2}(\mathbb{1}-\hat{\sigma}_z)\right\} \\ &= \frac{1}{2}(\mathbb{1} - g_{\min}\hat{\sigma}_x) \qquad \text{(E.10)}\end{aligned}$$

The $\hat{\sigma}_x$ term causes deterministic transitions between the two states regardless of their energies, at a rate determined by $g_{\min}$. By solving for the dynamics, the time for the input state $|1\rangle$ to evolve to the marked state $|0\rangle$ can be shown to be $t_f^{(qw)} = \pi/g_{\min}$.

We can now map between QW and AQC in the avoided crossing model using Eqs. (6.29) for $A(\alpha,\beta,\tau)$ and $B(\alpha,\beta,\tau)$. Using $\beta = \frac{1}{2} = 1/(1+\gamma_o)$, for $s(t)$ from Eq. (E.8) we have hybrid schedules

$$\begin{aligned}A_{\mathrm{AC}}(\alpha,t) &= \frac{1-s(t)}{\alpha + 2(1-\alpha)(1-s(t))} \\ B_{\mathrm{AC}}(\alpha,t) &= \frac{s(t)}{\alpha + 2(1-\alpha)s(t)}. \qquad \text{(E.11)}\end{aligned}$$